OUKA
The University of Osaka
Institutional Knowledge Archive

Title	Fundamental study on finite-size graphene-based materials with unique electronic structures toward catalyst-assisted microfabrication of semiconductor surfaces
Author(s)	李, 君寰
Citation	大阪大学, 2024, 博士論文
Version Type	VoR
URL	https://doi.org/10.18910/98770
rights	
Note	

The University of Osaka Institutional Knowledge Archive : OUKA

https://ir.library.osaka-u.ac.jp/

The University of Osaka

Doctoral Dissertation

Fundamental study on finite-size graphene-based materials with unique electronic structures toward catalyst-assisted microfabrication of semiconductor surfaces

Junhuan Li

July 2024

Graduate School of Engineering,
Osaka University

CONTENTS

CHAPTER

1

INTRODUCTION

Manufacturing techniques have always been a milestone in the history of human civilization. Nowadays, the development of manufacturing not only involves large objects such as airplanes and oil tankers but also extends to fields such as semiconductor chips and microelectromechanical systems, pursuing continuously shrinking feature sizes. Against this backdrop, nanotechnology has emerged. Nano-scale manufacturing technology utilizes the interaction of energy and matter, achieving specific dimensions, shapes, and patterns within the micrometer and nanometer scale ranges. It extends further from precision manufacturing, involving control over dimensions, precision, and material properties. These techniques typically include processes such as lithography, electron-beam lithography, ion beam etching, chemical etching, and atomic layer deposition, with widespread coverages in fields such as microelectronics, integrated optics, nanotechnology, and biomedical science.

1.1 MICROFABRICATION ON SEMICONDUCTOR SURFACES

The greatest invention of the 20th century was arguably the transistor, which marked the beginning of the microelectronics era. In 1947, scientists at the Bell Laboratory, a division of the American telecommunications company AT&T, invented the world's first transistor [1)]. Since then, the semiconductor industry based on silicon materials has rapidly captured most of the market, becoming the cornerstone of high-tech industries at the time and continuing to this day. The rapid development of microelectronics, as shown in Figure 1.1 [2)], has largely benefited from the emergence of integrated circuits (IC), or, in other words, transistor miniaturization and integration on a single chip.

A. From Microelectronics to Optoelectronics

In the information age, the development of microelectronics technology is astonishingly rapid. Moore's Law [3)] predicts that the number of transistors on an integrated circuit doubles approximately every 18 months, while the cost is halved. For instance, with the most advanced technology, TSMC successfully mass-produced 3 nm Fin field effect transistors in 2022 [4)]. Future challenges may include the quantum tunneling effect [5)] becoming significant as the critical dimensions of chips enter deep nanometer scales (i.e., electrons may tunnel through adjacent wires). Additionally, further increases in IC integration density become extremely difficult, and

the power consumption and heat dissipation [6] of transistors are particularly problematic.

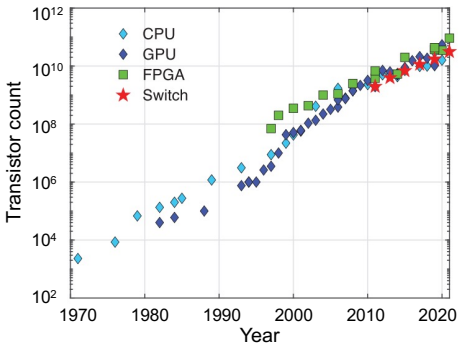

Figure 1.1 Transistor count of CPU, GPU, FPGA, and switch die and their release dates [2].

Currently, most information is transmitted through electrical signals over wires. However, due to the rest mass of electrons, their movement and signal transmission are susceptible to electromagnetic interference from electrostatic forces between electrons, thereby limiting the capacity and speed of electronic communications. On the other hand, driven by advances in computer and communication technologies, there is a growing demand for higher processing speeds, larger data-storage capacities, and higher transmission rates in microelectronic devices. Photons, as information carriers, offer distinct advantages over electrical signals: they possess no rest mass, experience minimal interference, and can utilize various wavelengths of light for simultaneous multi-channel communication. Therefore, optical information transmission offers greater bandwidth and higher speed. Additionally, the processing speed of optical signals is high and immune to electromagnetic interference. These advantages suggest that photonic technology will play a crucial role in the information society of the future.

B. Development and Applications of Optoelectronics

Inspired by the development process of microelectronics, the development strategy of photonics follows these three steps:

- Miniaturization of optical devices
- Integrated photonics
- Optoelectronic technology

To achieve the miniaturization of optical devices, it is necessary to utilize micro-nano manufacturing techniques [7-9] to fabricate individual optical components that are small in size and

light in weight. Although photonics does not require the stringent size control that integrated circuits do, it still needs precise control of the components' dimensions at the wavelength or micron scale. Furthermore, unlike electronic devices such as transistors, which mainly use silicon materials, optical devices for emission, coupling, transmission, modulation, logic, processing, and reception of light rely on the physical properties of different semiconductor materials [10-12]. Integrated photonics involves connecting these optical devices on the same substrate (typically silicon) through optical waveguides [9,13,14] to form a miniature photonic system (Figure 1.2 [15] and Figure 1.3) with specific functions. The ultimate goal is to connect integrated circuits and integrated photonic circuits on the same silicon platform [16-18], achieving optoelectronic interconnection technology and fundamentally transforming future communication and computing technologies.

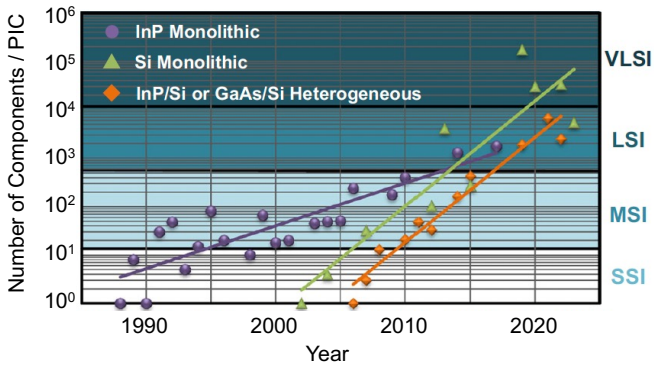

Figure 1.2 Timeline for the number of components on a silicon photonic integrated circuit (PIC) over generations of small-scale, medium-scale, large-scale, and very-large-scale integration (SSI, MSI, LSI, VLSI, respectively) [15].

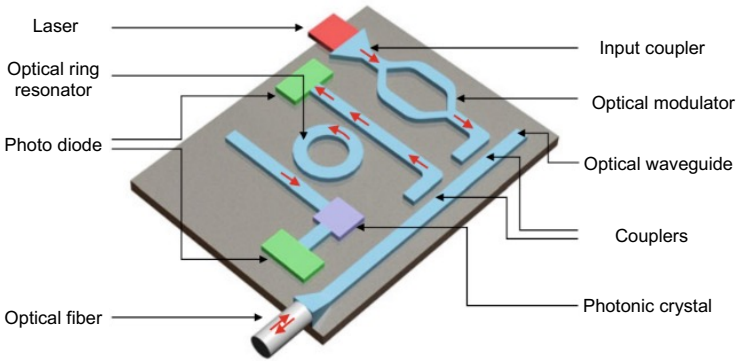

Figure 1.3 A photonic integrated circuit.

Although optical-electrical interconnect technology is still far from being realized, silicon-based photonic systems have already been widely applied, particularly in the data communication field. Both short- and long-reach applications are included, for instance, high-bandwidth communication, coherent communication [28], and complex modulation schemes. Undoubtedly, aside from numerous commercial applications, the academic community is also actively exploring application scenarios for this technology. These include, but are not limited to, nano-optomechanics and condensed matter physics [19], sensors [20,21,31], nonlinear optics [22], optical gyroscopes [23,24], RF integrated optoelectronics [25,26], integrated radio transceivers [27], novel light sources [29] beyond early lasers and LEDs, noise reduction methods for laser [30].

C. Technical Challenges

As mentioned above, Si-based photonics holds tremendous application prospects. Next, let's discuss the challenges faced in the miniaturization of optical devices, as shown in Figure 1.4 [32]. Note that we focus on the processing challenges required for miniaturization rather than delving into optical integration, such as connections and couplings between different semiconductor materials or devices, or further integration with microelectronic devices.

Firstly, let's examine the advantages of miniaturization in optical device fabrication. One very significant advantage is the ability to leverage mature process systems in microelectronics, such as complementary metal-oxide-semiconductors (CMOS). These technologies have accumulated decades of technical experience, garnered substantial financial support, and witnessed countless innovations from numerous technical personnel.

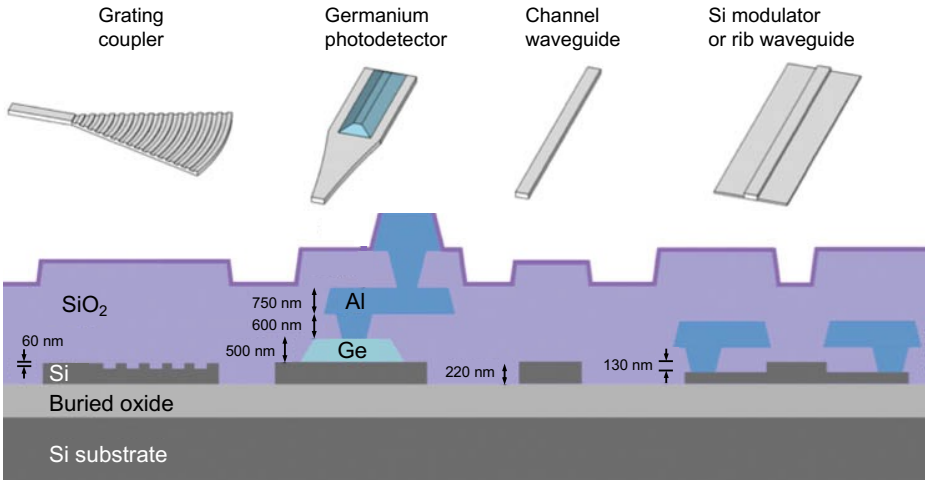

Figure 1.4 A diagram of the cross-sectional of key photonic devices in a Si platform [32].

However, there are a series of technical challenges ahead:

- Because of the diversity of optical devices and their varying operating principles, it is necessary to process III-V group semiconductor materials in addition to silicon. These materials and processing methods need to be compatible with CMOS technology. For example, as ideal materials for semiconductor lasers and photodetectors, Ge materials can be integrated into silicon platforms through bonding or epitaxial growth.
- Different optical components typically use optical waveguides for signal propagation. To reduce propagation loss in submicron waveguides [33,34], it is essential to have semiconductor microfabrication methods that can form smooth sidewalls, optimize the geometry, and ensure precise coupling.
- In terms of processing individual optical devices, it is not necessary to create tiny structures (the typical critical dimension is about 100 nm). A typical three-dimensional structure involves constructing an array of micron-sized pillars or holes on the semiconductor surface.

From the perspectives of cost and performance, photonic products need to draw from traditional technologies in microelectronics while considering the unique characteristics (as we mentioned above) of photonic devices. In summary, the development of optoelectronic technology urgently requires new semiconductor surface processing techniques.

1.2 MOTIVATION OF THIS STUDY

The focus of this thesis is a novel fabrication method aimed at creating micron-sized, three-dimensional (3D) structures on semiconductor surfaces according to design requirements. The fabrication method should be compatible with CMOS, and the processed semiconductor surface and sidewalls must be smooth and dimensionally precise. This method will be used for the miniaturization of optical devices and the integration of photonic circuits. Traditional wet etching can retain the crystal structure of the semiconductor surface, but it falls short of controlling the dimensions. On the other hand, dry etching, represented by reactive ion etching, can achieve precise anisotropic processing, but the surface roughness after processing is relatively high. In the past two decades, metal-assisted chemical etching (MaCE) has attracted much attention due to its combination of the advantages of both methods. MaCE utilizes the catalytic properties of noble metals to accelerate the corrosion of the semiconductor surface in contact with it in solution, forming micron-sized 3D structures. However, after processing, metal particles remain as contaminants on the semiconductor surface or diffuse into the interior. Their removal is very

difficult, which can affect the performance of optical devices such as solar cells and other electronic devices.

Therefore, this thesis proposes the use of nanocarbon materials as catalysts to assist in etching semiconductor surfaces, namely nanocarbon-assisted chemical etching (NCaCE). Specifically, this work combines first-principles theoretical analysis and atomic-level observation by scanning tunneling microscopy to elucidate the correlation between the electronic density distribution and catalytic active sites of nanocarbon catalysts. Nanocarbon catalysts are then used for the microfabrication of semiconductor surfaces, utilizing electrochemical reactions at the semiconductor/nanocarbon interface to oxidize and remove materials, thereby constructing micron-sized 3D structures on the surface. By improving the processing performance of this method, we hope to establish a new method for semiconductor surface processing that does not rely on noble metal catalysts.

A. Scope

This dissertation's findings encompass three main research areas: scanning tunneling microscope (STM) analysis, first-principles calculations, and microfabrication of semiconductor surfaces. Specifically, these areas include:

- Observing the atomic structure of nanoscale graphene sheets, including exfoliated and chemically reduced graphene, using STM.
- Focusing on the unique electronic density distributions near certain defects and their correlation with the structure.
- Conducting calculations on the structural optimization, band structure, and STM image simulations of graphene nanoribbons.
- Developing a novel method of microfabrication on semiconductor surfaces using graphene-based catalysts. This involves the chemical synthesis of graphene-based catalysts, lithography techniques, chemical etching processes, and various surface characterization techniques.

While a significant portion of this research delves into the fundamental properties of graphene, the overarching theme revolves around surface science in semiconductor manufacturing.

B. Approach and Presentation

This thesis proceeds in the sequence of first conducting experimental observations, then theoretical calculations, and finally implementing microfabrication, which is a blend of theory

and practice. We look into the electron density distribution of defects in nanographene using both experiments and computer simulations, which may provide chemically active sites. In the experiment part, scanning tunneling microscopy is used to look at small flakes of monolayer graphene with a focus on electron states close to the Fermi level. The theoretical calculations, on the other hand, solely serve to validate experimental results, utilizing a computational model of an idealized graphene nanoribbon. Our approach starts with the simplest models, thoroughly investigating and deriving reasonable explanations from computational results.

Finally, we focus on the processing of semiconductor surfaces, with a rich content including catalyst synthesis, selection of etching solutions, parameter optimization, and implementation of processing methods. Our plan is to use studying the properties of graphene as a base for practical processing, while the outcomes of processing semiconductor surfaces with graphene catalysts will help guide basic research. Such a loop is crucial for the understanding and practical application of graphene catalysts.

1.3 THESIS ORGANIZATION

A chapter-by-chapter compilation of this thesis is provided below.

- ***Chapter 1 (Introduction)***. A detailed description of the background of semiconductor surface microfabrication has been provided. The basic information for this thesis has been introduced: research objectives, scope, and overall approach.
- ***Chapter 2 (Microfabrication Techniques for Semiconductor Surfaces)***. Non-metal catalyst-assisted chemical etching has been proposed on the basis of the introduction of existing processing techniques for semiconductor surfaces. The research progress of non-metal catalysts has been described, and a feasibility analysis of their application in semiconductor microfabrication has been conducted.
- ***Chapter 3 (Electronic Structure of Finite-size Graphene-based Materials)***. The characterization of small graphene flakes has been conducted using STM. A rectangular-like electronic structure within nanographene has been discovered, and the origin of this unique superlattice has been discussed. Besides, a strategy utilizing computer simulations to verify experimental hypotheses has been proposed.
- ***Chapter 4 (The First-principles Calculations on Armchair-edged Graphene Nanoribbon (AGNR))***. The theoretical framework of first principles and the computational methods used in this thesis have been introduced. The correlation between the calculated STM images of AGNRs and the width of AGNRs, the sample bias used in the calculation, as well as the

wrinkled structure has been investigated. A comparison between the computational results and the experimental results has been provided.

- ***Chapter 5 (Nanocarbon-assisted Chemical Etching on Germanium Surfaces)***. A strategy to enhance the chemical etching of Ge surfaces using nanocarbon materials as catalysts has been proposed. The etching performances in oxygen-dissolved water and H_2O_2 solutions have been investigated. The microscopic mechanisms at the solid-liquid interface during the etching process have been proposed. Suggestions for future work have been provided.
- ***Chapter 6 (Summary and Outlook)***. This thesis is summarized.

REFERENCES

1) J. Bardeen, W. H. Brattain, Phys. Rev. 74 (1948) 230-231.
2) N. Margalit, C. Xiang, S. M. Bowers, A. Bjorlin, R. Blum, J. E. Bowers, Appl. Phys. Lett. 118 (2021) 220501.
3) G. E. Moore, Proceedings of the IEEE 86(1) (1998) 82-85.
4) H. Fujiwara, H. Mori, W. Zhao, K. Khare, C. Lee, X. Peng, V. Joshi, C. Chuang, S. Hsu, T. Hashizume, et al. IEEE International Solid-State Circuits Conference (2024) 27-29.
5) J. R. Tucker, C. Wang, P. S. Carney, Appl. Phys. Lett. 65 (1994) 618-620.
6) E. Pop, S. Sinha, K. E. Goodson, Proceedings of the IEEE 94(8) (2006) 1587-1601.
7) S. Miller, IEEE Journal of Quantum Electronics 8(2) (1972) 199-205.
8) R. A. Soref, Proceedings of the IEEE 81(12) (1993) 1687-1706.
9) A. L. Washburn, R. C. Bailey, Analyst 136 (2011) 227-236.
10) H. Park, A. W. Fang, R. Jones, O. Cohen, O. Raday, M. N. Sysak, M. J. Paniccia, J. E. Bowers, Optics Express 15(10) (2007) 6044-6052.
11) J. Liu, X. Sun, D. Pan, X. Wang, L. C. Kimerling, T. L. Koch, J. Michel, Optics Express 15(18) (2007) 11272-11277.
12) Y. Kang, H.-D. Liu, M. Morse, M. J. Paniccia, M. Zadka, S. Litski, G. Sarid, A. Pauchard, Y.-H. Kuo, H. W. Chen, et al. Nature Photonics 3 (2009) 59-63.
13) G. Son, S. Han, J. Park, K. Kwon, K. Yu, Nanophotonics 7(12) (2018) 1845-1864.
14) Y. Meng, Y. Chen, L. Lu, Y. Ding, A. Cusano, J. A. Fan, Q. Hu, K. Wang, Z. Xie, Z. Liu, et al. Light: Science & Application 10 (2021) 235.
15) S. Shekhar, W. Bogaerts, L. Chrostowski, J. E. Bowers, M. Hochberg, R. Soref, B. J. Shastri, Nat. Commun. 15 (2024) 751.
16) Y. Arakawa, T. Nakamura, Y. Urino, T. Fujita, IEEE Communications Magazine 51 (2013)

72-77.

17) S. Y. Siew, B. Li, F. Gao, H. Y. Zheng, W. Zhang, P. Guo, S. W. Xie, A. Song, B. Dong, L. W. Luo, et al. Journal of Lightwave Technology 39(13) (2021) 4374-4389.

18) S. Liu, J. Feng, Y. Tian, H. Zhao, L. Jin, B. Ouyang, J. Zhu, J. Guo, Frontiers of Optoelectronics 15 (2022) 9.

19) M. Li, W. H. P. Pernice, C. Xiong, T. Baehr-Jones, M. Hochberg, H. X. Tang, Nature 456 (2008) 480-484.

20) J. Hu, X. Sun, A. Agarwal, L. Kimerling, Journal Optics Society America B 26 (2009) 1032-1041.

21) M. Iqbal, M. A. Gleeson, B. Spaugh, F. Tybor, W. G. Gunn, M. Hochberg, T. Baehr-Jones, R. C. Bailey, L. Cary Gunn, IEEE Journal of Selected Topics in Quantum Electronics 16 (2010) 654-661.

22) M. Foster, A. Turner, M. Lipson, A. Gaeta, Optics Express 16 (2008) 1300-1320.

23) A. A. Trusov, I. P. Prikhodko, S. A. Zotov, A. R. Schofield, A. M. Shkel, 2010 IEEE Sensors (2010) 864-867.

24) M. Guilln-Torres, E. Cretu, N. A. F. Jaeger, L. Chrostowski, Journal of Lightwave Technology 30 (2012) 1802-1817.

25) J. Capmany, D. Novak, Nature Photonics 1 (2007) 319-330.

26) M. Burla, L. R. Cortés, M. Li, X. Wang, L. Chrostowski, J. Azaña, Optics Express 21 (2013) 25120-25147.

27) M. Ko, J.-S. Youn, M.-J. Lee, K.-C. Choi, H. Rucker, W.-Y. Choi, IEEE Photonics Technology Letters 24 (2012) 1112-1114.

28) C. R. Doerr, L. L. Buhl, Y. Baeyens, R. Aroca, S. Chandrasekhar, X. Liu, L. Chen, Y.-K. Chen, IEEE Photonics Technology Letters 23(2011) 762-764.

29) H. Y. Liu, T. Wang, Q. Jiang, R. Hogg, F. Tutu, F. Pozzi, A. Seeds, Nature Photonics 5 (2011) 416-419.

30) F. Aflatouni, H. Hashemi, Optics Letters 37 (2012) 196-198.

31) R. B. Wehrspohn, S. L. Schweizer, J. Schilling, T. Geppert, C. Jamois, R. Glatthaar, P. Hahn, A. Feisst, A. Lambrecht, Advances in Design, Fabrication, and Characterization, K. Busch, S. Lalkes, R. B. Wehrspohn, H. Fall (eds.), Photonic Crystals: Wiley-VCH Verlag GmbH (2006) 238-246.

32) T. Baehr-Jones, R. Ding, A. Ayazi, T. Pinguet, M. Streahinsky, N. Harris, J. Li, L. He, M. Gould, Y. Zhang, et al. Preprint at https://doi.org/10.48550/arXiv.1203.0767 .

33) K. Lee, D. Lim, L. Kimerling, J. Shin, F. Cerrina, Optics Letters 26 (2001) 1888-1890.

34) F. Grillot, L. Vivien, S. Laval, D. Pascal, E. Cassan, IEEE Photonics Technology Letters 16 (2004) 1661-1663.

CHAPTER

2

MICROFABRICATION TECHNIQUES FOR SEMICONDUCTOR SURFACES

The electronics industry, the greatest sector of the global economy, is built on semiconductor devices. Numerous devices are inseparable from semiconductor technology, or semiconductor manufacturing technology. Many important manufacturing technologies can be traced back to processes invented centuries ago that predate the rise of the electronics industry. For instance, the lithography process was invented in 1798, and in Greek, “lith-” means stone. This is because the earliest lithography process involved transferring patterns or images from a stone plate.

This chapter begins with a description of semiconductor materials and semiconductor devices (Sec. 2.1). Some basic manufacturing techniques, focusing on process characteristics, follow in Sec. 2.2. Dry etching and wet etching are listed in Sec. 2.2C, and their respective processing equipment, mechanisms, strengths, and weaknesses are introduced. The emergence of metal-assisted chemical etching, its applications, our reports using MaCE, and the challenges faced are presented in Sec. 2.3. A novel manufacturing technique that does not use precious metals and the introduction of nanocarbon materials as catalysts are introduced in Sec. 2.4. Finally, we return to the overall research strategy of this thesis in Sec. 2.5 and summarize this chapter in Sec. 2.6.

2.1 INTRODUCTION

Microfabrication processes enable to precisely process materials at microscopic scales, aiming to create complex semiconductor devices that cannot be realized in conventional fabrication techniques. The processing range covers from millimeters to micrometers, and even some fine structures reach the nanometer level. These technologies are diverse and typically require the integration of multiple techniques and the rational design of procedures to achieve highly integrated device structures. To generate economic benefits, each process step must be capable of mass processing a large number of devices to reduce costs. Furthermore, for microfabrication involving hundreds of process steps, the precision of geometric control during processing determines the yield and performance of the final product. Examples include micromachined pressure sensors and accelerometers [1,2] that have been successfully applied in the automotive industry.

Besides the processing dimensions, microfabrication techniques for semiconductors differ significantly from traditional mechanical processing in terms of precision and technical complexity. In the manufacturing process of semiconductor devices, a sequence of standard semiconductor fabrication technologies and specialized surface microfabrication processes are

arranged. For the production of specific devices, the processing flow must be meticulously defined and strictly regulated. By far, the most important aspect of the microelectronics industry has been the microfabrication processes [3)] of semiconductor surfaces. Among these, the most well-known is CMOS technology, which is a key innovation. Generally, in semiconductor surface microfabrication, there are essentially two categories: formation and removal. Formation refers to the processes of creating specific structures or features on the semiconductor surface, such as adding material layers, doping, and annealing. Removal processes include etching, photoresist stripping, polishing, and cleaning. In the next section, we introduce several commonly used fabrication techniques in the field of microelectronics. These techniques are frequently utilized in this dissertation to create three-dimensional (3D) microstructures on semiconductor surfaces.

2.2 BASIC MICROFABRICATION PROCESSES

Today's semiconductor surface microfabrication processes overlap to a large extent with the technologies used in IC fabrication. This section briefly introduces several of the basic microfabrication technologies. To create complex 3D structures on the surface of a semiconductor, layer-by-layer fabrication is required, as shown in the flow diagram in Figure 2.1. Here, the cleaning and polishing of the wafer are not shown. The primary purpose of the film deposition process is to form a protective layer on the semiconductor surface to ensure that the covered areas are not processed. Photolithography is one of the key technologies in semiconductor surface microfabrication. It is responsible for forming the photoresist patterns on the semiconductor surface. These patterns provide the processing windows for subsequent steps, such as material removal. Doping involves ion implantation to alter the properties of the semiconductor substrate. Etching is the process of removing portions of material from the surface. Note that complete IC fabrication usually includes hundreds of (including repetitive) steps. Next, each technology shown in Figure 2.1 was subdivided into a variety of processing methods with different principles that are constantly evolving, while only the representative methods were described.

A. Thin Film Deposition

Figure 2.2 shows the layered structure formed on a silicon substrate. These thin films can be formed by chemical vapor deposition (CVD), which mainly utilizes chemical reactions of gaseous precursors under high temperatures and other conditions. Physical vapor deposition (PVD) is also a typical thin film deposition method, generally involving the vaporization and subsequent

solidification of the target material. For polymers such as photoresist, spin coating or spray coating are also good choices.

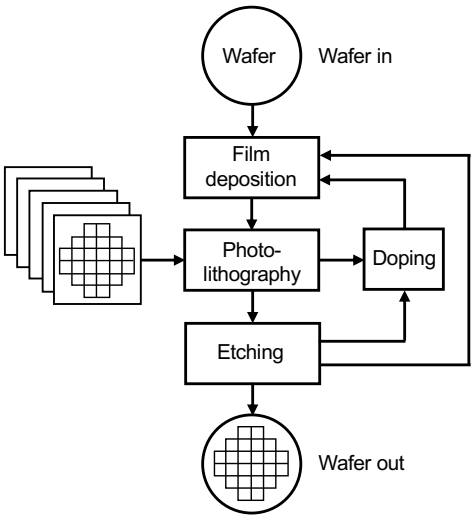

Figure 2.1 A flow diagram of typical methods used in IC fabrication processes [4].

According to the types of thin film materials, they are mainly divided into insulating layers, metal layers, semiconductor layers, and polymer layers. Common insulating films include silicon dioxide (SiO_2), aluminum oxide (Al_2O_3), and silicon nitride (Si_3N_4). Their functions are to provide electrical isolation between different circuits and protect material surfaces from physical or chemical damage. A SiO_2 layer is usually obtained through thermal growth or high-temperature deposition on Si substrates, while silicon nitride is formed by CVD. In the microelectronics industry, low-resistance metals such as copper (Cu) are used as electrical interconnect materials, including electrode materials. Other metals like titanium (Ti), tungsten (W), and the earlier widely used aluminum (Al), as well as some metal compounds, are also common. In addition to conductivity, the chemical stability, high-temperature resistance, and compatibility with other materials of the metal films are important factors to consider in the process. These metal layers are often deposited using PVD or CVD. In semiconductor films, Si material layers include polycrystalline silicon and amorphous silicon. Non-Si semiconductor layers mainly include gallium nitride (GaN), indium phosphide (InP), germanium (Ge), etc. The two main acquisition methods are atomic layer deposition (ALD) and epitaxial growth. In photolithography, it is common to drop a photoresist solution onto a substrate and then spin at high speed to create a uniform mask material. Additionally, microcontact printing has also been used to deposit such

polymer films, allowing for the formation of special patterns.

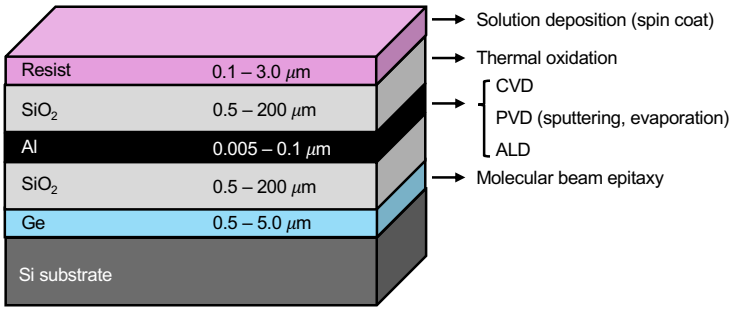

Figure 2.2 Schematic of build-up structures using different deposition techniques and materials, along with typical layer thickness.

B. Photolithography

Many top-down miniaturization methods begin with lithography, a technique for printing images and text on material surfaces. In general terms, lithography that uses light is referred to as photolithography, which is the most common type. As summarized in the steps in Figure 2.3, photolithography transfers the pattern from the mask to the resist first, then to the underlying thin film. A substrate (after depositing a film) is coated with a photoresist layer. After exposure and development, the pattern shown in Figure 2.3b was obtained. Positive photoresist was used here, so the photoresist in the exposed areas was removed, revealing the substrate underneath. The pattern on the photomask is reproduced in the photoresist layer, as shown in Figure 2.3c. At this stage, the substrate is placed in a solution that only etches the film but does not damage the photoresist or the substrate, and the result is shown in Figure 2.3d. Once the excess photoresist is removed, the complete photolithography process is finished. In practical applications, the process steps are often more complex than those shown in Figure 2.3 and may involve multiple times of film deposition and photolithography to create intricate patterns.

Photoresist and Photomask

Photoresists typically consist of three components: a polymer, a sensitizer containing a photoactive compound, and solvents. Photoresists have positive and negative types. In the case of a positive photoresist, exposure causes the photoactive compound to undergo photochemical reactions, thereby increasing the solubility of the photoresist (polymer). The developer will dissolve this part of the photoresist, leaving the unexposed areas intact. The mask used in

photolithography is an optically transparent glass or quartz plate with a thin metal layer (usually chromium) coated on one side. The pattern on the mask is created through another process. In use, a mask is placed between the light source and the substrate coated with photoresist. The mask can either be in direct contact with the photoresist or very close to it. Typically, photolithography replicates the mask pattern onto the photoresist in a 1:1 ratio. However, projection printing can further reduce the mask pattern proportionally using imaging lenses.

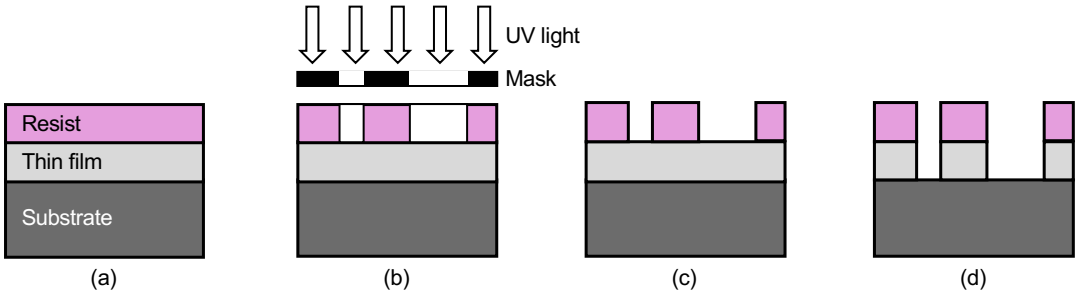

Figure 2.3 Schematic of a photolithographic process sequence for structuring a thin-film layer. (a) apply photoresist, (b) expose photoresist, (c) develop photoresist, and (d) transfer pattern.

Spinning Resist and Soft Baking

In Figure 2.3a, a uniform layer of photoresist is coated on the substrate before exposure. Sometimes, to enhance the adhesion of the photoresist to the substrate, an oxide layer is thermally grown on the substrate or an adhesion promoter is spin-coated. Then, the photoresist is uniformly spin-coated onto the substrate surface. The spinning speed is several thousand rotations per minute, and the thickness of the photoresist is approximately a few micrometers. The thickness of the resist requires careful consideration of multiple parameters during the photolithography process by the experimenter. The uniformity of the photoresist needs to be sufficiently good; otherwise, it will affect the subsequent exposure and pattern printing. Common issues include little resist leaving exposed areas of the substrate, and excessive application of resist results in poor surface uniformity of the photoresist film. As previously mentioned, to facilitate coating, the photoresist contains a certain amount of solvent. After spin coating, a soft bake (prebake) is performed to remove these solvents, thereby increasing the strength of the photoresist and its adhesion to the substrate.

Alignment, Exposure, and Postexposure Treatment

After the substrate is coated with photoresist, it is ready for exposure. A crucial step before exposure is aligning the substrate with the mask, especially in multilayer and complex designs that require precise positioning. Common alignment methods include manual adjustment and optical alignment, while some advanced equipment may have automatic alignment systems. During exposure, light of a specific wavelength, intensity, and uniformity is emitted from the light source. These lights will be partially blocked by the mask, while the other part will pass through the transparent pattern windows on the mask and irradiate the photoresist. The light source used for exposure is typically ultraviolet (UV) light, and shorter wavelengths allow for smaller feature sizes. In exposure, there are two important parameters: exposure time and light intensity. These determine the exposure dose on the surface of the photoresist. Both overexposure and underexposure are undesirable. As the intensity of the light source may decrease, become uneven, and become unstable over time, it is necessary to regularly check the light source. As previously introduced, the photoresist in the exposed area undergoes a photochemical reaction, changing its solubility in the developer solution. Postexposure baking is very necessary, as it can further enhance the stability of the photoresist, promote the completion of the reactions occurring during exposure, and reduce the impact of standing waves within the photoresist.

Development and Postbaking

The development process involves selectively dissolving either the exposed or unexposed areas of the photoresist, depending on whether a positive or negative photoresist is used. Typically, the substrate is immersed in the developer solution for a period of time. Depending on the type of photoresist, the developer solution generally uses either an alkaline solution or an organic solution. During development, the solution can be stirred. After development, deionized water is used to rinse the substrate to remove any residual developer and dissolved photoresist from the surface. Subsequently, methods such as nitrogen drying can be employed to remove water and other solutions from the substrate. It is important to note that small patterns may have residual photoresist, and the photoresist that is intended to be retained may also experience detachment. In addition to immersion development, there are also spray development and dry development based on vapor-phase processes. If subsequent photolithography steps involve wet processes, an additional baking step, known as post-bake or hard bake, is required. This step not only strengthens the photoresist but also reduces the solvent content in the photoresist. The developer solution used in the previous step may cause the photoresist to swell, and hard baking helps to minimize pattern distortion. The postbaking temperature is typically around 120 °C, which is higher than the prebake (soft baking) temperature, and it requires a longer baking time. After post baking, the substrate should be cooled gradually to avoid adverse effects from sudden temperature changes.

Resist Stripping

The final step in photolithography is resist stripping (or lift-off), which occurs after Figure 2.3d. The purpose of this step is to remove all the resist and any other substances covering the resist from the substrate for subsequent processing steps. If this step is not completed successfully, it will undoubtedly introduce impurities and reduce process quality. In wet stripping, the entire substrate is immersed in an organic solvent or a strong acid/alkaline solution. Commonly used organic solvents in experiments include acetone and isopropanol. During the stripping process, it is essential not to damage the substrate or other materials that need to be preserved. After stripping, the substrate needs to be cleaned with deionized water. Drying methods can include blowing nitrogen or natural drying. In many cases, wet stripping may not completely remove the photoresist, and organic solvents and dissolved contaminants may remain on the substrate surface. Compared to wet stripping, the dry stripping process is easier to control, which is why it is becoming increasingly popular. The substrate surface will be cleaner after dry stripping using plasma methods. However, one drawback is that it may cause damage to the substrate surface.

Although not detailed in this section, inspection and metrology techniques play a vital role in various stages of the lithography process. The resulting substrate with etched windows (exposed areas) will be processed in the next step. We will explain this part in detail in Sec. 2.2C.

C. Etching

In semiconductor manufacturing, there are many scenarios where material removal is necessary. Etching, an ancient technique that utilizes the phenomenon of corrosion, is widely applied in many areas. The precise control of this technique and its integration with other processes are fundamental steps in the manufacturing of semiconductor devices in the microelectronics industry. For example, after obtaining the result shown in Figure 2.3c through photolithography, etching can be used to create three-dimensional structures on the semiconductor surface. In this step, the photoresist pattern on the surface acts as a mask, as illustrated in Figure 2.4. In some scenarios, an insulating layer is also used to protect the surface from being etched, which is more durable.

Wet etching using liquid-phase chemical substances and dry etching using plasma or gas-phase chemical substances are the most common. The difference between the two lies in the phase of the substance used for etching. There are three important criteria when selecting a specific etching method:

- Etching rate: How fast the material being processed is removed.
- Isotropy and Anisotropy (as shown in Figure 2.4): The definition of isotropic etching and anisotropic etching lies in the relationship between etching rate and direction. The former refers to having the same etching rate in all directions, while the latter exhibits different

etching rates in different directions.

- Selectivity: The term “selectivity” describes the etching process that maintains a low etching rate for materials not intended for etching while having a high etching rate for the target material.

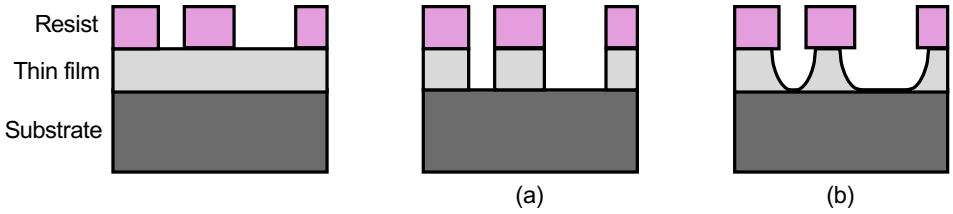

Figure 2.4 Schematic of (a) anisotropic and (b) isotropic thin-film etching.

Wet etching is generally isotropic [5,6], but anisotropy can also be achieved in some cases [7-9]. However, dry etching is generally anisotropic and allows for better pattern transfer. Next, we will discuss these two methods respectively.

Dry Etching

Dry etching is a method that utilizes plasma or other high-energy particles to remove material and is widely used in semiconductor manufacturing. This method can precisely control the etching process, enabling the fabrication of micro- and nanostructures on semiconductor surfaces. Dry etching encompasses a variety of technologies, and here we introduce a typical one: reactive ion etching (RIE) [10].

In RIE, reaction gases such as CF_4, SF_6, and Cl_2 are ionized under the influence of a high-frequency electric field, generating plasma at low pressure. The plasma ionizes and dissociates the reaction gas molecules, with the resulting ions participating in the etching process. In the electric field, the ions accelerate towards the substrate, causing physical sputtering of the material. At the same time, reactive species in the plasma chemically react with the material. In other words, RIE combines both physical and chemical mechanisms to remove material.

Figure 2.5a introduces common RIE equipment. The main components of an RIE system include an radio frequency (RF) or microwave power supply, a vacuum chamber, a gas delivery system, and a substrate holder or chuck. The RF power supply is responsible for generating the plasma and maintaining a stable plasma state. The power settings control the energy input to the plasma; the higher the power, the greater the plasma density and the faster the etch rate. In addition

to power, the frequency of the power supply also affects the etching results. The bias voltage in the system is used to control the direction of ion movement and to accelerate the ions towards the material's surface. The magnitude of the bias voltage affects various aspects of the etching process, including etch rate, etch selectivity, and etch profile. Through the gas delivery system, reactive gases such as CF4 are introduced into the vacuum chamber. In the vacuum chamber, plasma is continuously generated at low pressure. The low-pressure environment facilitates the ionization of the gas, producing a large number of high-energy particles. The gas flow rate determines the gas content in the vacuum chamber and affects the overall reaction in the system. Therefore, it can be said that there are many etching parameters in RIE, and adjusting these parameters properly is crucial for achieving high precision and ideal processing.

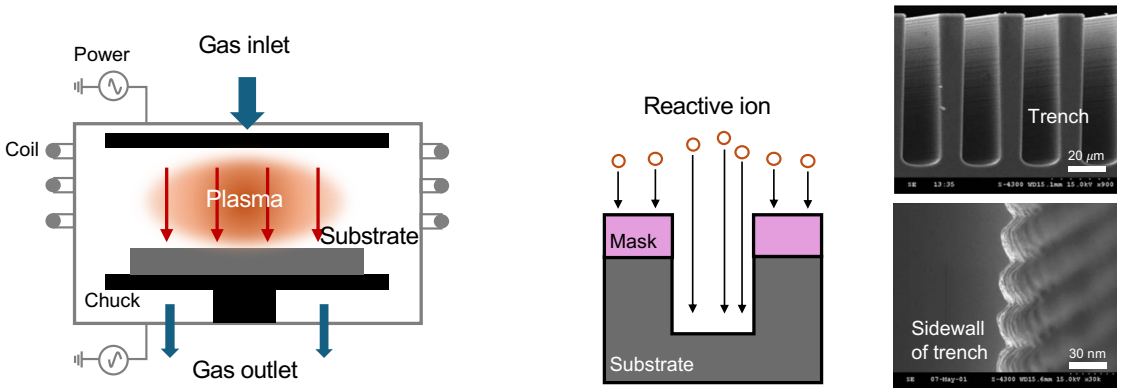

Figure 2.5 (a) Schematic of ICP-RIE. (b) Schematic of plasma etching mechanism, and the etched trench [11].

As a typical representative of dry etching, RIE has several advantages. As shown in Figure 2.5b, a major advantage is its ability to achieve anisotropic processing, i.e., vertical etching of materials, which is particularly crucial in the fabrication of high aspect ratio structures. However, the drawbacks of this type of dry etching include the high requirements for equipment and the numerous process parameters that interact with each other. In addition, RIE is likely to cause damage [11] to the material, as shown in Figure 2.5b.

Wet Etching

Wet etching, also known as wet chemical etching, is a processing method that utilizes liquid

chemical reagents to etch the surface of materials. It is suitable for processing the entire surface of a wafer and has wide applications [8,12] in microelectromechanical systems (MEMS) and semiconductor manufacturing. The operation of wet etching is very simple. As shown in Figure 2.6a, the material is immersed in a solution containing specific chemicals. The chemical reagents can be acidic solutions, alkaline solutions, or their mixtures. In such a liquid phase, a chemical reaction occurs at the interface between the substrate and the etchant, and material removal is accomplished through the dissolution of the reaction products. The etching rate can be analyzed through the microscopic reaction kinetics.

Wet etching is usually isotropic [5,6] because the chemical reactions at the solid-liquid interface proceed equally in different directions, resulting in the etching characteristics shown in Figure 2.6b. There are some exceptions due to differences in the crystal structure of Si in different directions, where the etching rate exhibits orientation dependence in certain solutions (e.g., potassium hydroxide [8,9]). This unique phenomenon is utilized in the anisotropic wet etching of material surfaces. However, it can only be applied to specific materials and specific orientations, which greatly limits its applications.

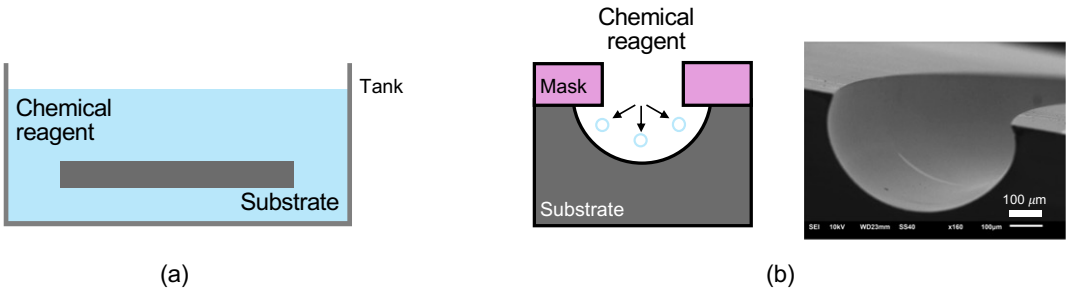

Figure 2.6 (a) Schematic of wet chemical etching. (b) Schematic of wet etching mechanism, and the etched channel [13].

The main components of wet etching are chemical reagent containers, which are generally relatively simple. Etching systems typically come with temperature control functions, and stirring devices are also available as options. Since wet etching is driven by chemical reactions, several key parameters are related to the etchant. Besides the obvious solution temperature, factors such as the acidity or alkalinity of the etchant and its concentration in the solution can have complex and significant effects on the etching of the substrate. Stirring devices are primarily considered for material exchange in chemical reactions, ensuring uniform etching across the substrate.

Overall, wet etching is somewhat inferior in terms of etching results, mainly due to its slower etch rate and poor controllability. The lack of controllability is primarily reflected in the inability of isotropic etching to achieve vertical processing of structures like trenches, and it often results in significant dimensional errors. These drawbacks indicate that this method is not suitable for precise processing and three-dimensional processing in semiconductor manufacturing. However, wet etching is still indispensable. For example, wet etching may have high etch selectivity for different materials. By designing multilayer structures with different materials and utilizing the high etch rate of wet etching for some of these materials, precise fabrication of certain nanoscale, three-dimensional structures can be achieved. Even in the manufacturing of advanced transistors, there is a step that takes advantage of this characteristic. Additionally, the simplicity, ease of operation, and high processing efficiency of wet etching are advantageous in terms of production costs.

Table 2.1 Comparison of dry and wet etching techniques

	Dry etching		Wet etching	
Etching factors	RIE	Ion etching	Chemical	Electrochemical
Driving force	Reactive gases	Plasma	Etching solution	External current
Environment	Vacuum	Vacuum	Acidic/alkaline	Neutral salt solution
Rate	~1000 Å/min	~100 Å/min	~1 μm/min	10 μm/min
Selectivity	High	Poor	Very high	Very high
Wall slope control	Anisotropic	Directional	Isotropic	Better than Chemical
Critical dimension control	Very good (< 0.1 μm)		Poor	
Radiation damage	Can be severe		None	
Cost	High	High	Low	Moderate

Comparison of Dry and Wet Etching

Understanding the differences between dry and wet etching methods is critical for specific applications in semiconductor fabrication. Table 2.1 details the characteristics, advantages, and disadvantages of these two methods. You can select the most appropriate etching method by carefully considering the material properties, desired feature size, process requirements, environmental impact, and cost.

Next, a new semiconductor surface processing technique different from the above-mentioned two methods has attracted attention: metal-assisted chemical etching. In Sec. 2.3, we will give detailed information on the history, characteristics, processing principles, applications, and challenges of this technique.

2.3 METAL-ASSISTED CHEMICAL ETCHING

A. Introduction

Since the year 2000, Li et al. [14] first discovered metal-assisted chemical etching (MaCE). Noble metals such as gold, platinum, and silver act as catalysts in the reaction, determining the feature sizes formed during the etching process. Like wet etching, the chemical reactions in MaCE occur at the interface between the substrate and the solution. Specifically, in areas covered by metal, the semiconductor surface is preferentially removed. The metal continuously catalyzes this etching reaction, forming deep holes or grooves, resulting in vertical processing. In recent years, MaCE has developed rapidly for several reasons. Firstly, it is low-cost, easy to operate, and produces high crystalline quality of the processed surface. Secondly, it combines the anisotropy and high processing rate of dry etching. Thirdly, it is highly flexible, with no apparent limitations on feature sizes, enabling the fabrication of nanoscale straight, well-defined pores, or lines.

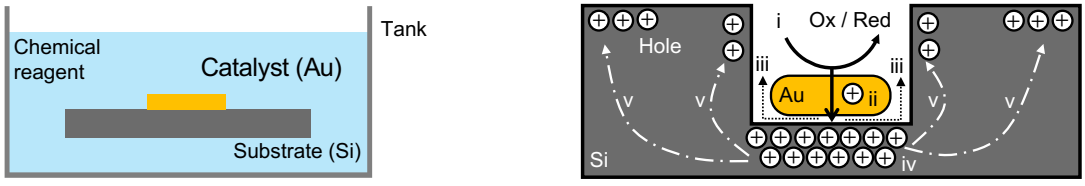

Figure 2.7 (a) Schematic of MaCE. (b) Schematic of MaCE mechanism [15].

Here, we take classical MACE on the surface of Si as an example. The etchants used are hydrogen fluoride (HF) and hydrogen peroxide (H_2O_2). It is well accepted that the following reactions will take place.

- Cathode reaction (at metal):

$$H_2O_2 + 2H^+ \rightarrow 2H_2O + 2h^+ \quad (2.1)$$

$$2H^+ + 2e^- \rightarrow H_2 \uparrow \quad (2.2)$$

- Anode reaction (at Si):

$$Si + 4h^+ + 4HF \rightarrow SiF_4 + 4H^+ \quad (2.3)$$

$$SiF_4 + 2HF \rightarrow H_2SiF_6 \quad (2.4)$$

- Overall reaction:

$$Si + H_2O_2 + 6HF \rightarrow 2H_2O + H_2SiF_4 + H_2 \uparrow \quad (2.5)$$

Table 2.2 Comparison of MaCE using catalysts formed gas phase deposited metal pattern and solution phase metal network [16)]

	Evaporated or sputtered metal catalyst	Solution based metal catalyst
Pattern size	Micro and nanoscale	Nanoscale only
Pattern size distribution	Uniform, determined by lithography	Random, large
Pattern site control	Complete control	Not feasible
Patterned structure	Versatile	Interconnected network
Etch rate	Fast	Slow
Scalability	Good	Good
Cost	Relatively high	Low

MaCE deposits the metal catalyst on the substrate's surface in some manner, as illustrated in Figure 2.7a, and then submerges the substrate in a container containing the chemical reagents. In Figure 2.7b, we explain the etching process on a Si substrate:

- i. The oxidant in the etchant is reduced; this reaction is catalyzed by the metal film.
- ii. The holes generated due to the reduction will promote oxidation of the underlying Si. The path of the hole movement is indicated in the figure.

- iii. Silicon oxide dissolves in HF and will move in the direction indicated by the arrows along with the solution.
- iv. A continuous catalytic reaction creates a large number of holes directly below the precious metal, resulting in an etch rate much faster than that of the bare Si surface.
- v. A portion of the holes that are not consumed in time diffuses into the areas without covering metals, which leads to the formation of microporous Si in these areas.

Using the phenomenon shown in Figure 2.7, different surface structures can be obtained by altering the pattern of the metal film. This process involves the thin film deposition and photolithography techniques we discussed earlier. The former forms a thin film of metal that is tens of nanometers thick, whereas the latter forms metal particles. A detailed comparison of these two types of metal catalysts is presented in Table 2.2. Regarding the oxidant in the etchant, the usual choices are H_2O_2, HNO_3, $KMnO_4$, or $KBrO_3$. HF was often used to remove the oxidants generated during the etching process. The most commonly used precious metals are Ag and Au. In addition, the concentration of chemical substances, temperature, type of semiconductor substrate, etc. will all affect the etching performance. This year, with the development of MaCE, there are more and more applications for semiconductors other than Si, such as Ge, InP, etc.

B. Application

Table 2.3 Typical characteristics of three etching techniques for semiconductors [16)]

	Wet etching	Dry etching	MaCE
Directionality	Isotropic	Anisotropic	Anisotropic
Aspect ratio	Low	Medium	High
Ion induced damage	None	Mild to severe	None
Crystal orientation dependence	Some	Weak	Weak
Etch rate	Fast	Slow	Fast
Sidewall smoothness	Smooth	Not smooth	Smooth or rough
Chemical selectivity	Good	Poor	Depends
Cost	Low	High	Low

Before we talk about the application of MaCE, we first list the characteristics of MaCE in Table

2.3, which overcomes the problem of traditional wet etching that cannot process the surface of the substrate vertically and produces nanowire structures with very high aspect ratios and individual nanowire diameters down to tens of nanometers, which meets the majority of needs. In addition, MaCE has the advantage of producing nanostructures with low surface damage and a high etching rate.

Next, we summarize the applications of nanowire structures produced by MaCE. Other structures, such as porous structures, will not be elaborated on too much. First, we introduce some typical applications of silicon nanowire (SiNW) structures fabricated on Si surfaces.

Anti-Reflection and Photovoltaic Devices

The simple formation of SiNW arrays on crystalline silicon (c-Si) surfaces can significantly reduce visible light reflection. Such anti-reflection (AR) structures can be used in light-harvesting devices (i.e., solar cells). In the photovoltaic industry, these AR structures can also play a significant role. Compared to a flat surface, the three-dimensional structure of a SiNW array increases the surface area of the semiconductor, undoubtedly increasing the light path length and absorption. Additionally, high aspect ratio structures can improve carrier collection. Another research direction is Si-organic hybrid solar cells. It combines high-performance inorganic Si materials with organic materials. Hybrid solar cells are good candidates for light-weight flexible solar cells. According to plans, such novel solar cells will occupy a significant proportion of future energy development strategies.

Energy Storage

Si also has great potential applications in energy storage materials, such as electrodes for rechargeable lithium-ion batteries. The key issue hindering this application is the instability of Si in these devices. Specifically, during use, it exhibits volume expansion and brittle properties. One current solution is to create nanostructures on the Si surface. Another type of energy storage device is the supercapacitor, where structures like silicon nanowires can increase their charge storage capacity. Moreover, it can enable rapid charge and discharge processes and enhance the structural stability of the electrode, thereby significantly improving the performance of the supercapacitor.

Nanoelectronics and Nanophotonics

The porous segment in c-Si nanowires can be used as photon-triggered transistors. Silicon nanowires can be used as channel materials in field-effect transistors due to their high surface-to-volume ratio and quantum effects, which enable high performance at the nanoscale. These transistors exhibit higher switching speeds and lower power consumption, making them suitable for high-performance computing electronic devices. Additionally, nanoscale silicon nanowires can effectively capture incident light and convert it into electrical signals, making them suitable

for various optoelectronic applications, such as high-sensitivity photodetectors.

Upon careful observation of SiNWs fabricated by MaCE, many small pores can be seen on the sidewalls. Such features actually enhance their application in optoelectronic devices. SiNW-based photodetectors exhibit excellent responsivity across different wavelength ranges. When the size of silicon reaches the nanoscale, both photoluminescence and electroluminescence performance can be enhanced. In some nonlinear optical devices, they can amplify optical signals.

Gas Sensors

Various SiNW based gas sensors, such as O_2, H_2, NH_3, NO_2, and CH_4, have been reported in the literature. When gas molecules come into contact with the surface of SiNWs, they can change the conductivity of the nanowires. Additionally, some chemical reactions may occur. By analyzing these changes, the presence and concentration of specific gases can be monitored. In the fabrication of SiNW gas sensors, the diameter, length, and surface morphology of the nanowires can be controlled by adjusting the etching parameters. Doping and surface functionalization are also commonly used methods to enhance the detection performance of the sensors. These sensors have potential applications in detecting harmful gases, pollutants, and even in the medical field. However, the integration of SiNW gas sensors remains a significant challenge.

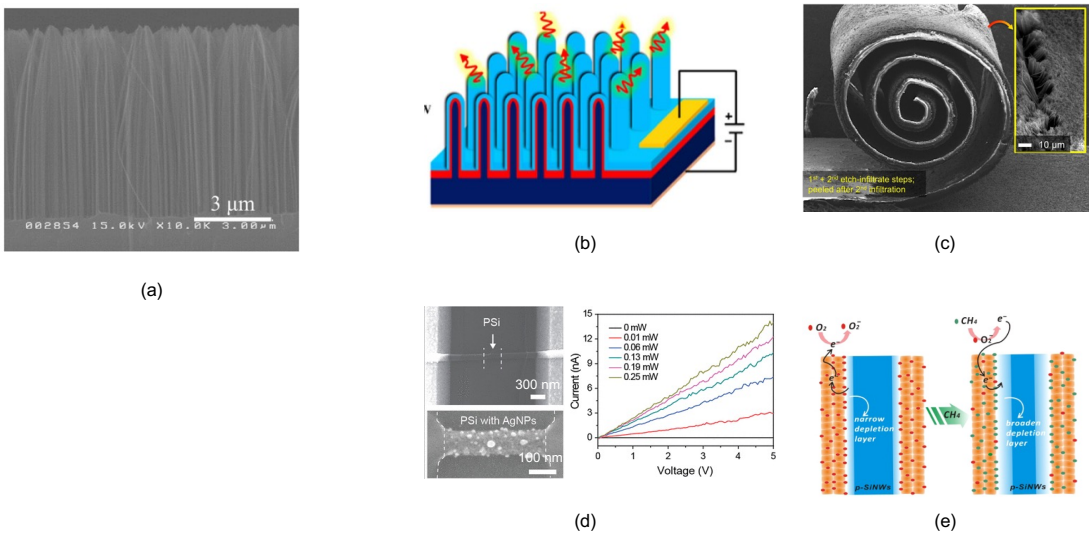

Figure 2.8 SiNW structures [17] (a) and their applications in photovoltaic [18] (b), energy storage [19] (c), nanoelectronics [20] (d), and gas sensors [21] (e).

The above-mentioned applications of SiNW structures are summarized in Figure 2.8. In

addition, MaCE has also made achievements in the fields of energy harvesting, biosensors and biomedicine, and photoelectrochemistry. More and more MaCE research explores different semiconductor materials. This undoubtedly broadens the application of MaCE technology and promotes the progress of this technology and the creation of new technologies.

C. Our MaCE on Ge and The Issues

Ge is also a promising semiconductor material, especially in the field of nanophotonics. For example, Ge has a narrower bandgap than Si, and epitaxially grown Ge on Si is expected to be used in lasers for optical integration. Wet etching of the Ge surface is not as effective as it is on Si materials. This is because the chemically produced Ge oxide (GeO_2) in solutions is permeable and soluble in water. After immersion in a H_2O_2 solution, pits will be formed on the Ge surface to varying degrees (depending on the concentration of the solution). For a flat Ge surface, traditional chemical mechanical polishing with an alkaline solution is not an ideal method.

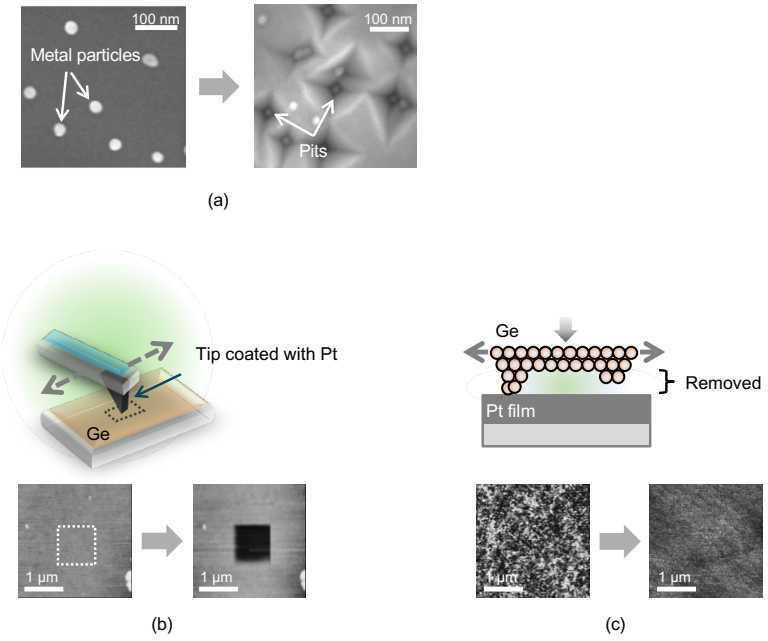

Figure 2.9 Our reports [22-24] on MaCE of Ge surfaces in O_2-containg water: (a) pit formation, (b) patterning, and (c) flattening.

In the past, we have attempted to apply MaCE to the processing of Ge surfaces. We successfully

used MaCE to create various etching patterns in our experiments. In MaCE, the catalysts used are noble metals such as Pt and Ag, and the etching is carried out in an oxygen-containing water. Furthermore, we demonstrated that this technique can be used for the planarization of semiconductor surfaces and compared it with traditional chemical mechanical polishing. The treated Ge surface exhibited ideal surface roughness, and high pressure was avoided during processing. The catalytic activity of the metals is considered to play a crucial role in achieving such processing results. These results of chemical etching of Ge enhanced by noble metal catalysis in water are briefly summarized in Figure 2.9.

The Issues

This is the same problem encountered in other MaCE research. A number of studies have shown that aqua regia can remove metal catalysts, such as Pt and Ag, from the bottom of the hollows that have been processed [25]. However, it is likely that the metal catalyst will still be on the semiconductor's surface (as shown in Figure 2.10) or inside it as metal particles. In addition, aqua regia, being a potent oxidizer solution, leads to serious damage to the surface nanostructures after processing.

Besides the above-mentioned problem, MaCE involves the deposition of noble metals on semiconductor surfaces, which requires the use of vacuum equipment. This often has cost implications, especially in mass production. In addition, as we mentioned earlier, the processing of Ge surfaces requires careful selection of etching solutions like acid or alkaline. These issues are illustrated in Figure 2.10.

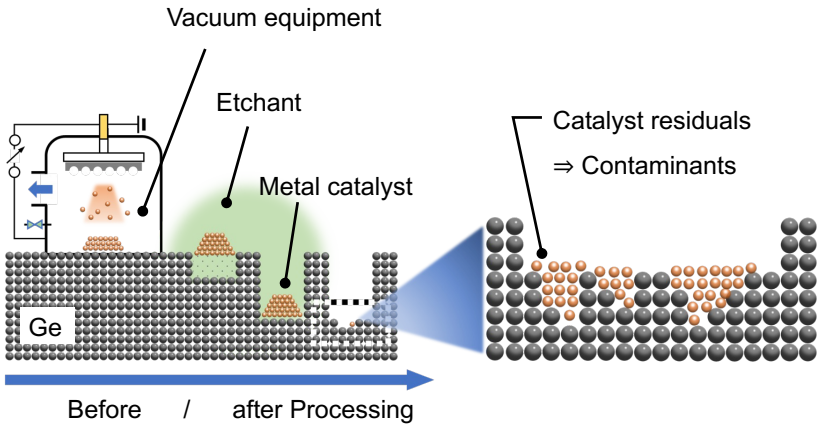

Figure 2.10 The challenging issues in MaCE.

Our current research topic is addressing the most significant problem: metal residues on the

surface after processing. In order to continue the advantages of this particular wet process of MaCE, we are focusing our goal on the replacement of metal catalysts. This new non-metallic material must be able to play a role similar to that of a metal catalyst and combine well with the wet etching technology. Nanocarbon materials are the first thing that comes to mind, and they also shine in research areas such as battery catalysis. For instance, because of its unique qualities, graphene, a member of the nanocarbon family, has garnered a lot of interest as a catalyst. In the next section, we will learn from nanocarbon materials' success in other fields and try to use them as an alternative to precious metals in our semiconductor microfabrication experiments.

2.4 PROPOSAL OF NON-METAL CATALYST ASSISTED CHEMICAL ETCHING

Although MaCE has been shown to be suitable for creating high aspect ratio micro- and nanostructures on semiconductor surfaces, there are still some issues that hinder their application, including metal residues, as mentioned in the previous section. Therefore, it is crucial to develop a new microfabrication technique for semiconductor surfaces that does not use noble metal catalysts. Nanocarbon materials are one of the most promising candidates. Next, we introduce the catalytic properties of nanocarbon, exemplified by graphene and its representative preparation methods, and propose a strategy to use nanocarbon as a catalyst in our semiconductor surface processing experiments.

A. Introduction

Graphene, as shown in Figure 2.11a, is a single-layer, honeycomb lattice structure composed of carbon atoms. Both graphene and its derivatives exhibit many intriguing properties, making them highly worthy of research. Their preparation methods will be discussed later.

Graphene oxide (GO) no longer has the perfect polycyclic macro-aromatic molecular structure of graphene but has a large number of oxygen-containing functional groups such as epoxy, hydroxyl, and carboxyl groups bonded to the planes and edges [26,27]. Compared with graphene, GO has a large number of lattice defects and is not ideal for use as electronic components or transistors, but it has many advantages as a catalyst material, which can be used directly or as a raw material to be further prepared as other types of graphene materials. For example, reduced graphene oxide (rGO) is produced by removing most of the functional groups by reducing GO. Reduced graphene has some sp^3 hybridized carbon atoms on the surface connecting H and residual

oxygen-containing functional groups.

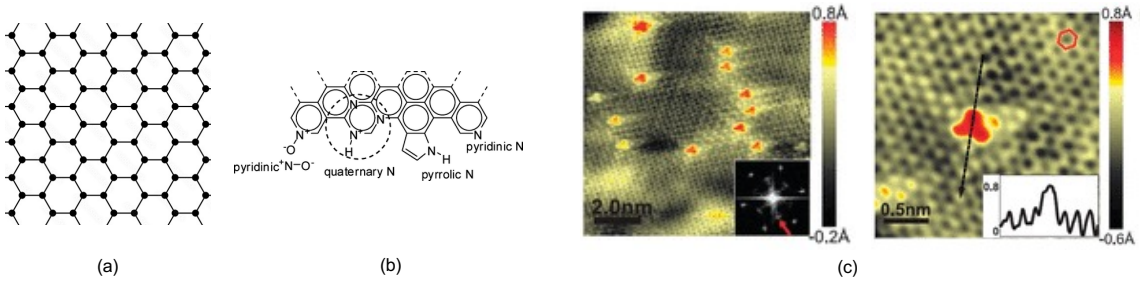

Figure 2.11 (a) Molecular structure of graphene. (b) Bonding configuration for nitrogen atoms in nitrogen-doped graphene [28]. (c) STM images of nitrogen-doped graphene showing nitrogen dopants [29].

Pure graphene contains only the C element; graphene oxide and reduced graphene contain oxygen-containing functional groups; in addition to C, its network also contains H and O elements. Functional modification of graphene materials can also introduce N, B, F, P, S, and other elements into their networks to produce heteroatom-doped graphene. In the periodic table, N and C have similar atomic radii, so N atoms can easily replace C atoms doped into the graphene structure. Through heteroatom doping, the original conjugated electronic network of graphene is changed, and new charge distribution and surface properties are formed in the doped region (as shown in Figure 2.11), which can affect specific reactions and catalytic processes.

B. Catalytic Properties of Carbon-based Materials

Carrier and Structural Modulation Functions

Prepared GO and rGO cannot fully reach single-layer thickness, so their specific surface area is far lower than the theoretical value but can still reach several hundred $m^2 \cdot g^{-1}$. It can be used to load and disperse catalytically active components, including noble metals, transition metals, polymetallic components, and metal oxides. Using active sites such as -H and -OH suspended on the surface of GO and rGO, organic functional groups with catalytic functions can also be introduced. As a carrier for catalysts, graphene-based materials can stabilize metal nanoparticles, prevent nanoparticles aggregation, and enhance the catalyst's anti-poisoning performance. Furthermore, graphene has an expansive surface structure that can facilitate certain reactions. It

allows for sufficient contact with chemicals and provides spatial convenience for material exchange. The synthesized catalysts are mainly used for hydrogenation reactions, oxidation reactions, and acid catalytic reactions.

Electronic Modulation Function

Although the preparation of graphene-based materials introduces many lattice defects, they still retain a planar structure and some physical properties. For example, its electrical conductivity is comparable to that of metallic materials. Therefore, graphene can work synergistically with loaded active components to accomplish many tasks. Kumar Surender et al. found that the strong electronic synergy between rGO and Co_3Fe can protect Co_3Fe from oxidation and corrosion. As a non-noble metal catalyst, Co_3Fe-rGO has strong tolerance to alkali solutions when used in oxygen reduction reactions (ORR) [30].

Enhanced Photocatalytic Function

The non-localized conjugated π-system of graphene can become an electron acceptor, and its excellent conductive properties are also conducive to electron migration [31]. Graphene materials can improve semiconductor photocatalytic performance by helping the migration of photogenerated electrons and preventing electron-hole recombination.

Hydrophilic-hydrophobic Tuning

The polar functional groups in GO have hydrophilic properties, making it easily dispersible in aqueous solvents. Defect sites and numerous oxygen-containing functional groups can induce the adsorption and deposition of nanoparticles on the GO surface, thereby affecting the catalyst's structure. Reduced GO can exhibit both hydrophilic and hydrophobic properties, depending on the amount of residual oxygen-containing functional groups. In some cases, the modified rGO is amphiphilic, that is, the graphene base is hydrophobic, and the organic functional groups are hydrophilic [32].

Catalytic Function

Without loading components such as metals or metal oxides and without grafting organic functional groups, the graphene material itself also has a catalytic function and is a carbon catalyst or metal-free catalyst.

GO is rich in various oxygen-containing functional groups, such as carboxyl groups, hydroxyl groups, and epoxy groups, and has a conjugated π electron structure. It can be used to catalyze hydration reactions, aldehyde acetal reactions, epoxide ring-opening reactions, etherification reactions, and acid-base catalyzed reactions. Lv et al. [33] found that GO will promote the oxidation reaction of 5-hydroxymethylfurfural. After the reaction, the carboxyl group of GO is reduced under anaerobic conditions, and GO acts as an oxidant to promote the reaction. During aerobic

oxidation, the oxygen components in reduced GO can still function. It is speculated that GO's high catalytic activity derives from unpaired electrons at the defective sites and adjacent carboxylic acid groups.

GO-based materials have been well known as nanocarbon catalysts in the reactions with alcohols, alkenes, and alkynes to prepare aldehydes or ketones [34]. GO was also used in the oxidation of sulfides to prepare sulfoxides. Other studies have shown that N-, B-, and both B- and N-doped graphene serve as carbon catalysts and have the ability to activate molecular oxygen [35].

C. Preparation of Nanocarbon Catalyst

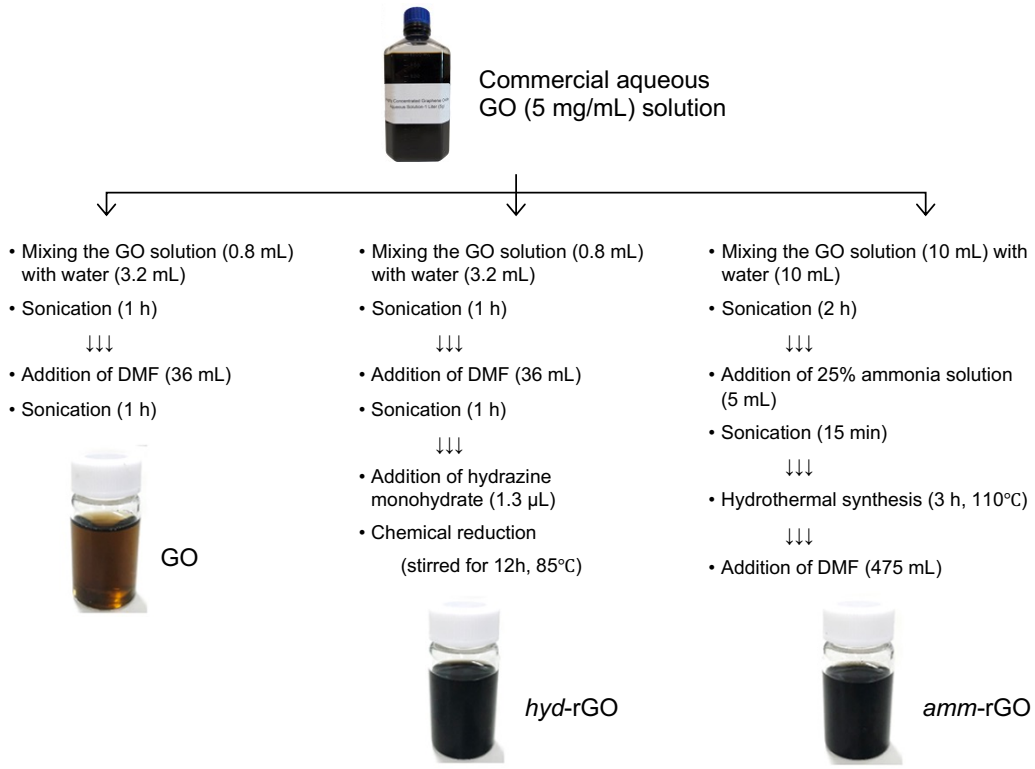

Figure 2.12 Details for obtaining GO, *hyd*-rGO, and *amm*-rGO. The concentration of GO or rGO in the colloidal suspensions was 0.1 mg/mL [37].

The mineral graphite, which is abundant in nature, consists of graphene sheets connected by van der Waals forces. Novoselov and Geim et al. obtained graphene by tape exfoliation in 2004,

followed by liquid phase exfoliation and electrochemical exfoliation. The size of graphene obtained by exfoliating graphite is very small, mostly in the micrometer to nanometer range. Other scholars have prepared larger graphene flakes by using a carbon source under specific conditions using the oriented-attachment growth or reconstruction method. None of the above graphene preparation methods can be produced on a large scale.

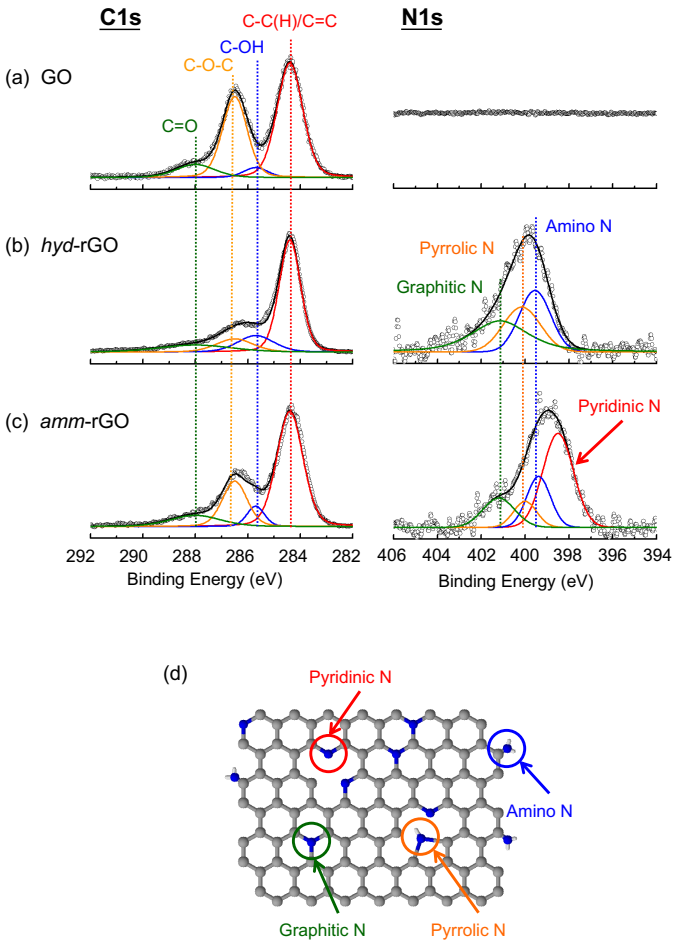

Figure 2.13 XPS spectra of (a) GO, (b) *hyd*-rGO, and (c) *amm*-rGO. (d) Nitrogen-doping sites in a graphene network. Gray, blue, and white balls present C, N, and H atoms, respectively [37].

Hummers et al. dissociated the graphite lamellar structure by oxidative intercalation, which is called the Hummers method. Later, Marcano [36] improved the Hummers method by using a strong oxidant to increase the spacing between graphite layers, and then exfoliating the graphene layers

under the effect of ultrasonication to form a monolayer or multilayered graphene oxide flake. Currently, the Hummers method is the primary method for large-scale graphene material preparation.

The reduction of GO is usually based on the GO solutions, and there are various methods for GO reduction, some of which are based on thermochemical methods, such as hydrazine hydrate, alcohols, hydrogen, and other reducing agents, and some of them are based on electrochemical methods. The manufacturing process from GO to rGO is highly operable, so rGO can be obtained at a relatively low cost.

Figure 2.12 illustrates the detailed methods for preparing different types of graphene solutions in our study. The raw material used is the GO solution provided by EM Japan. The graphene solution in the lower left corner is obtained by diluting the raw material with ultrapure water. The graphene solution in the center is obtained by reducing it with hydrazine monohydrate and is named *hyd*-rGO. Finally, the graphene solution on the right is obtained by the hydrothermal synthesis of ammonia-reduced GO (*amm*-rGO).

X-ray photoelectron spectroscopy (XPS) was applied to characterize the synthesized rGO nanosheets in Figure 2.13. The C 1s and N 1s XPS spectra of GO, *hyd*-rGO, and *amm*-rGO sheets are shown in the left and right columns in Figures 2.13(a–c), respectively. We can observe that both *hyd*-rGO and *amm*-rGO exhibit effective reduction in the C 1s spectra, as indicated by the weakening of the epoxide (C−O−C, 286.5 eV; orange) components in both samples compared to GO. The peak at 284.4 eV, corresponding to C−C(H)/C=C (red), remains the most prominent in each C 1s spectrum, suggesting that all samples maintain a graphene network. Other fitted peaks include C−OH at 285.7 eV (blue) and carbonyl C (C=O) at 288.0 eV (green).

Through N1s spectra, we learned that both *hyd*-rGO and *amm*-rGO are doped with nitrogen atoms. Namely, the fitted peaks at 398.4 eV (red), 399.5 eV (blue), 400.1 eV (orange), and 401.1 eV (green) represent pyridinic-, amino-, pyrrolic-, and graphitic-N atoms, respectively. Because of the intense peak of pyridinic-N atoms from the *amm*-rGO sample, a raw curve shown by open circles in the N 1s core level spectrum in Figure 2.13(c) shifted to a lower binding energy than that in Figure 2.13(b). These different peaks mentioned above indicate that nitrogen atoms were doped at different sites in the graphene network, as shown in Figure 2.13(d). In addition, we also noticed from the survey scans that *amm*-rGO is doped with more N atoms (the atomic concentration ratio of N to C) than *hyd*-rGO.

D. Nanocarbon-assisted Chemical Etching

After successfully synthesizing graphene-containing aqueous solutions, we attempted to apply them to the processing of Ge surfaces, i.e., nanocarbon (NC)-assisted chemical etching. For

convenience, we collectively refer to graphene oxide, hyd-rGO, and amm-rGO as nanocarbon.

So far, we have two paths to explore:

- i. Spin-coating a nanocarbon suspension to form a single flake level on Ge, which is then immersed in an etching solution for etching. This method has the advantage of being the easiest and most intuitive way to understand how the nanocarbon material behaves in a specific solution for etching Ge. However, it is not sufficient for practical production processing.
- ii. Combining wet etching in (i) with photolithography, i.e., forming a thin film (the thickness may be multilayered) of nanocarbon on the surface of Ge according to a pre-designed pattern. This method can selectively etch specific patterns, sizes (related to the exposure device), and arrangements on the Ge surface according to one's own wishes.

In addition to the research methods mentioned above, some of the latest research attempts and proposed schemes will be given in the discussion section of Chapter 5.

Etching Using Single Level Flakes of Nanocarbon

This experiment is prepared just like MaCE described in Figure 2.7a, with the exception that the metal catalyst in Figure 2.7a is replaced by single-layer flakes of nanocarbon. Of course, different materials use different deposition methods. The graphene catalyst used in our system is both a nanomaterial and a soft material (colloid), suspended in a solvent in liquid form. It is particularly suitable for being loaded on a substrate by spin coating.

As shown in Figure 2.14a, the Ge substrate with deposited nanocarbons will be used for etching experiments and surface observation. Before etching, the monolayer nanocarbon flakes are dispersed on the Ge surface after spin coating, as shown in Figure 2.14b. The size of a single nanocarbon flake is at the micron level, and the thickness is about 1.0 nm, which is thicker than the 0.335 nm of ideal graphene. Although not shown here, longer ultrasonic treatment of the nanocarbon solution before etching can obtain smaller-sized nanocarbon flakes.

Figure 2.14b displays the results of etching Ge in O_2-containing water using three types of nanocarbon catalysts. For specific experimental conditions, see Reference 37. It is obvious that etched hollows with a shape similar to nanocarbon flakes are formed on the Ge surfaces. These indicate that the loaded nanocarbon flakes play the role of a catalyst (just like noble metals in MaCE), removing material from the areas they cover. Figure 2.14c shows that the depths of the etched hollows using GO, *hyd*-rGO, and *amm*-rGO are approximately 9.1, 15.5, and 19.3 nm, respectively. Figure 2.14 shows that the etching effects vary for different types of nanocarbon flakes, which is highly related to the elemental composition and chemical structure of nanocarbon flakes. As illustrated in Figure 2.13, although all three types of nanocarbon retain graphene's carbon network, their content and distribution of oxygen-containing functional groups and doped

atoms differ.

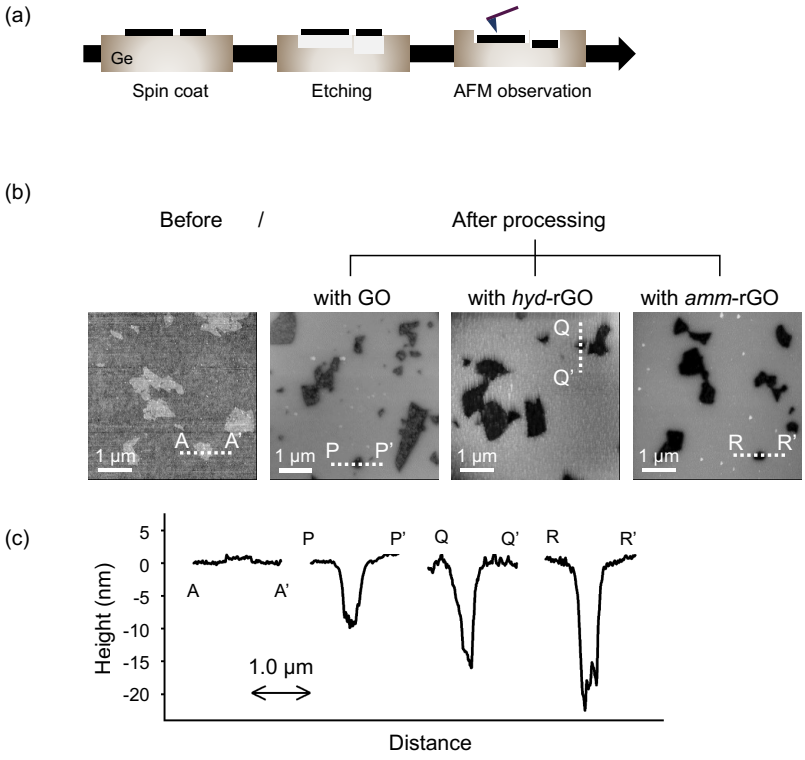

Figure 2.14 (a) Process-flow diagram for the etching experiment with dispersed graphene sheets on a Ge substrate. (b) Atomic force microscopy images of the Ge surface in etching experiments. The substrates were immersed in O2-containing water at 29°C for 3h. (c) Cross-sectional profiles along A-A', P-P', Q-Q', and R-R' [37].

In this study, one of our objectives is to prepare graphene with high catalytic performance, aiming to develop semiconductor surface microfabrication techniques using nanocarbons as catalysts. To do this, we need to relate the catalytic potential to the atomic structure for analysis. In other words, we need to determine what kind of atomic structure can lead to high catalytic activity at the atomic level. Catalytic activity is defined as the ability to promote a series of chemical reactions during the etching process.

Selective Area Etching Using Nanocarbon Films

In order to meet the demands of production, we seek to process three-dimensional microstructures on semiconductor surfaces according to predefined patterns. This requires the ability to form

arbitrarily designable nanocarbon patterns on the semiconductor surface, which is clearly not satisfied by spin-coating methods. We applied photolithography to our wet processing (Figure 2.15). As a result, we were able to form the desired nanocarbon pattern on Ge samples in accordance with the computer-aided design on the mask.

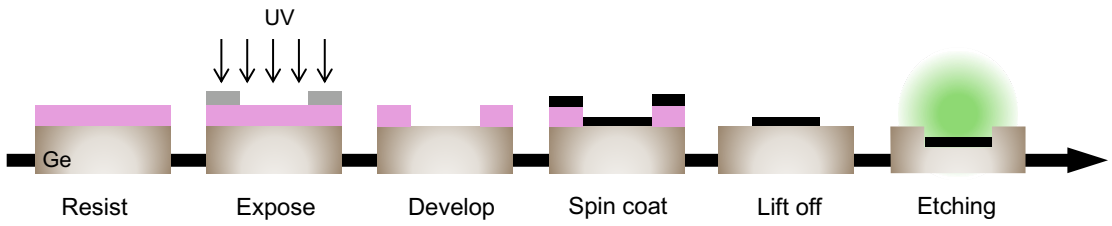

Figure 2.15 Process-flow diagram for the etching experiment combined with photolithography.

An experiment using the flow in Fig. 2.15 is shown in Fig. 2.16. This design's mask pattern is the Osaka University logo on a millimeter scale. Figure 2.16a shows that after lifting off the resist, the Ge substrate is left with a pattern formed by nanocarbon flakes. The cross-section profile reveals that the nanocarbon film's thickness is only 1-3 nm, as indicated by gray arrows. After etching such a sample in O_2-containing water, a trench structure was clearly visualized in Figure 2.16b. The cross-sectional profile shows an etching depth of about 100 nm and an etching rate of more than 30 nm/h.

However, there is still much work to be done. First, the etching shown in Figure 2.16 is only at the millimeter level, while our goal is at the micron or even submicron level.

Regarding this, the current experimental equipment supports reducing the linewidth of a mask pattern to a few microns, and it can even further reduce the pattern by 5 times using imaging lenses. However, at such small dimensions, forming continuous and complete nanocarbon films like that shown in Figure 2.16a may face challenges. On the other hand, even if we successfully deposit the desired film patterns on the Ge surface, there are still many aspects of the subsequent etching process that need to be verified, including:

- Whether ideal trench patterns (with vertical and smooth sidewalls, as well as flat bottoms) can be formed
- The processing consistency between different patterns or even different samples
- High etching rates
- The continuity of the etching process (the catalytic effect of nanocarbon), and so on

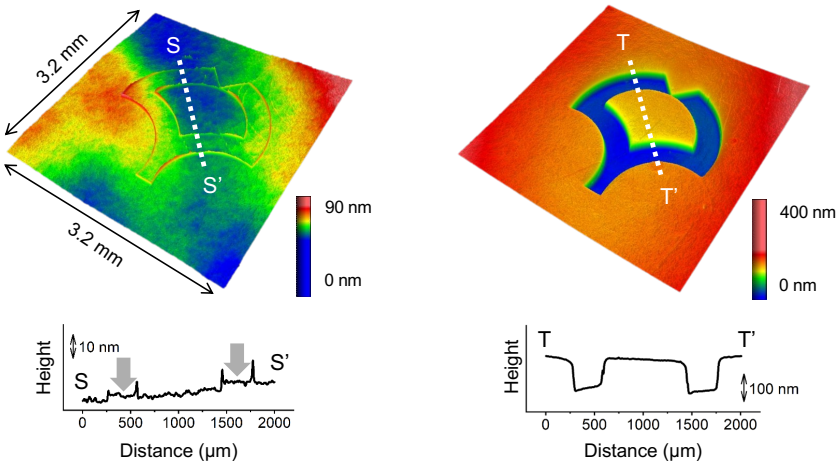

Figure 2.16 Surface topographic images taken by using a phase-shifting interferometer. (a) and (b) show Ge surfaces with a patterned GO film, or the logo of Osaka University, before and after the immersion into O_2-containing water for 3h at 58℃, respectively. Cross-sectional profiles along S-S' and T-T' are provided in (a) and (b). The gray arrows in the profile in (a) indicate the position of the GO film [37].

2.5 STRATEGY OF THIS THESIS

Figure 2.17 displays the plan used in this thesis to create a semiconductor surface microfabrication method based on non-metal-assisted chemical etching. It includes scanning tunneling microscopy (STM) to look at nanocarbon materials' surfaces, first-principles calculations, and nanocarbon-assisted chemical etching from the previous section. Although the catalytic process in etching is quite complex, it is widely recognized to initiate from active sites on the catalyst surface. These active sites include topological defects, lattice defects, functional groups, etc., which provide adsorption, dissociation, and reaction sites for reactant molecules while lowering the reaction's activation energy. Therefore, it is believed that an understanding of the atomic structure of nanocarbon catalysts, such as local defects, can help their applications.

- Scanning tunneling microscopy study

The nanocarbon catalyst used in this study has catalytically active local structures according to the synthesis method (solution reduction method, hydrothermal synthesis method), such as oxygen-containing functional groups, doped nitrogen atoms, vacancies, etc. In addition, the edge of nanocarbon alters the symmetry of the atomic arrangement and is regarded as a linear defect. Nanocarbon materials with the above localized structures are considered to be more chemically active than perfect graphene [38,39], which is the key to their function as catalysts. STM allows the observation of high-energy electrons near the Fermi level of nanocarbon materials, which are indispensable for steps such as molecular adsorption. Experiments proved that defect structures in the nanocarbon materials change the way electrons are distributed on the surface. This will be talked about in Chapter 3.

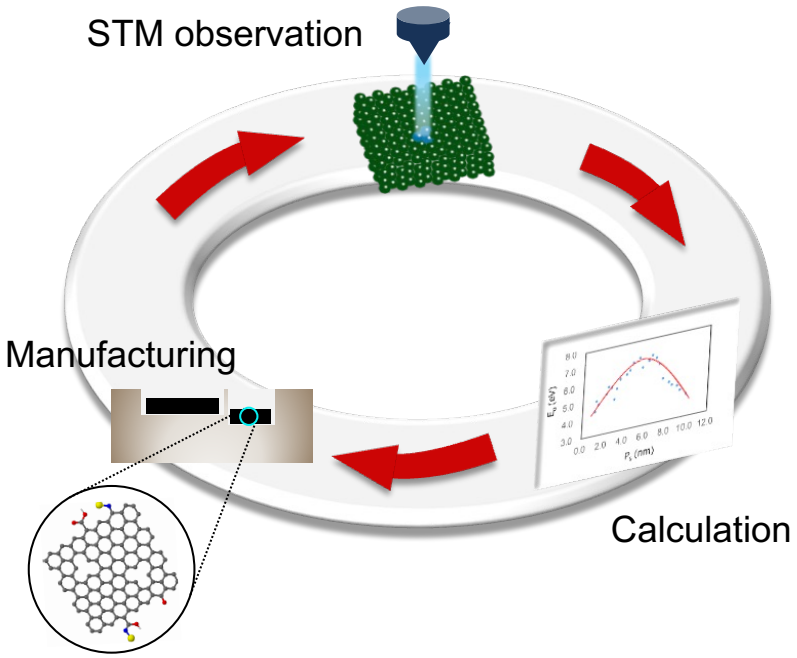

Figure 2.17 Strategy of this research including: STM observation, calculation, and manufacturing.

For structures such as oxygen-containing functional groups and doped nitrogen atoms, it is impractical to analyze the atomic structure by STM. This is because these structures are extremely complex and have yet to be fully understood. STM can give an electron density map of small regions, but it cannot determine the elemental composition or give information about the atomic structure. So far, in STM-related studies of graphene, the absence of individual carbon atoms, as

well as linear defects at the edges, have been studied the most. These defects frequently lead to a superstructure in close proximity that cannot be visualized in ideal graphene.

- First-principles calculations

Due to the limitations of experimental observations by scanning tunneling microscopy, computer-based simulations can provide a good complement. It can easily construct models as one's willing, such as single-atom vacancies and linear defects, with great efficiency. With the development of computing power and computational theory, accuracy has also improved. But combining the simulated results with our experimental data and verifying the soundness of the calculations requires extra attention.

- Nanocarbon-assisted chemical etching

This part starts with the synthesis of a nanocarbon aqueous solution, the implementation of the etching process, and the observation of the final processing results. The catalyst is synthesized in accordance with the established process. The processing results are mainly analyzed using atomic force microscopy and a white light interferometer, and sometimes other characterization methods such as scanning electron microscopy are also used.

Many descriptions were made in the previous section for the challenges encountered in the etching process. In addition, during the etching process, the reaction mechanism of the catalyst and semiconductor interface in the etching solution is also worthy of study.

2.6 SUMMARY

To realize microfabrication of semiconductor surfaces without using noble metals, a review of commonly used microfabrication techniques for semiconductor surfaces is presented. The advantages and disadvantages of dry etching and wet etching are summarized, and the application of metal-assisted chemical etching is introduced. Nanocarbon catalysts are proposed to solve problems such as residual noble metals on the surface after processing, which is a new attempt at catalyst-assisted chemical etching. The feasibility of applying nanocarbon materials to semiconductor surface etching is also verified. The contents of this chapter are summarized as follows:

Traditional dry etching and wet etching, although both have a long history of application, have their own obvious shortcomings. Overall, these techniques are unable to achieve anisotropic processing of semiconductor surfaces while obtaining a surface without introducing damage.

These issues require the development of a new microfabrication method.

The emergence of metal-assisted chemical etching has triggered much research. However, there are residual metal particles on the surface and inside of the processed semiconductor, which affects the performance of the device and the application of this technology.

We propose the use of nanocarbon materials to etch semiconductor surfaces in solution. This method utilizes the catalytic activity of nanocarbon materials to accelerate the oxidation and removal (etching) of semiconductor surfaces in contact with them. Some research challenges are listed as topics for this study, and research strategies to accomplish these goals are also presented.

REFERENCES

1) L. Lin, R. T. Howe, A. P. Pisano, Journal of Microelectromechanical Systems 7 (1998) 286.
2) http://www.meas-spec.com/myMeas/sensors.
3) C. Y. Chang, S. M. Sze, Eds., ULSI Technology, New York: McGraw-Hill (1996).
4) S. M. Sze, Semiconductor Devices: Physics and Technology, 2nd ed., New York: Wiley (2002).
5) B. Schwartz, H. Robbins, Journal of The Electrochemical Society 123(3) (1976) 1903.
6) W. Kern, RCA Rev. 39 (1978) 278-308.
7) D. B. Lee, J. Appl. Phys. 40 (1969) 4569-4574.
8) J. B. Price, Anisotropic Etching of Silicon with KOH-H_2O-Isopropyl Alcohol, Semiconductor Silicon 1973, Chicago (1973).
9) H. Seidel, L. Csepregi, A. Heuberger, H. Baumgärtel, Journal of The Electrochemical Society 137(17) (1990) 3612.
10) D. H. Lee, S. J. Choo, U. Jung, K. W. Lee, K. W. Kim, J. H. Park, J. Micromech. Miroeng. 25 (2015) 015003.
11) H. -C. Liu, Y.-H. Lin, W. Hsu, Microsystem Technologies 10 (2003) 29-34.
12) J. Albero, L. Nieradko, C. Gorecki, H. Ottevaere, V. Gomez, H. Thiepont, J. Pietarinen, B. Päivänranta, N. Passilly, Optics Express 17 (2009) 6283.
13) M. Bauhuber, A. Mikrievskij, A. Lechner, Mater. Sci. Semicond. Process. 16 (2013) 1428.
14) X. Li, P. W. Bohn, Appl. Phys. Lett. 77 (2000) 2572-2574.
15) Z. Huang, N. Geyer, P. Werner, J. de Boor, U. Gösele, Adv. Mater. 23 (2011) 285.
16) X. Li, Current Opinion in Solid State and Materials Science 16 (2012) 71-81.
17) H. Fang, Y. Wu, J. Zhao, J. Zhu, Nanotechnology 17 (2006) 3768-3774.
18) R. Ghosh, P. K. Giri, Nanotechnology 28 (2017) 012001.

19) A. Vlad, A. L. M. Reddy, A. Ajayan, N. Singh, J.-F. Gohy, S. Melinte, P. M. Ajayan, PNAS 109(38) (2012) 15168-15173.
20) J. Kim, H.-R. Kim, H.-C. Lee, K.-H. Kim, M.-S. Hwang, J. M. Lee, K.-Y. Jeong, H.-G. Park, Nano Lett. 19 (2019) 1269-1274.
21) D. Liu, L. Lin, Q. Chen, H. Zhou, J. Wu, ACS Sens. 2 (2017) 1491-1497.
22) T. Kawase, A. Mura, K. Dei, K. Nishitani, K. Kawai, J. Uchikoshi, M. Morita, K. Arima, J. Appl. Phys. 111 (2012) 126102.
23) T. Kawase, A. Mura, K. Dei, K. Nishitani, K. Kawai, J. Uchikoshi, M. Morita, K. Arima, Nanoscale Res. Lett. 8 (2013) 151.
24) T. Kawase, Y. Saito, A. Mura, T. Okamoto, K. Kawai, Y. Sano, M. Morita, K. Yamauchi, K. Arima, ChemElectroChem. 2 (2015) 1656-1659.
25) A. Kurek, S. T. Barry, Sci. Technol. Adv. Mater. 12 (2011) 045001.
26) D. R. Dreyer, H.-P. Jia, A. D. Todd, J. Geng, C. W. Bielawski, Org. Biomol. Chem. 9 (2011) 7292.
27) D. Chen, H. Feng, J. Li, Chem. Rev. 112 (2012) 6027-6053.
28) E. J. Biddinger, D. von Deak, U. S. Ozkan, Top Catal 52 (2009) 1566-1574.
29) L. Zhao, R. He, K. T. Rim, T. Schiros, K. S. Kim, H. Zhou, C. Gutiérrez, S. P. Chockalingam, C. J. Arguello, L. Pálová, D. Nordlund, M. S. Hybertsen, D. R. Reichman, T. F. Heinz, P. Kim, A. Pinczuk, G. W. Flynn, A. N. Pasupathy, Science 333 (2011) 999.
30) S. Kumar, D. Kumar, B. Kishore, S. Ranganatha, N. Munichandraiah, N. S. Venkataramanan, Applied Surface Science 418 (2017) 79-86.
31) B. Gomez-Ruiz, P. Ribao, N. Diban, M. J. Rivero, I. Ortiz, A. Urtiaga, Journal of Hazardous Materials 344 (2018) 950-957.
32) J. Kim, L. J. Cote, F. Kim, W. Yuan, K. R. Shull, J. Huang, J. Am. Chem. Soc. 132 (2010) 8180-8186.
33) G. Lv, H. Wang, Y. Yang, T. Deng, C. Chen, Y. Zhu, X. Hou, ACS Catal. 5 (2015) 5636.
34) A. Dhakshinamoorthy, A. Primo, P. Concepcion, M. Alvaro, H. Garcia, Chem. Eur. J. 19 (2013) 7547-7554.
35) D. R. Dreyer, H.-P. Jia, C. W. Bielawski, Angew. Chem. Int. Ed. 49 (2010) 6813-6816.
36) D. C. Marcano, D. V. Kosynkin, J. M. Berlin, A. Sinitskii, Z. Sun, A. Slesarev, L. B. Alemany, W. Lu, J. M. Tour, ACS Nano 4 (2010) 4806-4814.
37) R. Mikurino, A. Ogasawara, T. Hirano, Y. Nakata, H. Yamashita, S. Li, K. Kawai, K. Yamamura, K. Arima, J. Phys. Chem. C 124 (2020) 6121-6129.
38) N. Dimakis, I. Salas, L. Gonzalez, O. Vadodaria, K. Ruiz, M. I. Bhatti, Molecules 24 (2019) 754.
39) C. U. Mendoza-Domínguez, V. A. Basiuk, Mater. Chem. Phys. 271 (2021) 124963.

CHAPTER

3

ELECTRONIC STRUCTURE OF FINITE-SIZE GRAPHENE-BASED MATERIALS

This chapter, as part of the fundamental research on graphene-based catalysts, begins with an introduction to the atomic structures of graphite, graphene, and graphene nanoribbons in Sec. 3.1. Sec. 3.2 introduces the past studies on graphene's electronic properties and the research methodology. Sec. 3.3 focuses on the characterization method used in this study, namely scanning tunneling microscopy (STM). Sec. 3.4 presents detailed experimental results from the nanoscale characterization of graphene. Sec. 3.5 outlines our plan for simulating the electronic states of graphene.

3.1 INTRODUCTION TO GRAPHENE NANOSTRUCTURES

Carbon nanomaterials encompass various forms across different dimensions, ranging from 0 to 3. Among them, the representative ones are three-dimensional (3D) graphite, two-dimensional (2D) monolayer graphene, and one-dimensional (1D) graphene nanoribbons. This section primarily focuses on monolayer graphene, which serves as the foundation stone. For example, graphite is a stacked form of graphene, whereas graphene nanoribbons can be considered the result of cropping 2D graphene. The aqueous/organic solution of the nanocarbon catalyst used in this study contains graphene-based flakes, which retain graphene's fundamental carbon framework. We must understand the basic atomic structure of graphene, even though our goal is to investigate chemical doping and structural defects in graphene-based materials like graphene oxide or reduced graphene oxide.

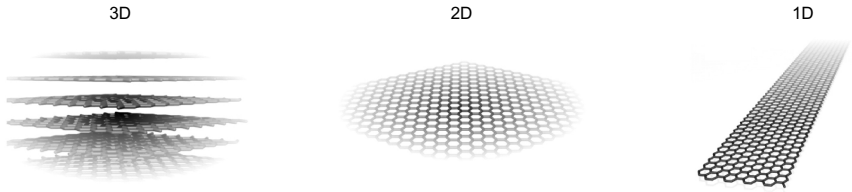

Figure 3.1 Atomistic models of carbon nanostructures exhibit different dimensionalities: 3D (graphite crystal), 2D (graphene), and 1D (graphene nanoribbon) [1,2].

Carbon possesses six electrons, with two core electrons (1*s*) and four valence electrons (2*s* and

2*p*). In Figure 3.2a, there are two unpaired valence electrons (2*p*), and this configuration is referred to as the ground state. However, configurations like those in Figure 3.2b and Figure 3.2c are more common. One of the paired 2*s* electrons will occupy an empty 2*p* orbital. One 2*s* electron and two 2*p* electrons will form new hybrid orbitals. There are four unpaired electrons in the excited state, and they are able to form at most four bonds.

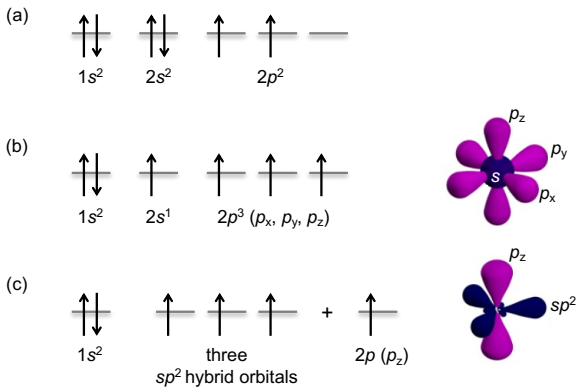

Figure 3.2 Electronic configurations of carbon: (a) ground state, (b) excited state, and (c) sp^2 hybridization.

The graphene-based materials in Figure 3.1 all fall into sp^2 hybridization. Regarding sp^2 hybridization, we have provided an explanation in the previous paragraph and in Figure 3.2c. Each carbon atom in graphene is bound to its three nearest neighbors through sp^2 hybridization to form three equivalent σ bonds in the plane with a bond length of about 0.142 nm, forming an infinitely regular orthohexagonal honeycomb lattice . The σ bonds are strongly covalent bonds that form the planar structure of graphene sheets (Figure 3.3), as well as their mechanical and thermal properties. The remaining $2p_z$ orbital is orthogonal to the graphene plane, which forms localized π (bonding) and π^* (antibonding) orbitals by a lateral interaction with neighboring p_z orbitals (called the *pp*π interaction). These dispersed π electrons are distributed near the Fermi energy and determine graphene's transport properties.

As shown in Figure 3.4, graphene is like many single layers of graphene stacked together, with only van der Waals forces holding the layers together. Therefore, it is relatively easy to break them apart using some mechanical methods. For example, it is relatively easy to produce single or multiple layers of graphene using the scotch tape method. The graphene in different layers is most likely arranged in an AB stacking. Simply put, this means that the carbon atoms in the upper layer of graphene are offset compared to those in the lower layer. The definitions of A and B atoms will

be explained in later experimental observations. The interlayer distance in graphene ($z_G/2$) is very small, about 0.335 nm [3].

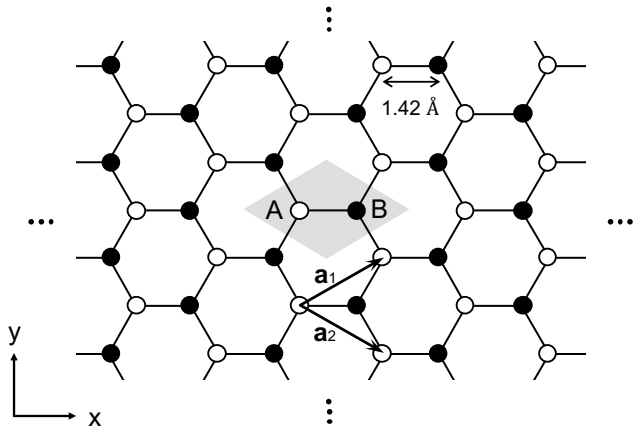

Figure 3.3 The graphene structure has a hexagonal lattice. Solid and empty circles indicate the two triangular sublattices, labeled A and B. The gray area subtended by primitive translation vectors $\mathbf{a}_1$ and $\mathbf{a}_2$ marks the primitive unit cell.

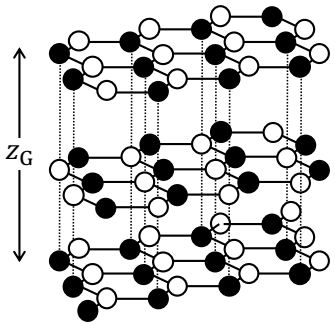

Figure 3.4 The most common graphite structure is called AB (Bernal) stacking.

Just as bulk materials exhibit certain surface states, graphene nanostructures with finite dimensions also possess unique edge states, such as graphene nanoribbons (GNRs) with widths on the nanoscale. Unlike the zero bandgap of graphene crystal structures, the electronic states in GNRs are influenced by quantum confinement and depend on the atomic structure of the ribbons. Figure 3.5a shows two typical shapes: the zigzag edge and the armchair edge, indicated by arrows, with a 30° angle difference. Following previous conventions, we denote these GNRs with zigzag and armchair edges as N-ZGNR (Figure 3.5b) and N-AGNR (Figure 3.5c), respectively, where N

was labeled. In the 1990s, Fujita [4] and Nakada [5] et al., using tight-binding models, discovered that GNRs with zigzag edges exhibit metallic properties, with electronic states near the Fermi level concentrated at the edges. On the other hand, AGNRs can exhibit either metallic or semiconducting properties based on the number N.

Other than these two “ideal” cases, more complex and experimentally common shapes are a combination of zigzag- and armchair-shaped pieces. Experimental observations indicate that GNRs currently have a high degree of edge roughness, and finite-sized graphene nanosheets usually exhibit disordered edge structures. The study of such graphene nanosheets will be discussed in the subsequent sections of this chapter.

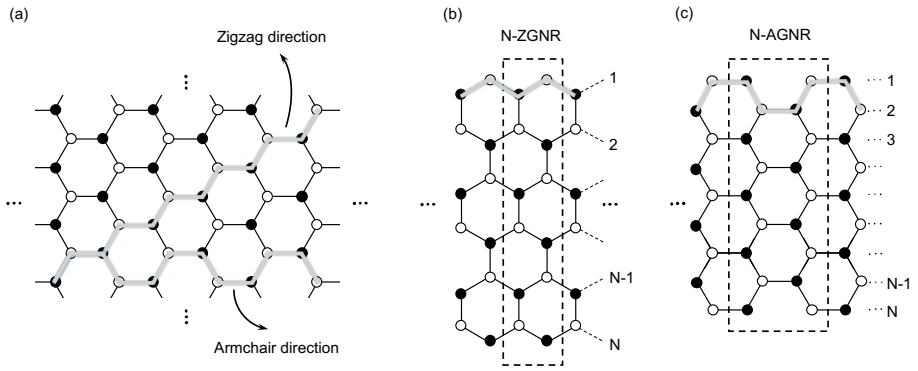

Figure 3.5 (a) Honeycomb lattice of graphene showing both zigzag and armchair directions. Ribbons with zigzag and armchair edges are shown in (b) and (c), respectively, where the shape of the edges at the top of each scheme is highlighted with a gray shadow. Their corresponding 1D unit cells are marked with dashed boxes. Note that the dangling bonds on the edge sites of GNRs are terminated by hydrogen atoms, which were not shown.

3.2 RESEARCH ON GRAPHENE-BASED MATERIALS

Graphene, with its atomically thick, two-dimensional structure and many outstanding properties, has attracted significant attention from researchers in recent years [6-8]. To date, scientists have tried various methods to obtain graphene in order to explore its various aspects. The structure and properties of graphene obtained through different methods exhibit more or less differences, often leading to applications in different fields. Furthermore, some researchers have modified or decorated the structure of graphene to add new functions [9] and application scenarios. The research

on graphene is diverse, and we will introduce its preparation methods, microstructure, and corresponding applications.

A. Introduction

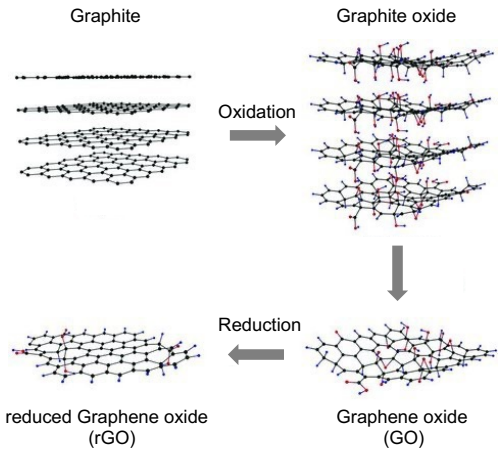

Figure 3.6 Preparation of graphene oxide and chemically reduced graphene [10].

Graphene-based materials are mostly prepared by aqueous-phase methods. The first step is to prepare graphite oxide, as shown in Figure 3.6. It can be seen that the interlayer distance of graphite increases during oxidation. This is due to the presence of many oxygen-containing groups on the surface of graphene, which lays the foundation for the subsequent chemical exfoliation of single-layer or few-layer graphene. Ultrasonic treatment can be used to separate GO sheets in solution, forming a stable colloidal dispersion. For the entire oxidation process, please refer to the previously introduced Hummers' method [11]. Chemically reducing the obtained GO solution results in reduced GO (rGO). The usual method is to add a reducing agent [12] to the GO solution to remove most of the oxygen-containing functional groups formed during oxidation. At this point, we obtain a single-layer graphene-based material that retains most of its aromatic structure.

To better apply the prepared GO or rGO, it is necessary to investigate them. Studies have shown that GO and rGO have significant differences from graphene. For example, even the conductivity of rGO, which is closer to graphene, is significantly reduced [9,13]. In this case, graphene-based materials obtained through the process shown in Figure 3.6 may not be suitable for applications

in the field of electronic devices. To clarify this, numerous studies have explored the detailed atomic structure of graphene-based materials obtained through similar methods.

Figures 3.7(a)–(c) exhibit Transmission Electron Microscopy (TEM) images of single-layer graphene, GO, and rGO sheets on a substrate, respectively. Unlike graphene, GO and rGO are structurally inhomogeneous, with several features indicated by different colors. These holes are thought to be caused by gases released during chemical synthesis. The graphitic regions indicate that the basal plane is incompletely oxidized, retaining the hexagon structure and 1.4 Å lattice constant. The graphitic area in rGO sheets significantly increases from approximately 16% in GO to around 70%, indicating a substantial restoration of the original sp^2 bonding character. The disordered regions on the surface of GO represent high oxidation and occupy a large proportion of the surface area. These disordered regions are not completely eliminated after reduction, and methods such as annealing may further reduce the oxygen content. In summary, both GO and rGO have many differences compared to graphene, which undoubtedly brings many challenges and opportunities to their applications.

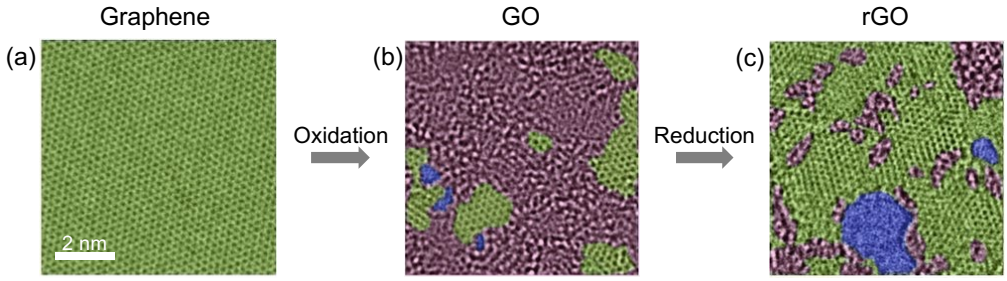

Figure 3.7 TEM images showing the atomic structures of single suspended sheets of (a) graphene, (b) GO, and (c) rGO. The green, purple, and blue areas depict ordered graphitic sp^2 domains, disordered regions with remaining oxygen functionalities, and holes, respectively [14].

B. Applications of Graphene Defects

In addition to the holes and oxygen-containing functional groups shown in Figure 3.7, GO and rGO also contain edge defects, structural distortions, and strains in the carbon network, as well as some doped atoms [15]. The effects of these defects on graphene-based materials are listed in Figure 3.8. Currently, there are two main research directions: one is to minimize the defect content in the carbon lattice to obtain the excellent physical properties of nearly perfect graphene; the other is to actively utilize these defective structures. Methods to eliminate defects include optimizing the oxidation and reduction processes of graphene materials, high-temperature annealing, or using

chemical vapor deposition to produce high-quality graphene. On the other hand, these defects open up new applications for graphene-based materials, such as in catalysis. Researchers have been actively working on exploiting the defect structures in the graphene network and have made significant efforts in this regard. New synthesis and processing methods, new materials, and new catalytic application scenarios are continually being proposed. However, all these advancements are based on a clear understanding of the various defects, including their atomic structure, structure-activity relationship, and catalytic mechanism.

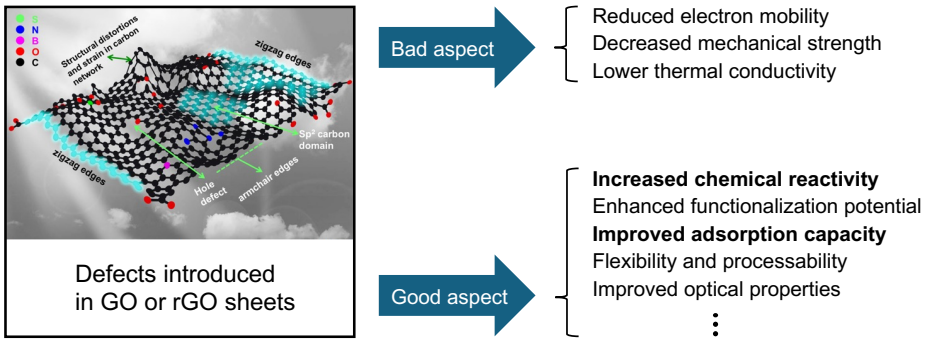

Figure 3.8 Defect structures [15] in graphene-based materials offer both benefits and drawbacks.

As reviewed in Figure 3.9, carbon-based nanomaterials have various defects, including vacancy defects, edge defects, topological defects, and heteroatoms. These defects are ubiquitous in graphene-based materials and can arise from various causes, but our understanding of them is still quite limited. It is currently known that defects often lead to uneven electron distribution and distortion of the electronic structure. Moreover, the originally chemically inert graphene exhibits a certain degree of chemical activity due to the presence of defect structures. This has led to extensive research on carbon nanomaterials in the field of catalysis.

For instance, high electron density distribution and special electronic structures have been observed near edge defects. Analysis suggests this may be related to the numerous unpaired π-electrons at the edges. Such structures can facilitate electron transfer and serve as active sites for reactions. Topological defects disrupt the symmetry of the aromatic hexagonal structure. These local defects can also lead to charge redistribution, aiding certain chemical reactions in conjunction with adjacent carbon atoms. The aforementioned types of defects are extensively studied in electrode materials for energy devices, primarily due to their electrocatalytic properties. Additionally, doping with heteroatoms (such as N, B, P, etc.) has been clearly shown to enhance the chemical activity of graphene. Depending on the type and amount of dopant atoms, graphene-

based materials can exhibit different properties.

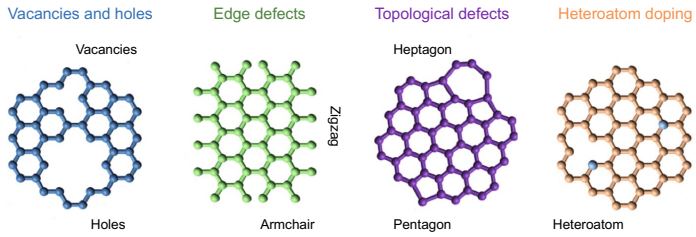

Figure 3.9 Schematic illustrations of the type of defective graphene-based nanomaterials [16].

There has been extensive research on the catalytic mechanisms of defective structures in graphene. First-principles calculations reveal that graphene oxide with oxygen-containing groups, as shown in Figure 3a, demonstrates high catalytic activity in the oxidative dehydrogenation of propane to propylene. Hydroxyl groups situated around the active sites provided by epoxides significantly improve the activation of propane's C-H bonds. This enhanced catalytic activity is notably dependent on the specific sites involved. Calculations of bonding energy, adsorption energy, activation energy, and reaction pathway provide a molecular-level understanding of the process. For more details, please refer to reference [17]. Additionally, some studies have constructed high-performance graphene catalysts through structural modifications. For example, Figure 3b demonstrates an experimental approach to further modify graphene oxide, resulting in primary and tertiary amine bifunctional graphene oxide [18].

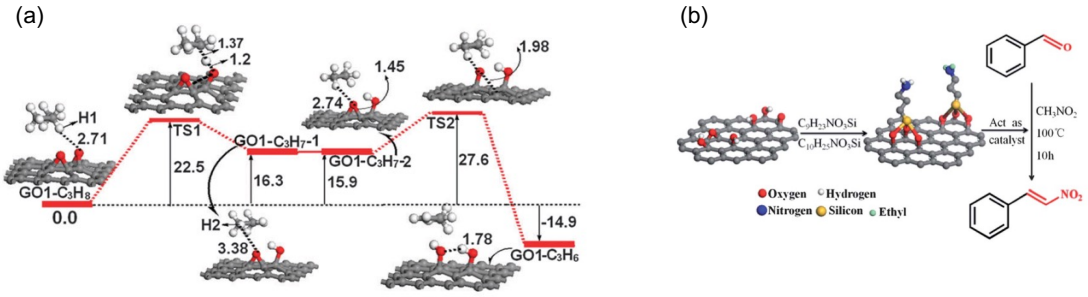

Figure 3.10 (a) Effect of GO surface hydroxyl groups on catalytic reaction activity [17]. (b) Catalytic reduction of nitrobenzene by rGO [18].

As we introduced in Figure 3.7, there are many unidentified disordered regions in the carbon framework of chemically synthesized rGO. Although attempts have been made to observe and understand them, some theoretical atomic models of materials like GO have been proposed. However, detailed records in this area are still scarce. To enrich and enhance the fundamental research and applied science of graphene, it is essential to gain a deep understanding of its atomic structure and corresponding properties. Figure 3.11 shows scanning tunneling microscope (STM) observations of these graphene derivatives, providing nanoscale local structural images.

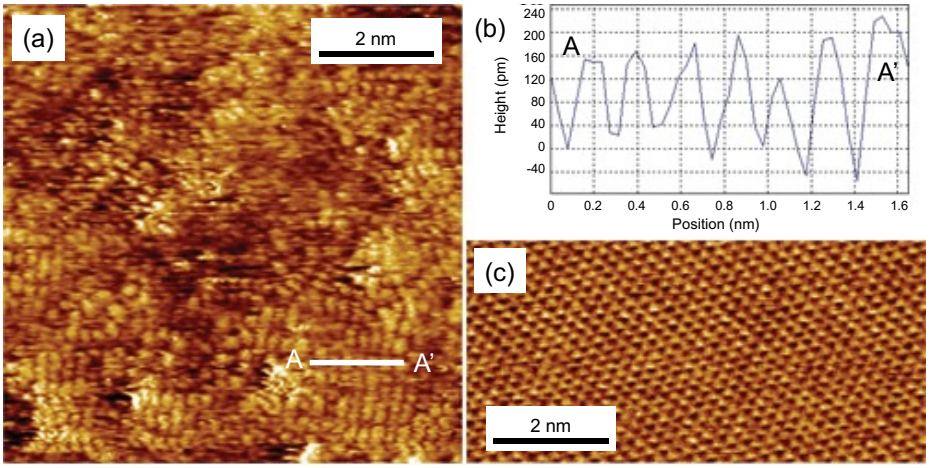

Figure 3.11 (a) Typical atomic-scale STM images of the basal plane of chemically reduced graphene oxide nanosheets. (b) Line profile taken along the line A-A' in (a). (c) An atomic-scale STM image of pristine, defect-free graphite is shown for comparison. Tunneling parameters: I = 3 nA, V = 10 mV for (a), and I = 2 nA, V = 100 mV for (c) [19].

Clearly, the images indicate that the distribution of disordered structures within rGO may be random. From the profile in Figure 3.11b, it can be seen that the lattice constants are not significantly different from the data observed in graphene. In contrast, the STM images of highly oriented pyrolytic graphite show a highly ordered atomic arrangement, as shown in Figure 3.11c. The formation of disordered regions is believed to be related to some functional groups distributed on the graphene plane. Additionally, many defect structures within rGO can also be reflected in the images. For instance, besides the defects listed in Figure 3.9, graphene also exhibits distortions or wrinkles in the three-dimensional plane.

C. Research Objectives for Characterization of Graphene-based Materials

Despite many efforts to understand the local atomic-level structure of chemically reduced graphene, satisfactory results have yet to be achieved. This remains a primary goal in characterizing graphene-based nanomaterials in our study. Figure 3.12 presents a hypothetical illustration of the local structure of an rGO sheet. In addition to the vacancy defects and oxygen-containing functionalities shown in Figure 3.11, Figure 3.12 also depicts nitrogen atom doping and edge defects. Doping graphene sheets with atoms of other elements has been shown to enhance their catalytic performance. Edge structures in pristine nanographene, particularly in the form of nanoribbons, are known to significantly alter their electronic properties. Similarly, we believe that edges in rGO sheets will also play an important role. Furthermore, the edges of graphene sheets produced by chemical reduction are believed to be randomly decorated with carboxyl groups. Note that Figure 3.12 does not depict the distortion of the carbon skeleton.

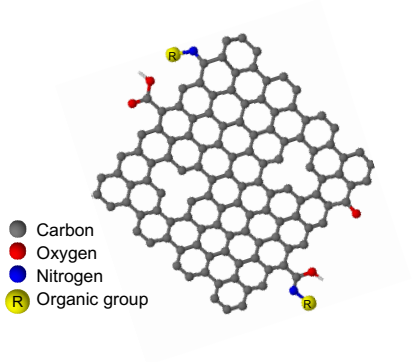

Figure 3.12 (a) A schematic illustration of the chemically reduced graphene oxide nanosheets used as a nanocarbon catalyst in our study.

Here, we summarize the local defective structures we need to elucidate (in order of difficulty):

- Vacancy defects (single atom and multi-atom)
- Edge structures
- Doped atoms, oxygen-containing functional groups, and spatial distortions

In addition to understanding these detailed local structures, we need to correlate each structure with its catalytic activity to better develop its catalytic performance and apply it in actual production and processing.

3.3 SCANNING TUNNELING MICROSCOPY

For atomic-scale nanomaterials like graphene, characterization and analysis are inevitably involved in research. Appropriate testing methods can provide information about the size, morphology, and atomic structure of graphene materials. These characteristics are crucial for analyzing the properties of graphene and guiding graphene research. Various characterization methods can provide strong support for graphene research. Due to the unique low-dimensional properties of graphene, studying its microstructure necessitates the use of analytical techniques capable of observing at the nanoscale, such as various electron microscopy and scanning probe microscopy techniques.

A. STM Setup

In our research, we mainly used a scanning probe microscopy technique called scanning tunneling microscopy (STM). The STM method was born in Zurich, Switzerland, in 1982 and quickly spread worldwide. Nowadays, with its unique advantages, it has become an indispensable technology in surface science. Combining it with other surface characterization methods can provide a deeper and more comprehensive understanding of material properties.

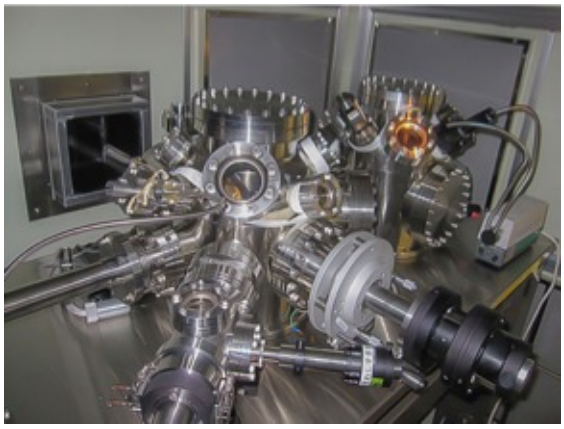

Figure 3.13 Scanning tunneling microscopy equipment.

The characteristic feature of STM is its use of the tunneling effect in close proximity for observation. Therefore, despite observing at the atomic and molecular level, it does not necessarily require a vacuum environment. Consequently, observation environments can vary

from vacuum to atmospheric, liquid, or gaseous conditions. However, limitations in the observation area and sensitivity to external environmental vibrations due to its operating principle are some drawbacks of STM.

In this study, we used a commercial STM system (JEOL, JSTM-4500XT), as shown in Figure 3.13. The JSTM-4500XT was developed as an ultra-high vacuum STM device that addresses the above-mentioned issues while offering numerous possibilities. Here, we will explain the concept of STM using this device as a representative example. The greatest feature of STM is its spatial resolution in real space, which is about 0.01 nm, allowing the observation of surface images of atoms and molecules, including light elements. Unlike electron microscopes that observe images through phase contrast, the resolution of STM corresponds to real-space images, reflecting the actual topography of the sample surface.

Currently, STM is most powerful in the study of local surface structures. By directly capturing the atomic arrangement of a solid surface as a real image, it becomes possible to understand the spatial fluctuations and inhomogeneities of the surface structure. This capability was not achievable with traditional surface structure observation methods such as LEED or RHEED, making STM an indispensable research method in this field. Furthermore, STM techniques have the advantage of very high depth resolution, allowing the investigation of the electronic states near the Fermi level of the surface. Utilizing this spectroscopic capability, it is possible to simultaneously examine the structure and electronic states of semiconductor devices, superlattice films, and superconducting materials, making it a highly effective method for material evaluation.

STM requires bringing a small metal tip very close to the sample surface (Figure 3.14), normally within about 1 nm, i.e., several atomic layers. This step is accomplished using a coarse positioning mechanism and piezoelectric scanner tubes. When the tip-sample separation is sufficiently close, a bias voltage is applied between the sample and the tip, allowing electrons to tunnel through this small gap and generate a tunneling current. This current is heavily dependent on the distance between the tip and the surface structures. As the probe scans the material surface, variations in surface morphology and electronic density lead to changes in the tunneling current. When the distance between the probe and the surface is kept constant, the image obtained through scanning represents a record of the tunneling current. If the STM probe and surface are controlled to maintain a constant current, the image reflects the voltage applied between the probe and the sample. In addition to STM imaging, there is another measurement technique called Scanning Tunneling Spectroscopy (STS). STS is used to understand the relationship between the tunneling current and the applied voltage, thereby obtaining the local density of electronic states of the material. Typically, these two measurement techniques are used together.

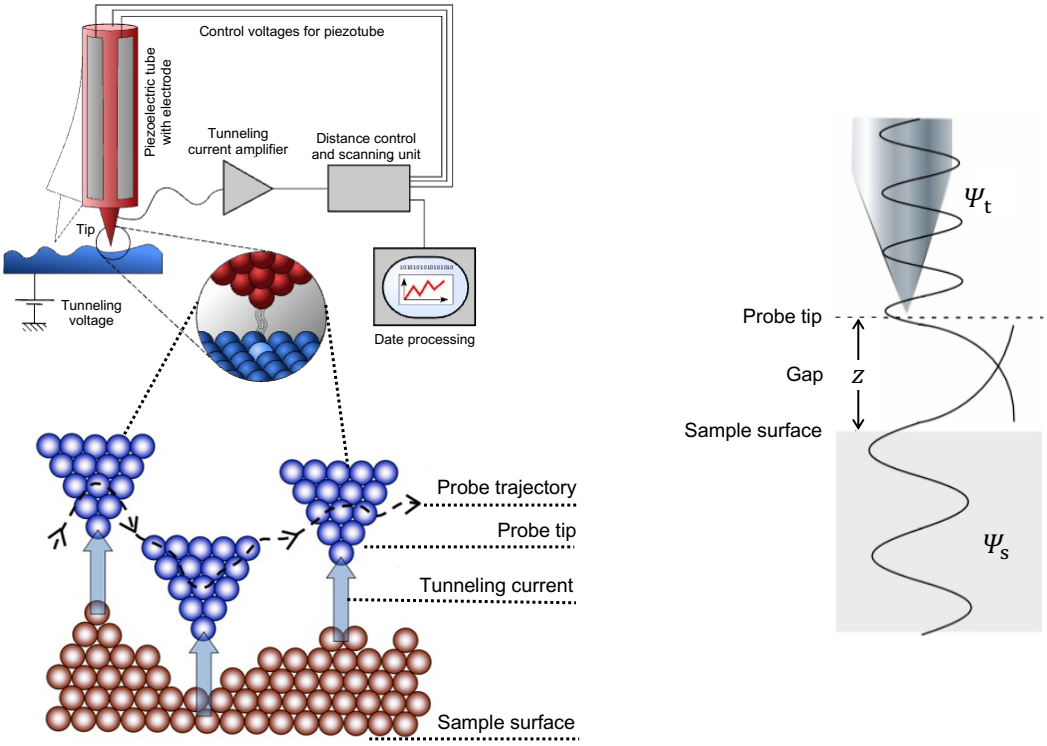

Figure 3.14 Schematic view of an STM and 1D tunneling configuration [20].

Overall, explaining the tunneling phenomenon in STM requires quantum mechanics. When the gap of the barrier (such as a vacuum) is sufficiently small, particles like electrons exhibit wave-like properties, allowing them to pass through. When the metal tip is placed within a sub-nanometer range of the sample surface, the 1D tunneling configuration shown in Figure 3.14 is created. The tunneling wave Ψ_s of the sample electrons and the wave Ψ_t of the STM tip electrons overlap in the insulating gap, allowing a current to flow.

Tunneling current

The tunneling current could be expressed as:

$$i_{s\to t} = -\frac{2\pi e}{\hbar}|M|^2(\rho_s(\varepsilon)\cdot f(\varepsilon))\cdot(\rho_t(\varepsilon - eV)\cdot[1 - f(\varepsilon - eV)]) \tag{3.1}$$

$$i_{t\to s} = -\frac{2\pi e}{\hbar}|M|^2(\rho_t(\varepsilon - eV)\cdot f(\varepsilon - eV))\cdot(\rho_t(\varepsilon)\cdot[1 - f(\varepsilon)]) \tag{3.2}$$

Where $i_{s\to t}$ and $i_{t\to s}$ tunneling of electrons from sample to tip, and from tip to sample at energy ε, and M is the tunneling matrix element, $\rho_s(\varepsilon)$ and $\rho_t(\varepsilon)$ are density of states (DOS) of the sample and the tip respectively, and $f(\varepsilon)$ is the Fermi function.

STM will measure both $i_{s\to t}$ and $i_{t\to s}$, and integrating over all energies gives

$$I = -\frac{4\pi e}{\hbar}\int_{-\infty}^{\infty}|M|^2\,\rho_s(\varepsilon)\rho_t(\varepsilon - eV)\big[f(\varepsilon)\cdot[1-f(\varepsilon-eV)]\big] - f(\varepsilon-eV)\cdot 1 - f(\varepsilon)]d\varepsilon \tag{3.3}$$

Considering the typical temperature (room temperature or below) of the measurements and a use of small voltage,

$$I \approx -\frac{4\pi e}{\hbar}\int_{0}^{eV}|M|^2\,\rho_s(\varepsilon)\rho_t(\varepsilon - eV)d\varepsilon \tag{3.4}$$

STM tip consist of Pt/Ir alloy which has a flat DOS around Fermi level. So, $\rho_t(\varepsilon - eV) \approx \rho_t(0)$, or DOS of the tip can be treated as a constant independent of energy ε.

$$I \approx -\frac{4\pi e}{\hbar}\rho_t(0)\int_{0}^{eV}|M|^2\,\rho_s(\varepsilon)d\varepsilon \tag{3.5}$$

Substitute $|M|^2 \approx e^{-2\frac{s}{\hbar}\sqrt{2m\varphi}}$ into Equation (3.5), the tunneling current that STM measures becomes

$$I \approx -\frac{4\pi e}{\hbar}e^{-s\sqrt{\frac{8m\varphi}{\hbar^2}}}\rho_t(0)\int_{0}^{eV}\rho_s(\varepsilon)d\varepsilon \tag{3.6}$$

Where m is the electron mass, s is the width of the vacuum barrier, and φ is the effective local barrier height, which represent some mixture of the tip and sample work functions.

Sample bias

The square magnitude of the wave function Ψ represents the probability of finding an electron at a given location. In simpler terms, this can be expressed as representing the distribution of electrons using an electron cloud. From the perspective of energy bands, Figure 3.15 shows the energy levels occupied by electrons, which can be observed using STM. In STM observations, by changing the polarity of the bias voltage, the direction of the tunneling current can be controlled. When $V_{\text{bias}} > 0$, electrons at the top of the valence band of the tip can tunnel through the vacuum to the conduction band of the sample. In this case, the STM observes the unoccupied states of the sample. Conversely, when $V_{\text{bias}} < 0$, the STM observes the occupied states of the sample. It is also important to note that the STM results are influenced by factors on the probe side.

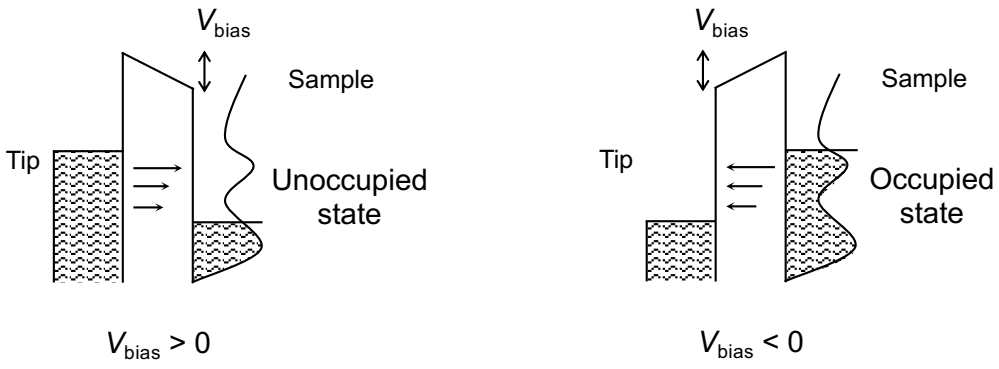

Figure 3.15 Schematic of an STM tunnel junction consisting of tip and sample.

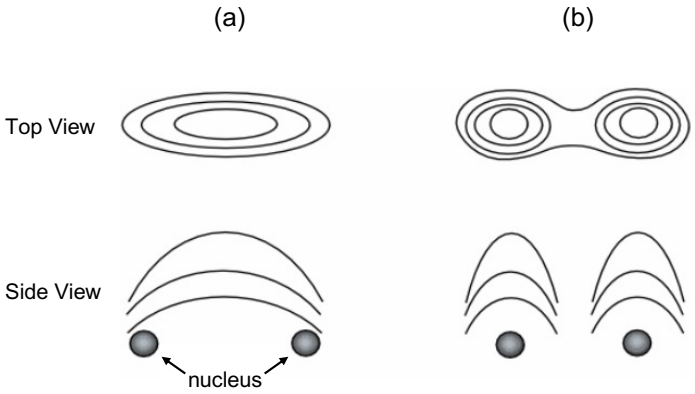

Figure 3.16 Sketch of possible STM images relative to the nucleus locations. Top View is the contouring lines of STM images and the corresponding side view on the bottom. STM image shows high tunneling location (a) at center of two nuclei and (b) at the top of each nucleus.

STM images provide information about the electronic distribution on the material's surface under specific bias voltages. We typically infer the positions of atoms based on this information, but such inferences are not always 100% accurate, as illustrated in Figure 3.16. In STM images, regions where electrons are concentrated appear as bright spots. In some cases, such as shown in Figure 3.16a, multiple atoms can appear as a single large electron cloud. This means that the area

with the highest electron density is not necessarily where the atomic nucleus is located. In Figure 3.17b, if the electron clouds near different atoms do not overlap significantly, they can accurately reflect the positions of the atoms.

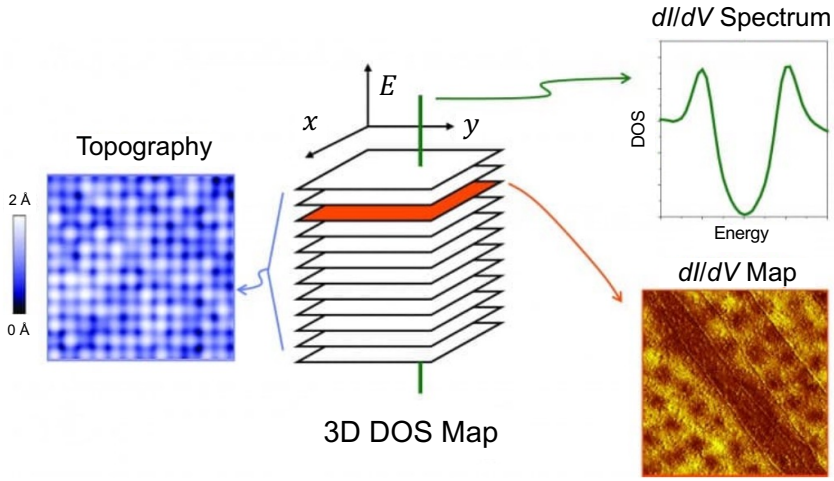

Figure 3.17 Schematic of 3-dimensional data sets obtained on a pixel grid (3D DOS maps) and main types of STM measurements.

Topographic imaging is the most common type of STM measurement (Figure 3.17). In our experiments, we also measured topographic images, which allow us to directly (approximately) see the surface structure of the sample.

In STM measurements, the constant current mode is the most commonly used. The current between the probe and the sample is highly sensitive to the distance between them. To maintain a constant current value, the STM system has a feedback loop that quickly adjusts the height of the probe. When the tunneling current exceeds the set value, the system raises the probe to decrease the current. By recording the trajectory of the probe tip, the surface contour of the sample can be mapped. The STM images obtained in this mode not only reflect the surface topography of the sample but also provide information about the electronic state density. Generally, it is difficult to distinguish between these two influences.

In Figure 3.17, another commonly used measurement technique is Scanning Tunneling Spectroscopy (STS), which yields dI/dV spectra. Its main feature is the ability to collect the electronic density of states on the surface over a wide energy range. The voltage range can cover both the valence and conduction bands, making it useful for understanding the band structure of

materials. Such characterization methods are standard tools in the exploration and research of new materials.

B. Previous STM Studies on Graphite and Graphene Surface

To use STM to observe nanocarbon materials, such as rGO nanosheets, we first need to select a suitable substrate to support the rGO. A highly oriented pyrolytic graphite (HOPG) substrate, which has ideal conductivity and an atomically flat surface, is commonly used for STM observations. Our STM experiments were performed on a commercial HOPG sample, as shown in Figure 3.18a. A fresh HOPG surface (Figure 3.18b) was created by cleaving the HOPG sample with adhesive tape in ambient air. After cleaving, the sample was immediately transferred to an ultrahigh vacuum (UHV: ~2×10^{-8} Pa) chamber for STM observations. No thermal treatments or baking were applied to the HOPG surface prior to observations. We used Pt/Ir tips that were mechanically cut and then cleaned by electron bombardment. Images were taken at room temperature in constant current mode using a commercial UHV STM system (JEOL, JSTM-4500XT).

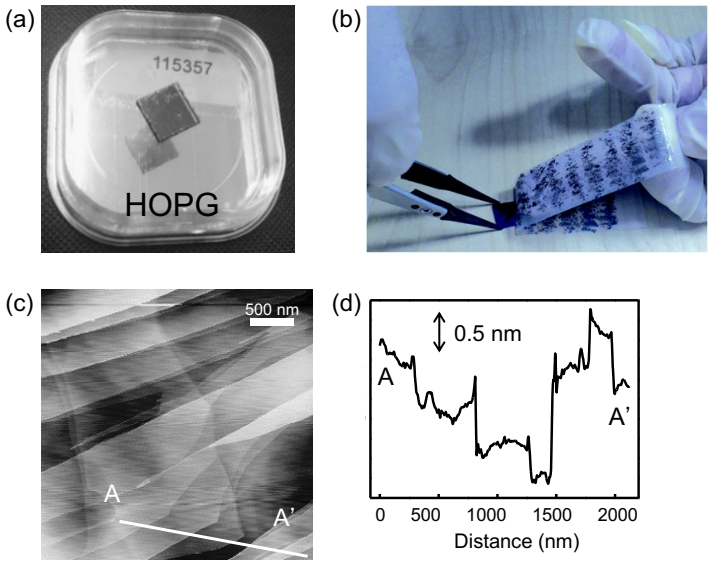

Figure 3.18 (a) HOPG sample. (b) The Scotch tap method. (c) An AFM image of HOPG surface. (d) Line profile taken along the line A–A' in (c).

To confirm the surface state of the HOPG, atomic force microscopy (AFM) was also conducted. From the results in Figures 3.18c and 3.18d, we can see that the HOPG substrate has a flat surface extending over several thousand nanometers. Although some step and terrace structures exist on the surface of the HOPG substrate, the width of the steps is generally sufficient for the dispersion of rGO nanosheets on its surface.

Graphite and Graphene Layers

Before introducing our STM experimental results, it is necessary to review past STM studies on graphene-related materials. These studies, which have been widely recognized, help in understanding our research findings. This is because the graphene-based nanomaterials we observed essentially belong to the graphene family, retaining the fundamental sp^2 framework.

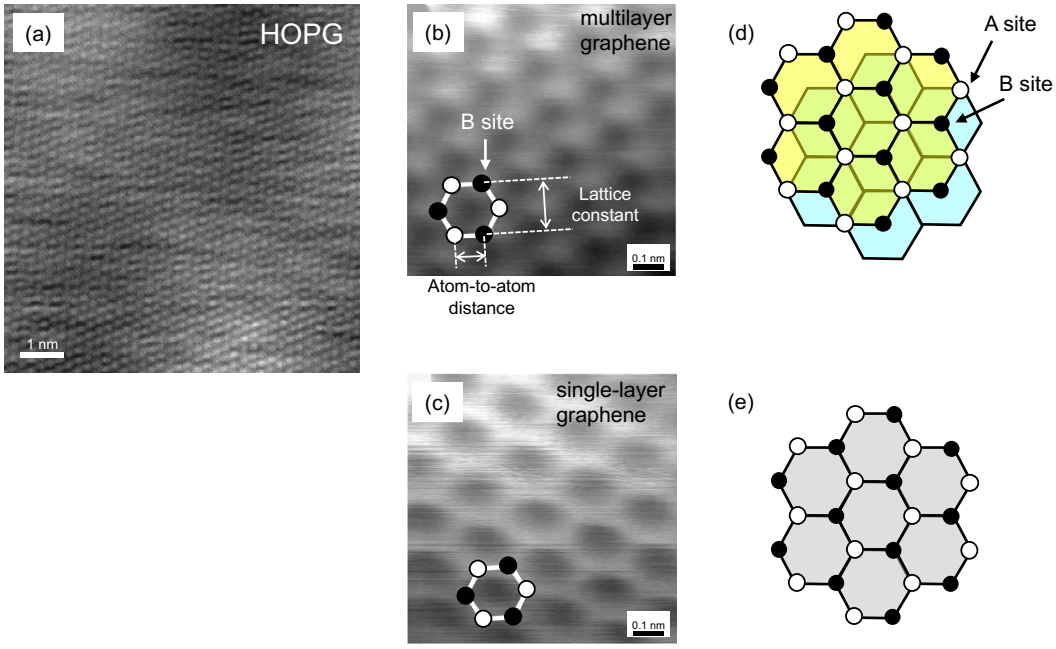

Figure 3.19 STM topographic images of the surface of (a) bulk graphite [21], (b) multilayer graphene [22], and (c) single-layer graphene. Ball and stick models for (b) and (c) are shown in (d) and (e), respectively.

Figure 3.19 shows atomically resolved STM images of bulk graphite, multilayer graphene, and single-layer graphene. First, the surface of graphite (Figure 3.19a) exhibits a regular triangular lattice with a lattice constant of ~0.25 nm, indicating a defect-free surface lattice. The multilayer

and single-layer graphene sheets observed in Figures 3.19b and 3.19c were both prepared by mechanical exfoliation. The multilayer graphene sheet (Figure 3.19b) displays the same threefold symmetry typical of the graphite crystal in Figure 3.19a. This feature can be readily interpreted in terms of the AB stacking of graphene planes in graphite. In bulk graphite or multilayer graphene, the carbon atoms on the surface are not equivalent. As shown in Figure 3.19d, half of the carbon atoms in the surface layer are located above carbon atoms in the adjacent lower layer (A sites), while the other half are sitting over a void (B sites). This asymmetry in the surface atom electronic environment results in a threefold symmetry ("three-for-six") pattern, where three bright or dark features can be observed for each set of six carbon atoms. The single-layer graphene crystal in Figure 3.19c exhibits a symmetrical honeycomb structure, where all surface atoms contribute equally to the tunneling images. And no atomic defects were found in the image, demonstrating a high degree of crystalline order in graphene prepared by mechanical exfoliation. The asymmetry present in the AB-type atoms of graphite and multilayer graphene is absent in single-layer graphene (Figure 3.19e). Therefore, all surface carbon atoms are identical, resulting in the symmetric honeycomb structure observed in the STM image.

Finite-sized Graphene Sheets

Finite-sized graphene has attracted attention for its peculiar electronic structure dependent on its dimensionality, size, and geometry. The electronic structure undergoes significant changes, and edge-localized electronic states are more characteristic, particularly as these materials become smaller. Therefore, directly observing finite-sized graphene, especially the local electronic structure near the edges, can provide deeper insights into the properties of nanographene.

Figure 3.20a shows an atomically resolved ultrahigh vacuum STM image of a hydrogenated step edge of HOPG. This step edge consists of a mix of zigzag and armchair types. The edge types are labeled in the image based on the hexagonal lattice. Bright spots are only seen in the areas near the zigzag edge, clearly showing the LDOS dependence on the edge structures. The STS data in Figure 3.20a also verifies the presence of the edge states at the zigzag edges (refer to references 4 and 5). Figure 3.20b shows a homogeneous armchair edge where no edge states are observed, instead showing a $(\sqrt{3} \times \sqrt{3})R30°$ superlattice. Only the LDOS of the p and p^* bands was observed in the dI/dV curve at the edge of this image, and the contribution of peaks similar to that in Figure 2(b) was negligibly small.

With the advancement of experimental equipment and methods, as well as the development of theoretical calculations, there has been a growing understanding of nanographene's electronic structure. For instance, in Figure 3.21a, a very clean, monolayer graphene armchair step edge is observed. In this image, changes in the electronic structure can be clearly detected: near the edge, a rhombic $(\sqrt{3} \times \sqrt{3})R30°$ superlattice is displayed, while the previously mentioned triangular lattice of the graphite surface appears in the interior. To date, this rhombic superlattice has been

regarded as an intrinsic electronic state of the armchair edge, and it can even be used to determine the nearby atomic structure.

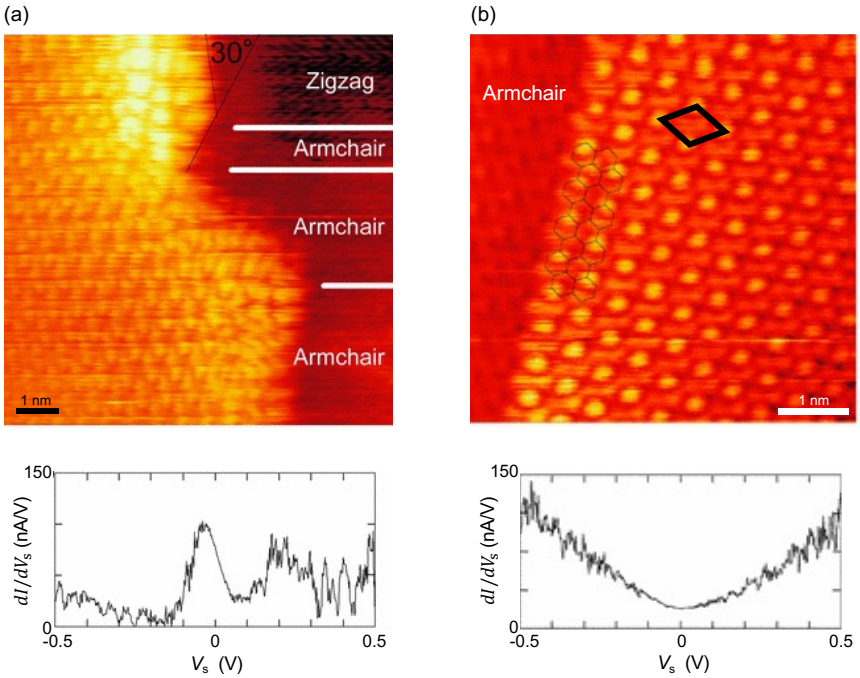

Figure 3.20 (a) An atomically resolved STM image of different edges and a typical dI/dV_s curve from STS data at a zigzag edge. (b) An atomically resolved STM image of a homogeneous armchair edge and a dI/dV_s curve from STS taken at the armchair edge [23].

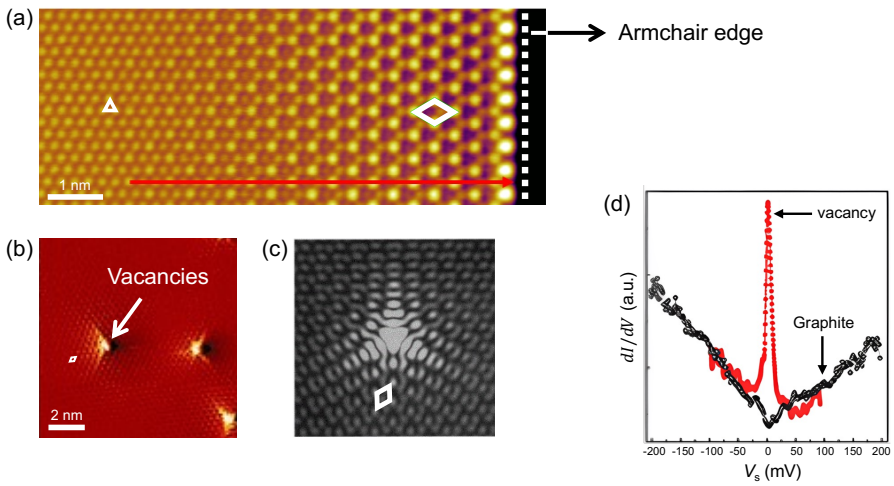

Figure 3.21 The $(\sqrt{3} \times \sqrt{3})R30°$ superstructure is observed in topographic images taken near

(a) a clean armchair edge [24] and (b) single vacancies [25]. (c) Computer simulation of an STM image due to a single point defect [26]. (d) STS measurements [25] of the LDOS induced by the single vacancy and of pristine graphite in (b).

Figure 3.21b shows the atomic-scale LDOS of artificially created isolated vacancies on a graphite surface. The previous pristine graphite surface now presents several point defects, which are surrounded by threefold $(\sqrt{3} \times \sqrt{3})R30°$ patterns. This result is similar to calculations (Figure 3.21c), suggesting that these defects correspond to single vacancies on both A and B atoms of the graphite honeycomb lattice. Additionally, there is a sharp electronic resonance at the Fermi energy (Figure 3.21d) around each single graphite vacancy, which may be related to the formation of local magnetic moments and implies a dramatic reduction of the charge carriers' mobility and an increase in chemical reactivity. In summary, in addition to the armchair step of graphite, a $(\sqrt{3} \times \sqrt{3})R30°$ superlattice is also observed near a single graphite vacancy. This might be associated with changes in the magnetic and chemical properties of graphene materials.

3.4 ATOMIC-LEVEL STM IMAGES OF FINITE-SIZE GRAPHENE-BASED MATERIALS

This section mainly introduces the atomic-scale STM images of nanographene sheets observed on an HOPG substrate, including reduced graphene oxide (rGO) and pristine graphene. Our focus is on the distinctive electronic structures near the edges of small graphene and rGO sheets. In addition to the well-known lattice structures introduced in the previous section, we have discovered a new type of rectangular-like lattice. This peculiar electronic structure also appears to be influenced by the edge structure. This section details the discovery and examination of this rectangular-like structure, as well as how we plan to verify its origin through calculations.

A. Experimental Methods

Sample Preparation

The rGO sheet used in the STM experiment was prepared as shown in Figure 3.22. By adding hydrazine monohydrate to a GO solution, an rGO suspension was obtained. For details and other types of chemical synthesis of rGO, please refer to the description in Figure 2.12. It should be noted that if these suspensions are not used for a long time, their dispersion state will deteriorate.

Therefore, the rGO solution needs to be ultrasonically treated before each experiment. When the reduced graphene solution was obtained, we dispersed it on the cleaved HOPG substrate by spin-coating. After drying with N_2 gas, it was transferred into the STM's chamber, where it was ready for observation.

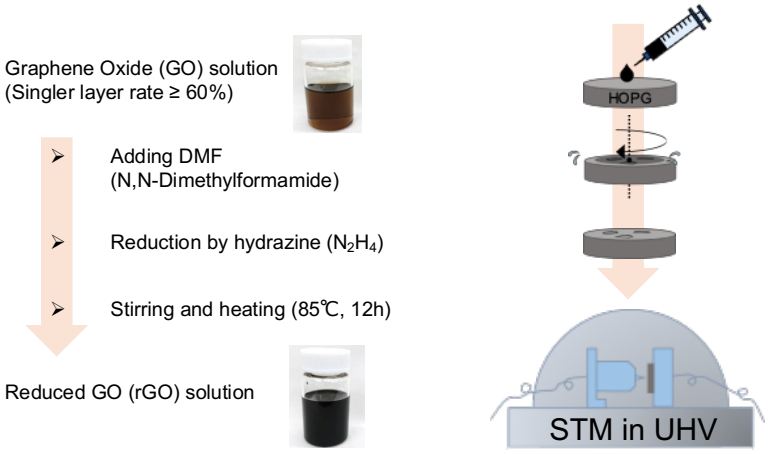

Figure 3.22 Preparation of samples prior to STM observation.

The size of the rGO sheets on HOPG after spin-coating can be adjusted by sonication of the rGO solution. Although the relevant data is not shown here, our research confirms that prolonged sonication can yield smaller graphene sheets.

Table 3.1 STM experimental conditions.

SPM parameters	
Image	STM: Topography
Tunnel Current	0.200 nA
Sample Bias	-0.050 V
No of pixels	(512,512)
Clock speed	66.70 μs or 33.30 μs
Feedback Filter	0.2 Hz
Z Filter	50.0 kHz
Preamp Filter	50.0 kHz
Preamp Gain	1.00 V/nA
Loop Gain	2

In addition to the rGO nanosheets mentioned above, we also observed pristine graphene nanosheets on the HOPG surface. The preparation method is relatively simple, involving the cleavage of HOPG with adhesive tape to obtain a fresh surface. During this process, step-like structures and small exfoliated graphene sheets are formed in local regions.

STM Observation

Images were taken at room temperature in constant current mode using a commercial UHV STM system (JEOL, JSTM-4500XT). If not specified otherwise, our STM experimental conditions are as shown in Table 1.

B. Electronic Structure of RGO and Graphene Nanosheets

Figure 3.23 shows an image on a rGO sheet [27] dispersed on HOPG. Sample bias (V_s) and tunnel current (I_t) were set to −0.01 V and 0.1 nA, respectively. In Figure 3.23a, a small flake exists, part of which is enlarged in Figure 3.23b. The atomic-scale corrugations of the flake in Figure 3.23b are mainly composed of two superstructures. One has rhombus and the other has rectangular-like lattices, as shown in Figures 3.23c and 3.23d, respectively. The rhombic phase, known as $(\sqrt{3} \times \sqrt{3})R30°$ superstructure, has been reported by many groups on graphite surfaces near complete or defective armchair edges [28], as well as on graphene grown on SiC [29].

Figure 3.24a shows an STM image of a small pristine graphene sheet [27] on HOPG. The cross-sectional profile along the *p*–*p*' line in Figure 3.24a is provided in Figure 3.24b. Except for the right edge, the sheet thickness in Figure 3.24b is measured to be approximately 0.5 nm, as indicated by an arrow. At the right side of the sheet in Figure 3.24a, there exists a hollow. It is probable that the graphene sheet in Figure 3.24a was partially exfoliated from the HOPG surface and then folded to leave a hollow at its right-hand side, as schematically depicted in Figure 3.24c. The measured thickness of the graphene sheet in Figure 3.24b is larger than the theoretical value of 0.34 nm, which corresponds to the monoatomic step height of a graphite surface. This is probably due to nonplanar deposition of the graphene sheet [30], leading to the formation of wrinkles. Adsorbed molecules on graphene are also known to increase a measured thickness [31]. Note that there are two possible origins to form such a folded graphene sheet. One of the origins of formation is during the cleavage of the HOPG surface by adhesive tape. The other is the vertical displacement of the top graphene layer from the substrate mediated by the interaction of an STM tip with the HOPG sample [32]. In previous studies, such STM manipulation has been used for producing graphene nanoribbons [33,34]. In this work, we focus on the superstructures on the folded graphene sheet in Figure 3.24a.

Figure 3.24d shows a magnified STM image of the monolayer graphene sheet in Figure 3.24a.

The image exhibits atomic-scale bright dots that form different patterns. Figures 3.24e–3.24g show the typical three patterns extracted from Figure 3.24d wherein the gray scale was adjusted to highlight atomic corrugations. On the HOPG terrace, there exist triangular lattices, as shown in Figure 3.24e. As explained several times before, Bernal stacking is the most reliable hypothesis for their observations [35,36], and a lattice distance between neighboring dots is ~0.25 nm. On the folded sheet in Figure 3.24d, there exists a rhombus pattern, an example of which is shown in Figure 3.24f. For later discussion, the lengths of the long and short diagonals of this rhombus lattice were analyzed and determined to be 0.75 ± 0.01 and 0.46 ± 0.01 nm, respectively. Considering this size, it is reasonable to assume that the rhombus represents the $(\sqrt{3} \times \sqrt{3})R30°$ superstructure.

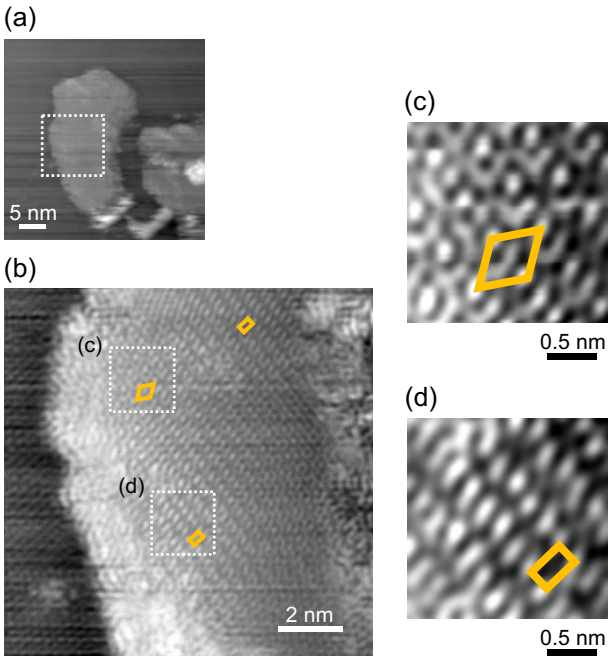

Figure 3.23 (a) STM image of a HOPG surface loaded with a rGO sheet. (b) Enlarged STM image of the area indicated by the dotted line in (a). Dot patterns exhibiting (c) $\sqrt{3} \times \sqrt{3}$ and (d) rectangular lattices in (b) [27].

In addition, it is striking that another rectangular quadrangle lattice (Figure 3.24g) is clearly visible on the folded sheet, which resembles to the ones observed in Figure 3.23. This phase, which is hereafter referred to as a "rectangular lattice," was confirmed at different areas on the

sheet; two examples are indicated in Figure 3.24d. The rectangular lattice has long and short sides with lengths of 0.37 ± 0.02 and 0.22 ± 0.01 nm, respectively. A notable feature in Figure 3.24g is that the long-side direction of the lattice is the same as, or parallel to, that of the long diagonal of the $\sqrt{3} \times \sqrt{3}$ phase in Figure 3.24f. Another feature observed is that, in contrast to circular bright dots at the vertices of the $\sqrt{3} \times \sqrt{3}$ phase in Figure 3.24f, those of the rectangular lattice tend to be elongated along its long-side direction in Figure 3.24g. The sizes of the rectangular lattice and these above-mentioned features match those in Figure 3.23, which indicate that this unique lattice is not a "ghost" image due to tip conditions but is derived from intrinsic electronic structure in the small graphene sheets.

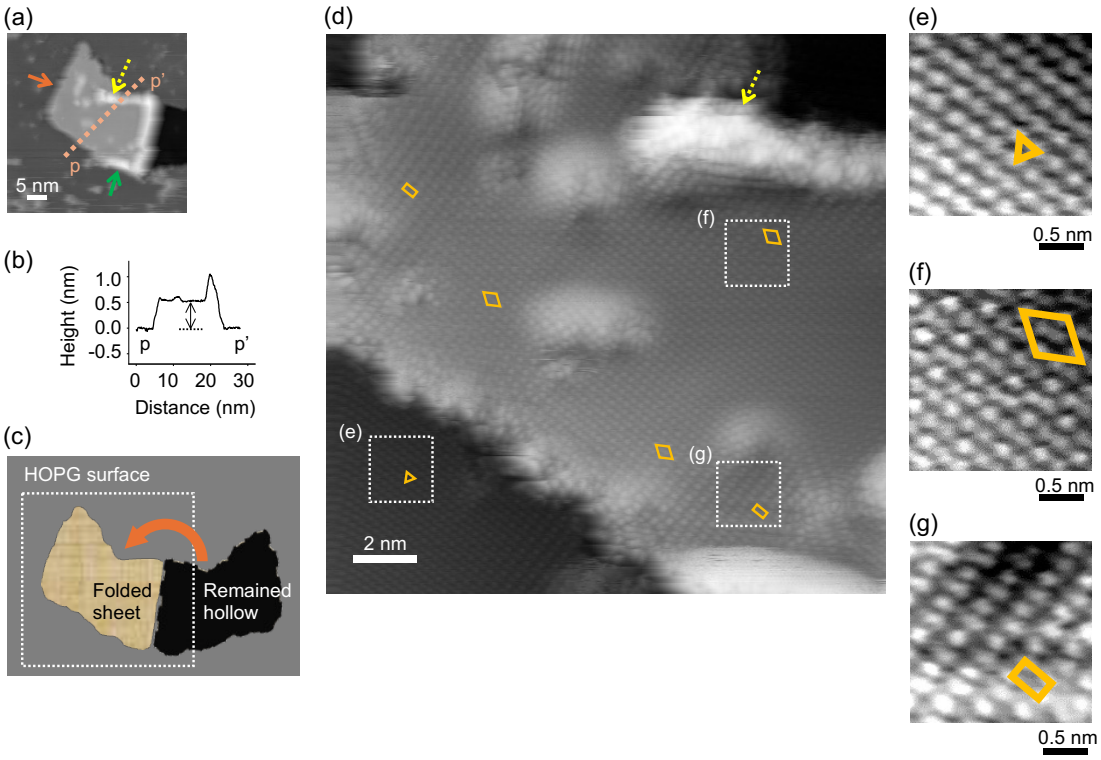

Figure 3.24 (a) STM image of a small graphene sheet on HOPG. The solid arrows pointing toward an outer edge or a protrusion are placed on the image for later discussion. (b) Height profile along p-p' in (a). (c) Schematic depiction of the graphene sheet corresponding to (a); the dotted area indicates the region imaged in (a). (d) Magnified STM image of the folded sheet in (a). The dotted arrows in (a) and (d) indicate the same position. (e)–(g) Typical distributions of bright dots in (d). The unit cells of (e) triangular, (f) rhombohedral, and (g) rectangular lattices are superimposed in each image.

Regarding the folded single-layer graphene sheet in Figure 3.24, we performed continuous probe scanning (observation) of the same area. Three typical images are shown in Figure 3.25. It should be noted that Figure 3.25a and Figure 3.24a are the same, only with some arrows and dashed lines removed. Two hypotheses were previously proposed regarding the formation of the folded single-layer graphene sheet in Figure 3.25a (and Figure 3.24a). In Figure 3.25b, it is evident that this tiny graphene sheet has undergone another fold. Only one minute elapsed between the recordings of Figures 3.25a and 3.25b. The results in Figure 3.25 are most likely due to the interaction between the probe and the substrate, which is quite common in STM scans. In subsequent observations, we obtained Figure 3.25c. Unlike the previous two images, it is difficult to determine the cause of its formation from the image or to establish its connection with the previous scan results. Here, I personally lean towards the idea that Figure 3.25c is formed by the in-plane translation and rotation of the topmost graphene sheet in Figure 3.25b rather than by the previous folding mechanism.

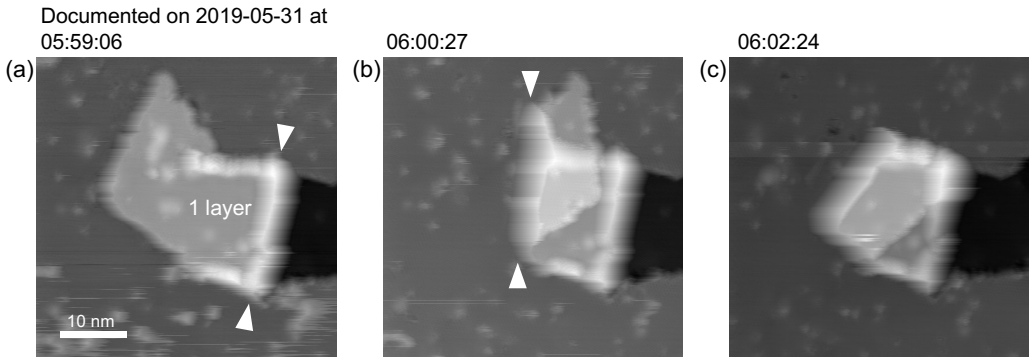

Figure 3.25 STM images obtained from successive scans of the same place. (a)–(c) The folding process of a small graphene sheet. The approximate creases are indicated with solid arrows.

Over a considerable period, the graphene nanosheet maintained the folded state shown in Figure 3.25c without any noticeable deformation. We conducted a detailed investigation of this sample (Figure 3.26). We aimed to gain more insight into the interior of such small graphene sheets, particularly whether special electronic structures, such as the rectangular lattice observed in Figures 3.23 and 3.24, could be seen near the edges.

In contrast, the nanosheet in Figure 3.26 had undergone at least two folds (multilayer graphene).

Furthermore, most of its edges were not the typical zigzag, armchair, or a mix of both, but rather a type of crease. In much literature [37,38], this crease is referred to as a ripple or wrinkle structure. Therefore, this presents a good opportunity to understand the different impacts that ordinary edges and creases might have on the nanosheet.

Figure 3.26a is an enlarged view of the area below the nanosheet shown in Figure 3.25c. As shown in Figure 3.26b, we again observed a rectangular lattice near the dotted arrows. This region is also adjacent to the edge structures. We also observed a rectangular structure near the solid arrows. This bright strip region indicates the crease, and its overall electronic state is similar to the electronic states of zigzag edges described in previous literature (high electron density, etc.). Additionally, we observed a rhombic superstructure close to what appears to be a vacancy defect and a triangular lattice on the HOPG substrate, all of which are indicated in the image. Figure 3.26 suggests that such a rectangular structure can be observed in graphene's crease regions, also known as wrinkle structures.

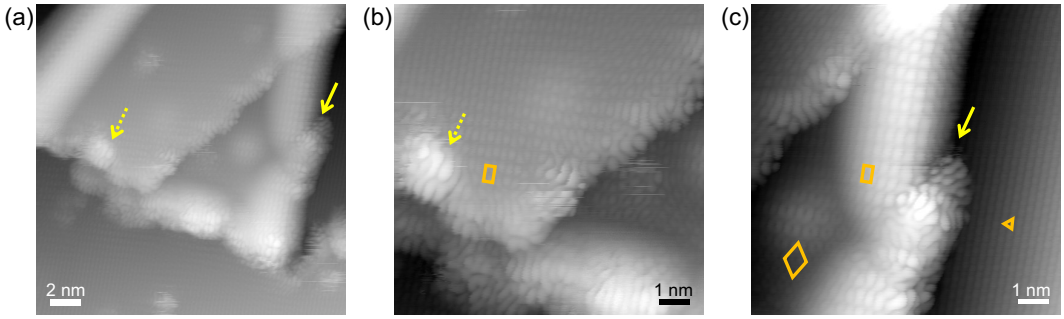

Figure 3.26 STM images near wrinkled structures. (a) A small, folded graphene sheet. The magnified images in (a) and shown in (b) and (c). The dotted arrows in (a) and (b) indicate the same position. Similarly, the solid arrows in (a) and (c) also indicate the same position.

C. Origin of Rectangular Lattice within Nanographene

Other research groups [39,40] have also observed rectangular lattices similar to those in Figure 3.24g on graphene-based materials. However, except for one group [41], the imaging mechanism has not been discussed in detail (Figure 3.27). Pandey et al. reported STM observations of GO sheets deposited on HOPG, revealing a unit cell with a size of 0.406×0.273 nm^2 over distances spanning a few nanometers. This structure was observed in 50% of the high-resolution STM scans performed on GO sheets. They insisted that the unit cell originated from oxygen functional groups

bound to carbon atoms in the GO sheets. Interestingly, our rectangular lattice in Figure 3.24g resembles the shape reported in the literature. However, the possibility of oxidation on the sample surface observed in Figure 3.24 is minimal. Furthermore, the size of our rectangular lattice differs, indicating that it was likely created by a mechanism other than the periodic distribution of oxygen functionalities.

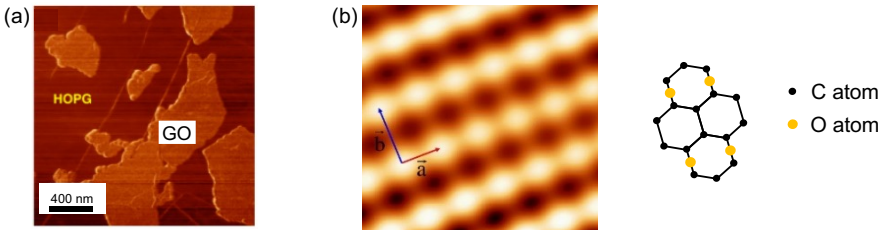

Figure 3.27 (a) A lateral force image of GO flakes on HOPG. (b) STM image of a GO flake revealing a rectangular lattice [41].

Based on subsequent experimental observations and analysis of the results, we found that the short-side length of the rectangular lattice in Figure 3.24g is almost half of the short diagonals of the $\sqrt{3} \times \sqrt{3}$ lattices in Figure 3.24f. Considering the aligned directions of the two lattices in Figures 3.24f and 3.24g, as previously described, one possible explanation for the creation of the rectangular lattice in Figure 3.24g is the overlap of two different $\sqrt{3} \times \sqrt{3}$ superstructures.

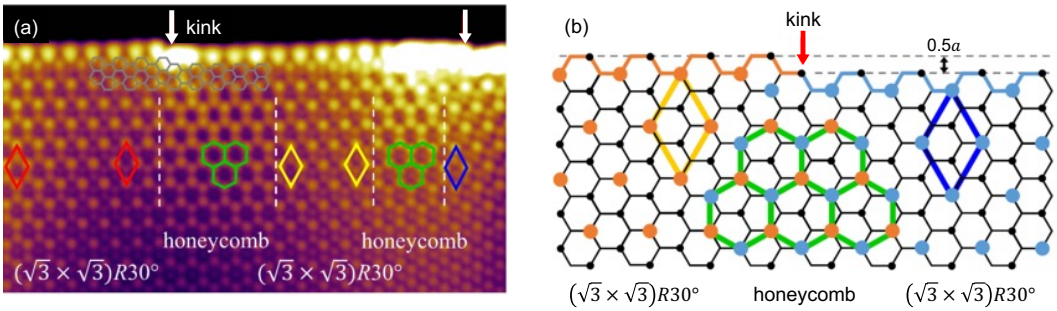

Figure 3.28 STM image of the armchair step edge with a mixture of $(\sqrt{3} \times \sqrt{3})R30°$ and honeycomb superstructures. The honeycomb superstructure is due to overlap of two sets of intrinsic $(\sqrt{3} \times \sqrt{3})R30°$ superstructures with a phase shift. (b) Lattice structure showing that the honeycomb superstructure emerges in the middle of armchair edges with a lattice offset. It is

a result of overlapping of two sets of $(\sqrt{3} \times \sqrt{3})R30°$ superlattices with a phase difference [24].

Recently, another group presented a detailed STM study of a graphite surface with monoatomic armchair step edges [24]. They visualized a coexistence of $(\sqrt{3} \times \sqrt{3})R30°$ and honeycomb superstructures near structurally defective armchair step edges (Figure 3.28a). There are two kinks marked by solid arrows along the edge. The atomic row of terminating carbon atoms on the two sides of the kink has an offset of half the lattice constant (a) perpendicular to the edge. Note that the $(\sqrt{3} \times \sqrt{3})R30°$ superstructure is always located right under a homogeneous part of the armchair edge, while the honeycomb superstructure is visible near the kink between two parts of the armchair edge. They claimed that the honeycomb pattern results from the lateral superposition of two sets of $(\sqrt{3} \times \sqrt{3})R30°$ superstructures with different phases, as shown in Figure 3.28b. It is important to note that such a honeycomb superstructure does not appear at linear and defect-free monoatomic armchair step edges. Inspired by their work, we propose that rectangular lattices in Figure 3.24g are formed by another overlap or a superposition of two sets of the $\sqrt{3} \times \sqrt{3}$ phase along the long diagonal direction.

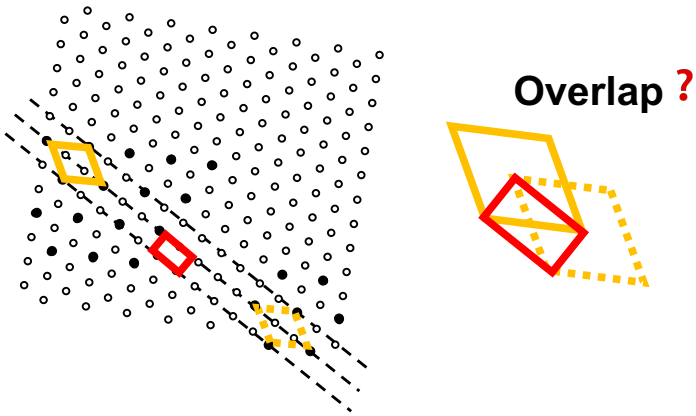

Figure 3.29 Schematic diagram of a conjecture about the overlapping of two sets of $(\sqrt{3} \times \sqrt{3})R30°$ superstructures and the formation of a rectangular lattice.

To better understand the overlap hypothesis proposed in our experimental results, the features were summarized again as follows:

- The long-side direction of the rectangular lattice is the same as, or parallel to, that of the long diagonal of the $\sqrt{3} \times \sqrt{3}$ phase.

- In contrast to the circular and bright dots on the HOPG terrace, the dots at the vertices of the rectangular lattice tend to be elongated along its long-side direction.
- In terms of size, the short-side length of the rectangular lattice is almost half of the short diagonals of the $\sqrt{3} \times \sqrt{3}$ lattices.

We plan to verify this hypothesis using theoretical calculations. An introduction to the preliminary calculations is provided later, and a detailed discussion will be reported in Chapter 4.

So far, the sample voltages (V_S) used in our STM experiments have been low, such as -0.01 V or -0.05 V. We have also attempted to change the V_S in STM experiments to investigate its effect on the rectangular structures. The specific steps involved observing graphene nanosheets or graphite step edges and attempting to recapture the previously described rectangular lattice under low-voltage scanning. Then, we would change the V_S and observe whether the rectangular lattice obtained under low voltage could be observed in the same area or if any other electronic structures would appear. The positive V_S was also taken into account during the scanning.

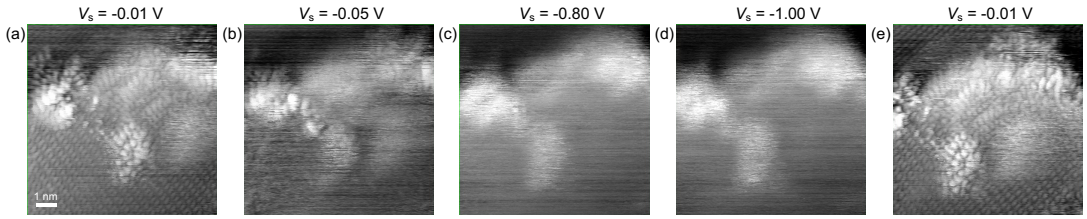

Figure 3.30 STM images of an rGO sheet. Images in (a)–(e) were taken with different sample biases. Tunnel current is 0.1 nA.

Figure 3.30 illustrates a typical example of such an experiment. Under low-voltage observation, the lower part of the image of this graphene nanosheet appears to have a rectangular structure (Figure 3.30a). However, as we gradually increased the absolute value of V_S in Figures 3.30b–3.30d, all the features, including the bright spots, became blurred. The rectangular lattice, or its variations, could not be determined. This is mainly because, in the constant current mode, increasing the absolute value of the voltage causes the probe to scan the outer layer of the electron cloud on the sample surface. When we returned to a low voltage (Figure 3.30e), we observed features similar to those in Figure 3.30a at the same location, including the rectangular lattice. This also confirms the authenticity of the results in Figure 3.30a, which is one of the commonly used methods in our STM experiments.

3.5 STRATEGY FOR SIMULATING STM IMAGES OF GRAPHENE NANORIBBONS

Not only does our research require the use of computational methods, but many past STM studies of graphite surfaces have also employed computations to replicate experimentally obtained electronic structures, identify atomic structures, and expand theoretical hypotheses. Below, we present the early theoretical calculation [42] of graphene in Figure 3.31.

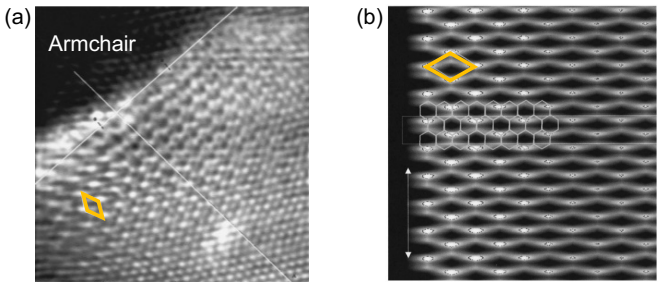

Figure 3.31 STM image of an “armchair” type step edge termination in graphite. The lines indicate the bulk graphite lattice is approximately normal to the edge. (b) Simulated STM image of armchair terminated graphene step edge. The atomic lattice of the graphite crystal is shown as a $(\sqrt{3} \times \sqrt{3})R30°$ superstructure [42].

Figure 3.31a shows a STM image of the step edge on a graphite surface. According to the atomic configuration, as guided by the white lines, the edge is identified as an "armchair" type edge. Near the edge, the $(\sqrt{3} \times \sqrt{3})R30°$ lattice is marked with a rhombus pattern. Mimicking this configuration, the authors performed calculations for a graphene nanoribbon in Figure 3.31b. Although the term "graphene nanoribbon" is used in the literature, it is essentially a semi-infinite graphene sheet with an armchair edge on one side (the left side of Figure 3.31). In this calculation of the electronic states, the $(\sqrt{3} \times \sqrt{3})R30°$ lattice observed at the edge corresponds well with the experimental results.

To verify the hypothesis in Figure 3.29, we constructed a simple model to calculate its electronic structure. Taking Figure 3.32 as an example, we will first briefly introduce the model used for the calculations. Then we will explain why this model (atomic configuration) was chosen. Finally, we will describe our calculation strategy (which parameters to change) to achieve our

expected results.

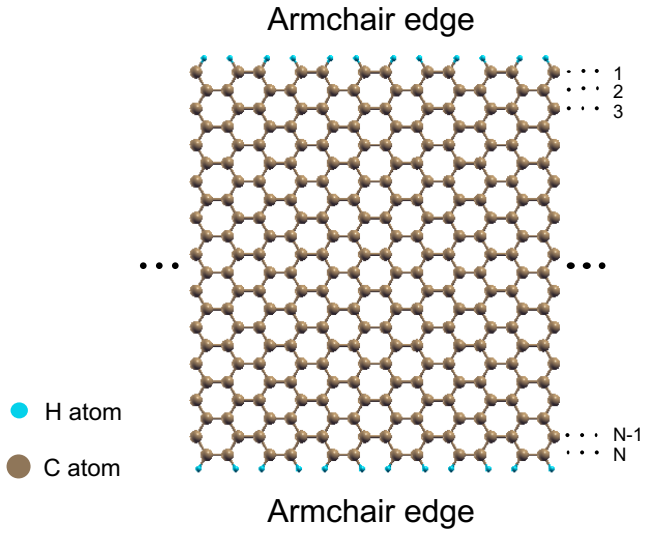

Figure 3.32 Schematic of the AGNR model for simulations. The edge dangling σ bonds are passivated by hydrogen atoms.

As previously introduced in Figure 3.5c, Figure 3.32 is an AGNR model. In terms of ribbon width, N is an integer defined as the number of dimer lines across the ribbon width. The key point is that both sides of the nanoribbon have armchair edges. This is because the $(\sqrt{3} \times \sqrt{3})R30°$ superstructure is an inherent electronic structure that exists near the armchair edge. Moreover, this superstructure disappears in the interior of graphene, far from the armchair edge. If we construct a GNR with armchair edges on both sides, we expect the rhombic superstructure to form on both sides of the nanoribbon. If the width of the nanoribbon is sufficiently short (or just right), it creates the conditions for the overlap (interference) of two sets of $(\sqrt{3} \times \sqrt{3})R30°$ lattice from different origins.

In other words, in the following calculations, we need to adjust the width of the AGNR (N in Figure 3.32). If necessary, we may need to change the nanoribbon's edge configuration, such as using defective armchair edges similar to those in Figure 3.28. We might even consider multilayer graphene or bulk graphite to simulate the substrate's effect on the electronic states of the topmost graphene layer. Additionally, due to various reasons, we did not complete the investigation of the dependence of the electronic structure on sample biases in the experimental part, an issue that still requires attention.

REFERENCES

1) M. Terrones, A. R. Botello-Méndez, J. Campos-Delgado, F. López-Urías, Y. I. Vega-Cantú, F. J. Rodríguez-Macías, A. L. Elías, E. Muñoz-Sandoval, A. G. Cano-Márquez, J.-C. Charlier, H. Terrones, Nano Today 5 (2010) 351-372.
2) J. Hass, W. A. de Heer, E. H. Conrad, J. Phys.: Condens. Matter 20 (2008) 323202.
3) Y. Baskin, L. Meyer, Phys. Rev. 100 (1995) 544.
4) M. Fujita, K. Wakabayashi, K. Nakada, K. Kusakabe, J. Phys. Soc. Jpn. 65 (1996) 1920-1923.
5) K. Nakada, M. Fujita, G. Dresselhaus, M. S. Dresselhaus, Phys. Rev. B 54 (1996) 17954-17961.
6) M. J. Allen, V. C. Tung, R. B. Kaner, Chem. Rev. 110 (2010) 132.
7) A. K. Geim, Science 324 (2009) 1530.
8) C. N. R. Rao, A. K. Sood, K. S. Subrahmanyam, A. Govindaraj, Angew. Chem. Int. Ed. Engl. 48 (2009) 7752.
9) S. Park, R. S. Ruoff, Nat. Nanotechnol. 4 (2009) 217.
10) H. Bai, C. Li, G. Shi, Adv. Mater. 23 (2011) 1089-1115.
11) W. S. Hummers, R. E. Offeman, J. Am. Chem. Soc. 80 (1958) 1339.
12) S. Stankovich, D. A. Dikin, R. D. Piner, K. A. Kohlhaas, A. Kleinhammes, Y. Jia, Y. Wu, S. T. Nguyen, R. S. Ruoff, Carbon 45 (2007) 1558.
13) C. Berger, Z. Song, X. Li, X. Wu, N. Brown, C. Naud, D. Mayou, T. Li, J. Hass, A. N. Marchenkov, E. H. Conrad, P. N. First, W. A. de Heer, Science 312 (2006) 1191.
14) K. Erickson, R. Erni, Z. Lee, N. Alem, W. Gannett, A. Zettl, Adv. Mater. 22 (2010) 4467-4472.
15) H. Hu, J. H. Xin, H. Hu, X. Wang, Y. Kong, Applied Catalysis A: General 492 (2015) 1-9.
16) D. Xue, H. Xia, W. Yan, J. Zhang, S. Mu, Nano-Micro Lett. (2021) 13:5.
17) S. Tang, Z. Cao, Phys. Chem. Chem. Phys. 14 (2012) 16558-16565.
18) W. Zhang, S. Wang, J. Ji, Y. Li, G. Zhang, F. Zhang, X. Fan, Nanoscale, 5 (2013) 6030-6033.
19) J. I. Paredes, S. Villar-Rodil, P. Solís-Fernández, A. Martínez-Alonso, J. M. D. Tascón, Langmuir 25 (2009) 5957-5968.
20) https://en.wikipedia.org/wiki/Scanning_tunneling_microscope.
21) J. Osing, I. V. Shvets, Surface Science 417 (1998) 145-150.
22) E. Stolyarova, K. T. Rim, S. Ryu, J. Maultzsch, P. Kim, L. E. Brus, T. F. Heinz, M. S. Hybertsen, G. W. Flynn, PNAS 104 (2007) 9209-9212.

23) Y. Kobayashi, K. Fukui, T. Enoki, K. Kusakabe, Y. Kaburagi, Phys. Rev. B 71 (2005) 193406.
24) W. Zhang, Z. Ju, W. Wu, Phys. Rev. B 100 (2019) 115120.
25) M. M. Ugeda, I. Brihuega, F. Guinea, J. M. Gómez-Rodríguez, Phys. Rev. Lett. 104 (2010) 096804.
26) H. A. Mizes, J. S. Foster, Science 244 (1989) 559.
27) J. Li, S. Li, T. Higashi, K. Kawai, K. Inagaki, K. Yamamura, K. Arima, Phys. Rev. B 103 (2021) 245433.
28) Y. Niimi, T. Matsui, H. Kambara, K. Tagami, M. Tsukada, H. Fukuyama, Phys. Rev. B 73 (2006) 085421.
29) M. Ye, Y. T. Cui, Y. Nishimura, Y. Yamada, S. Qiao, A. Kimura, M. Nakataka, H. Namatame, M. Taniguchi, Eur. Phys. J. B 75 (2010) 31.
30) X. Zhang, H. Luo, Appl. Phys. Lett. 103 (2013) 231602.
31) V. C. Tung, M. J. Allen, Y. Yang, R. B. Kaner, Nat. Nanotechnol. 4 (2009) 25.
32) H. S. Wong, C. Durkan, N. Chandrasekhar, ACS Nano 3 (2009) 3455.
33) P. Ruffieux, S. Wang, B. Yang, C. Sánchez-Sánchez, J. Liu, T. Dienel, L. Talirz, P. Shinde, C. A. Pignedoli, D. Passerone, T. Dumslaff, X. Feng, K. Müllen, R. Fasel, Nature 531 (2016) 489-492.
34) L. J. Yin, W. X. Wang, K. K. Feng, J.-C. Nie, C. M. Xiong, R.-F. Dou, D. G. Naugle, Nanoscale 7 (2015) 14865-14871.
35) S. I. Park, C. F. Quate, Appl. Phys. Lett. 48 (1986) 112.
36) D. Tománek, S. G. Louie, Phys. Rev. B 37 (1988) 8327.
37) J. A. Baimova, E. A. Korznikova, S. V. Dmitirev, B. Liu, K. Zhou, Curr. Nanosci. 12 (2016) 184.
38) W. Zhu, T. Low, V. Perebeinos, A. A. Bol, Y. Zhu, H. Yan, J. Tersoff, P. Avouris, Nano Lett. 12 (2012) 3431.
39) R. M. Jacobberger, B. Kiraly, M. Fortin-Deschenes, P. L. Levesque, K. M. McElhinny, G. J. Brady, R. Rojas Delgado, S. Singha Roy, A. Mannix, M. G. Lagally, P. G. Evans, P. Desjardins, R. Martel, M. C. Hersam, N. P. Guisinger, M. S. Arnold, Nat. Commun. 6 (2015) 8006.
40) A. Luican-Mayer, J. E. Barrios-Vargas, J. T. Falkenberg, G. Autès, A. W. Cummings, D. Soriano, G. Li, M. Brandbyge, O. V. Yazyev, S. Roche, E. Y. Andrei, 2D Mater. 3 (2016) 031005.
41) D. Pandey, R. Reifenberger, R. Piner, Surf. Sci. 602 (2008) 1607.
42) P. L. Giunta, S. P. Kelty, J. Chem. Phys. 114 (2001) 1807-1812.

C H A P T E R

4

THE FIRST-PRINCIPLES CALCULATIONS ON ARMCHAIR-EDGED GRAPHENE NANORIBBON (AGNR)

In this chapter, we first introduce the development and basic concepts of computational science in Sec. 4.1. Then, we discuss the theories, computational tools, and supercomputer systems, as well as the computational goals and processes used in our study (Sec. 4.2). Sec. 4.3 to Sec. 4.5 provide a detailed description of the calculations of STM images of graphene nanoribbons. We investigate the effects on the electronic properties of graphene nanoribbons from three aspects: the width of the nanoribbons, the sample bias used in the calculations, and the internal wrinkle structures of the nanoribbons. Finally, we present a summary in Sec. 4.6.

4.1 INTRODUCTION

Experimental studies have traditionally been the primary approach in materials research, but theoretical simulations are now assuming a progressively prominent role. Historically, physical principles were limited to the study of pure crystals and were unable to account for the intricate features of real materials, including flaws and grain boundaries. Nevertheless, recent breakthroughs in computer technology have facilitated this achievement. During the 1980s, researchers and industry professionals utilized molecular orbital (MO) simulations to analyze the characteristics of substances that were of significance in their respective fields. Currently, it is customary to initially employ MO calculations to design desired compounds, subsequently validate the theoretical outcomes through experimental trials, and ultimately achieve the synthesis of the compounds. Consequently, computations are currently employed to engineer novel materials possessing certain characteristics.

In MO computations, molecular orbitals are simplified as a combination of atomic orbitals in a linear manner. To accurately depict the collective electronic wavefunction and charge density of the system, certain techniques are required to describe the electron-electron interaction effects inside the system. The selection of a suitable method depends on the unique requirements of the calculation, such as the Hartree-Fock approximation, Generalized Gradient Approximation (GGA), or Local Density Approximation (LDA). While the precision of these methods may differ, they all offer a substantial number of basic functions necessary for the computations.

Ab initio approaches are subject to restrictions. One such limitation is the current computational capacity, which can only handle a limited number of atoms. Additionally, it is not feasible to accurately calculate all the properties of real materials. One efficient method is to employ periodic boundary conditions to enhance computing efficiency; however, this does not really augment the

number of atoms encompassed in the system. Hence, methods like the tight-binding method or classical molecular dynamics play a vital role in addressing the intricacies of certain materials. In these two methods and the aforementioned ab initio molecular dynamics, the state of the system is solely defined by the starting condition. Another approach to treating complicated systems is the Monte Carlo method, although further details will not be provided in this context.

Material computation fundamentally entails solving the many-body problem. In solid-state physics, the term “many-body problem” assumes that materials are composed of an infinite number of atoms, referred to as “bulk.” Because this many-body (almost infinite) system possesses a high degree of symmetry, namely the invariance under translation of the unit cell, powerful theorems such as Bloch’s theorem can be used to solve it. In this context, material modeling employs linearization, or linear approximations. The Newtonian equation is a linear approximation of the relativistic equation of motion at speeds much smaller than the light velocity. The linear approximation is suitable for complex systems because the potential around the stable position can be expressed by a quadratic equation. Nonetheless, it is also important to study situations outside of the linearity range. In general, numerical treatment is the only way to solve many body problems. This scheme is extended to the basic equation in molecular dynamics. The material properties studied in computational science for molecules, crystals, and polymers are determined by the fundamental forces (ionic, covalent, molecular, and van der Waals forces) between their constituents. Therefore, determining material properties strongly depends on the establishment of interaction potentials or on experimental observations.

4.2 COMPUTATIONAL METHODS

The principal idea of “first principles” and “ab initio” is to regard many-atom systems as many-body systems composed of electrons and nuclei, and to treat everything on the basis of first principles of quantum mechanics, without introducing any empirical parameters. When the positions of all nuclei are held fixed in a system, the electrons reach a steady state and form an “electron cloud” with a stable charge density distribution determined quantum mechanically.

Using First-principles (or ab initio) molecular-dynamics methods, which calculate the forces exerted on atoms at each time step, one can simulate the evolution of atomic and electronic motions. In general, electrons move so as to follow very quickly the nuclear motion. This is because the electron mass is much smaller than that of nuclei. In such a case, where the change in the electronic state occurs very rapidly compared to the nuclear motion, the assumption that the electrons are always in a steady state holds generally. This is called the Born–Oppenheimer

(BO) approximation and adiabatic approximation. Using this approximation, one can completely separate the calculation of the electronic structure from that of the ionic motion and perform the two calculations separately at each step. This is the basis of the usual BO/adiabatic ab initio molecular-dynamics methods.

However, to treat rigorously the quantum states of many-electron systems is not easy, and one has to rely on some approximate theories, namely a methodology which is fairly reliable but not exact. In our calculations, we also used some approximate methods with the framework of density functional theory (DFT), which will be introduced in the next section. In the following, atomic units ($e = \hbar = m = 1$) are used unless mentioned otherwise. In atomic units, which we abbreviate to a.u., the length unit is the Bohr radius (0.529×10^{-10} m), and the energy unit is 1 Hartree ($=$ 2 Rydberg $=$ 27.2 eV $=$ 4.36×10^{-18} J).

A. Density Functional Theory

The first-principles approach based on DFT is used to determine the ground state and excited states of many-atom systems. DFT is a theory that expresses energy using electron density [1)]. It offers an exact background for the many-body problem but can be solved only approximately. Instead of solving the complex many-electron Schrödinger equation directly, DFT aims to find the ground-state electronic density of a system that minimizes the total energy. In this case, the resulting equation is one-electron-like. There are quite a few underlying theories in the DFT framework, and we will only present a few that are relevant to our calculations.

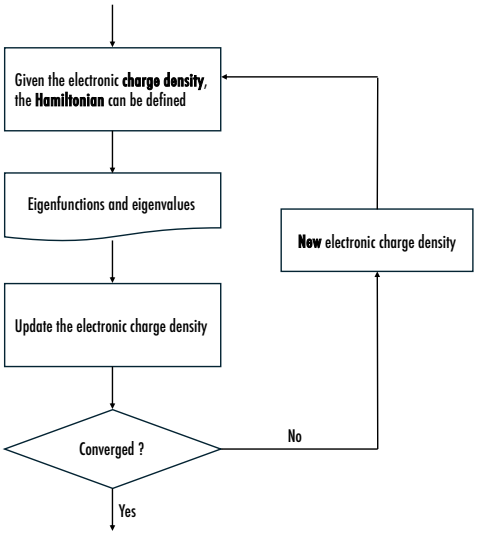

Figure 4.1 The electronic degrees of freedom are treated in the DFT framework.

Hohenberg-Kohn (HK) Theorems

The Hohenberg–Kohn theorems [2] provide a theoretical foundation of DFT. In 1964, Hohenberg and Kohn introduced their theorems for v-representable electron densities, which describe the electronic ground state using the electron density as the primary variable. An electron density is v-representable if it is associated with a ground-state solution to the Schrödinger equation.

- HK theorem I: The external potential $\hat{v}(\mathbf{r})$ of a given system is determined to within a trivial additive constant by the v-representable electron density of the system.

  This allows for the separation of energy into separate the energy functional into two terms

  $$E_0 = E[n_0(\mathbf{r})] = F_{\mathrm{HK}}[n_0(\mathbf{r})] + V[n_0(\mathbf{r})] \tag{4.1}$$

  where

  $$V[n_0(\mathbf{r})] = \int v(\mathbf{r}) n_0(\mathbf{r}) \mathrm{d}^3\mathbf{r} \tag{4.2}$$

  the $n_0(\mathbf{r})$ is the ground state (GS) described in DFT, and the HK functional is introduced as

  $$F_{\mathrm{HK}}[n_0(\mathbf{r})] = T[n_0(\mathbf{r})] + U[n_0(\mathbf{r})] \tag{4.3}$$

- HK theorem II: From the v-representable trial densities $\tilde{n}_0(\mathbf{r})$ fulfilling $\int \tilde{n}_0(\mathbf{r})\mathrm{d}^3\mathbf{r} = N$; $\tilde{n}_0(\mathbf{r}) \geq 0$; and the ground state energy E_0 of a molecular system can be determined from the relation

  $$E_0 \leq E[\widetilde{n_0}(\mathbf{r})] \tag{4.4}$$

Kohn-Sham (KS) Equation

In the Kohn-Sham formulation [3] of DFT, the process of minimizing the energy while ensuring particle conservation closely follows the derivation of the Hartree-Fock equation (a rigorous one-electron approximation). The KS equation is the resultant equation used to determine the best orbitals, which is shown as:

$$\left[-\frac{\hbar}{2m_{\mathrm{e}}}\nabla^2 + v_{\mathrm{eff}}(\mathbf{r})\right]\psi_i(\mathbf{r}) = \varepsilon_i \psi_i(\mathbf{r}) \tag{4.5}$$

where ε_i is the orbital energy of the corresponding KS orbital, and an effective potential is denoted as $v_{\mathrm{eff}}(\mathbf{r})$.

The Kohn-Sham equation describes the behavior of non-interacting “electrons” in an effective local potential. For the exact functional and, thus, exact local potential. The Kohn-Sham equation has the same structure as the Hartree-Fock equations, with the non-local exchange potential replaced by the local exchange-correlation potential. For calculations in which the energy surface is the quantity of primary interest, DFT offers a practical and potentially highly accurate alternative to the wavefunction methods discussed above.

Exchange-Correlation Functional

The accuracy of the Kohn-Sham method is determined by the capability of the exchange-correlation functional to capture the non-classical electron-electron interactions in the molecular (many-atom) system. As the exact form of the exchange-correlation functional is unknown, one introduces physically justified approximations. The exchange-correlation functionals can be classified by various criteria, such as functional parameterization, arguments, etc. There are several types of exchange-correlation functionals, and new functions are constantly being developed. Here, we only introduce Generalized Gradient Approximation (GGA) [4,5].

Functionals of this approximation (GGA) depend on $n(\boldsymbol{r})$ and $\nabla n(\boldsymbol{r})$. By incorporating the electron density gradient, a more precise description of electron-electron interactions in areas of rapidly varying density can be obtained. In the 1970s, Sham and Herman, along with their coworkers, made the first efforts to create this kind of exchange-correlation functionals, but failed from a performance point of view. In 1988, Becke proposed the first reliable exchange functional (B88). Subsequently, more exchange-correlation functionals have been constructed using the Becke formulation. Among these, the most notable are the Lee-Yang-Parr (LYP) correlation functional and the Perdew-Burke-Ernzerhof (PBE) exchange-correlation functional. The former is an integral component of the most widely used hybrid functional (B3LYP), while the PBE functional is the most commonly employed GGA functional in solid-state computations (and also in our calculations).

B. Computational Resource

To complete calculations quickly and accurately, high-performance computers, or supercomputers, are essential. These systems typically feature a large number of processors capable of handling extremely complex computational tasks. High-speed network connections and large-capacity memory facilitate the transfer of data and storage of files between personal computer terminals and the supercomputer system. The DFT method introduced in the previous section requires computational software packages to prepare cell parameters, pseudopotentials, and other input files containing computational parameters. Next, we introduce the computer systems supplied by the Supercomputer Center, the Institute for Solid State Physics (ISSP, The University of Tokyo), and the computational tools used in our calculations.

Supercomputer System

A representative one we used to be the system B, as shown in Figure 4.1, consists of two types of compute servers (CPU servers and FAT servers). The CPU server is a Dell PowerEdge C6525 (1,680 nodes) equipped with two AMD EPYC 7702. And the FAT server is a Dell PowerEdge R940 (8 nodes) equipped with 4 Intel Xeon Platinum 8280 and 3 TB memory.

Each node of these systems is connected by HDR100 InfiniBand. Each node is connected to a Luster file system with a capacity of 600 TB for the user's home directory and 2 PB for the work directory. These file systems are connected by HDR100 InfiniBand, which enables high-speed file access from each node.

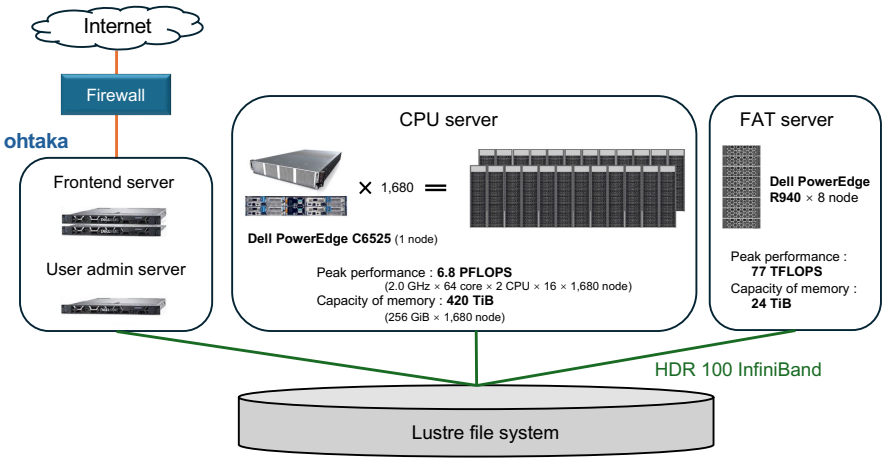

Figure 4.2 Configuration diagram of supercomputer system B in the ISSP [6].

Simulation Tool

In this work, all first-principles calculations based on DFT methods were performed using STATE (Simulation Tool for Atom TEchnology) code [7,8]. STATE is a plane-wave pseudopotential implementation of electronic structure calculations and ab initio molecular dynamics simulations based on DFT within the local, semilocal, and nonlocal density functionals. STATE is written in the fortran90 and parallized with MPI and Open MPI.

The STATE program can accomplish calculations as follows:

- Electronic minimization
- Electronic structure analysis
- Structural optimization
- Reaction path search
- Molecular dynamics
- Free energy sampling
- Real-space projection of nonlocal pseudopotential
- Accurate slab calculation with the effective screening medium (ESM) method

- Electrified slab calculation with the ESM method

Currently, we primarily use structural optimization to validate our computational models, making them closer to real-world structures. Then, we will use electronic structure analysis to obtain the density of states, partial density of states, band structure, and STM simulations of the materials. Additionally, reaction path search and molecular dynamics are considered powerful tools for exploring the etching mechanisms discussed in Chapter 5. Although this thesis does not cover these aspects, we plan to use them in our future work.

Table 4.1 The methods used in our calculations.

Theory of calculation	
Total energy	DFT
Pseudopotential	Ultrasoft
Exchange-correlation functional	PBE-GGA
Wave functions	Plane-wave basis set

In our DFT-based calculations, as shown in Table 4.1, the Perdew-Burke-Ernzerhof generalized-gradient approximation (GGA) was used as the exchange-correlation functional [5]. Ultrasoft pseudopotentials and a plane-wave basis set were used to expand wave functions and charge density with cutoff energies of 36 and 400 Ry, respectively.

C. Computational Process

In our calculations, self-consistent field (SCF) calculations are required, both for simulating STM images, energy band structures, and density of states. This method is a fundamental part of quantum chemistry and computational materials science, especially within the framework of DFT and Hartree-Fock methods. It uses an iterative process to solve the Schrödinger equation for many-atom systems until a satisfactory answer is obtained. The following is the SCF process:

- Initial guess: A guess for the electron density or the wavefunction is given at an initial step to compute the initial potential.
- Solve the Kohn-Sham (or Hartree-Fock) equations: New electron orbitals and eigenvalues are obtained in this step.

- Update electron density: A new electron density is computed using the orbitals in previous step.
- Convergence or iteration: The new electron density is compared to the previous one (a guess). If the difference between them is smaller than a predefined threshold, the calculation is convergent. If not, the SCF calculation continues to generate updated potential.

In this process, the initial guess for the electron density and the criteria for convergence are important. The criterion of convergence determines the accuracy of the computation. An example of our SCF process and the input and output files are given in Figure 4.3.

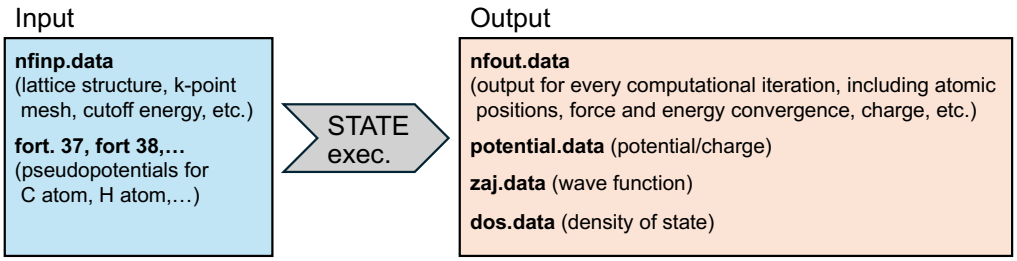

Figure 4.3 Flow of self-consistent field (SCF) process in our calculations.

In cases of convergence, the output files obtained in Figure 4.3, such as the wave function (dos.data) and electron density/potential (potential.data), will be used for subsequent STM image simulations and other calculations. In the STM image simulation, we use armchair-edged graphene nanoribbons or introduce wrinkle structures starting from it. The model's specific calculation details will be explained in the subsequent sections.

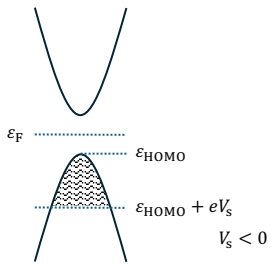

Figure 4.4 Schematic for a negative sample bias (V_s) used in STM image calculations.

Here, it is necessary to introduce the sample voltage used in our calculations, as it is required in all our computations. Additionally, it's important to emphasize certain aspects that can easily lead to misunderstandings, as shown in Figure 4.4. In our calculations, we attempt to understand how the distribution of electrons with high energies influences STM images. In other words, the bias dependence on images was investigated in a small and negative bias region. To avoid inaccuracy in the Fermi level (ε_F), we used the sum of the electron density of orbitals in $[\varepsilon_{HOMO} + eV_s, \varepsilon_{HOMO}]$ for a negative sample bias (V_s), where e denotes the elementary charge ($e > 0$) and ε_{HOMO} denotes the energy level of the highest occupied molecular orbital (HOMO). Computed local density of states (LDOS) contours were obtained for the simulated STM images at the corresponding V_s.

4.3 EFFECT OF RIBBON WIDTH ON SIMULATED STM IMAGE OF AGNR

From this Section up to Section 4.5, calculations will focus on the electronic structure of armchair-edged graphene nanoribbons (AGNRs). The initial motivation for these calculations is to verify the origin of the rectangular lattice observed in the STM experiments discussed in Chapter 3. In other words, this thesis aims to investigate the effects of defects like edge and wrinkle structures on the electronic density and chemical activity of nanographene. The reasons for using AGNR models, as well as why this section starts with changing the ribbon width, can be found in the last section of Chapter 3. Additionally, since the goal is to verify the results of the STM experiments, it is necessary to compare the calculations with the experimental conditions and results presented in the article.

A. Rectangular Lattice in AGNRs with Specific Width

Validation of Calculation Accuracy

In computational studies, it is essential to verify that the computational models and methods used are reasonable and feasible. One way to achieve this is by referencing calculations from other literature. The AGNR model used in our calculations has been extensively studied, so parameters such as its lattice constants are well-documented. Reproducing some of the computational results of other researchers is also necessary and should be implemented at the initial stages.

The schematic of AGNRs we simulated is shown in Figure 4.5a. In this study, the armchair

edges of the ribbons were all treated with single-hydrogen termination, which is one of the most thermodynamically stable structures [9]. Ribbon width (W), also expressed as N in other literature or in Chapter 2 of this thesis, is defined as the number of dimer lines that cross the ribbon width.

Take the AGNR with a width of $W = 22$ as an example; the size of a supercell, indicated as the dashed frame in Figure 4.5a, along the x and y directions is 4.26 and 43.65 Å. And vacuum distances of 15.90 and 10.60 Å separate the ribbons in plane and between planes, respectively. The Brillouin zone integration along the edge direction was done with a uniform grid of 30 k points, unless otherwise stated. The atomic positions in the cell were optimized to relax until all the forces on the nuclear coordinates were below a threshold of 10^{-3} a.u.

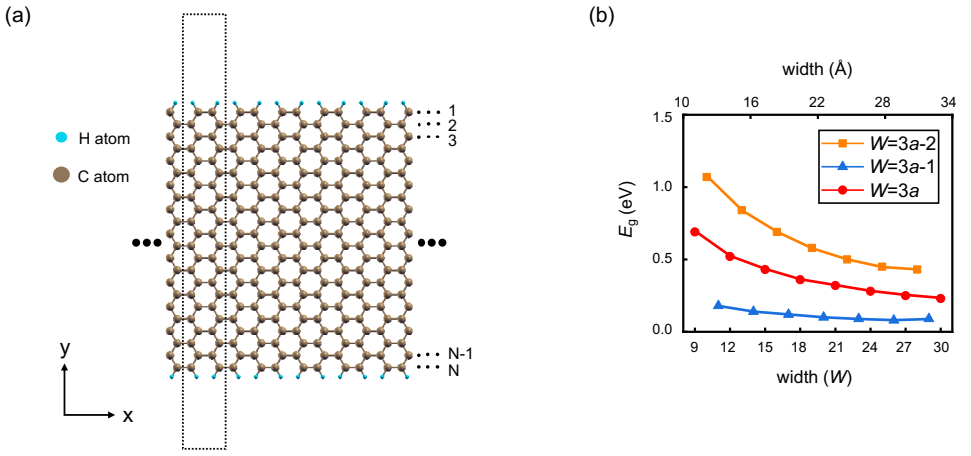

Figure 4.5 (a) Schematic of the AGNR model for simulations. (b) Calculated bandgap (E_g) as a function of AGNR width.

Using the optimized AGNRs, we first checked the validity of our simulations by investigating the energy gaps (E_g) as a function of an AGNR width based on its band structure. As shown in Figure 4.5b, it is clear that the plots can be divided into three subclasses, i.e., $W = 3a - 2$, $3a - 1$, and $3a$ wherein a is an integer. For all subclasses, E_g decreases with increasing ribbon width and tends to zero. The graph in Figure 4.5b indicates that the width and subclass of AGNRs determine whether the system is metallic or semiconducting. This result is very consistent with previous literature [10,11] and is a well-known characteristic of AGNR.

Simulated STM Image for AGNRs with different width

We then simulated STM images at a V_s of −0.05 V for AGNRs with the width ranging from $W = 22$ to $W = 30$, the results were shown in Figure 4.6. Simulated STM images were found to

change periodically as the ribbon width W increased. Figures 4.6a–4.6c summarize the results for AGNRs with $W = 3a - 2$, $3a - 1$, and $3a$, respectively. In Figure 4.6a, the electron density is slightly higher at the armchair edges, and dot patterns form a $(\sqrt{3} \times \sqrt{3})R30°$ superstructure in the interior of the ribbons. In the middle of the ribbons, single cocoonlike spots occupy the vertices of the $\sqrt{3} \times \sqrt{3}$ cell. For nanoribbons with $W = 3a - 1$ in Figure 4.6b, the corrugations at the edge areas are similar to those in Figure 4.6a. A $\sqrt{3} \times \sqrt{3}$ lattice is formed in the entire ribbon, however, the feature of single cocoonlike spots is absent. In contrast, for ribbons with $W = 3a$ in Figure 4.6c, electrons are not localized at edges and a rectangular lattice was visualized.

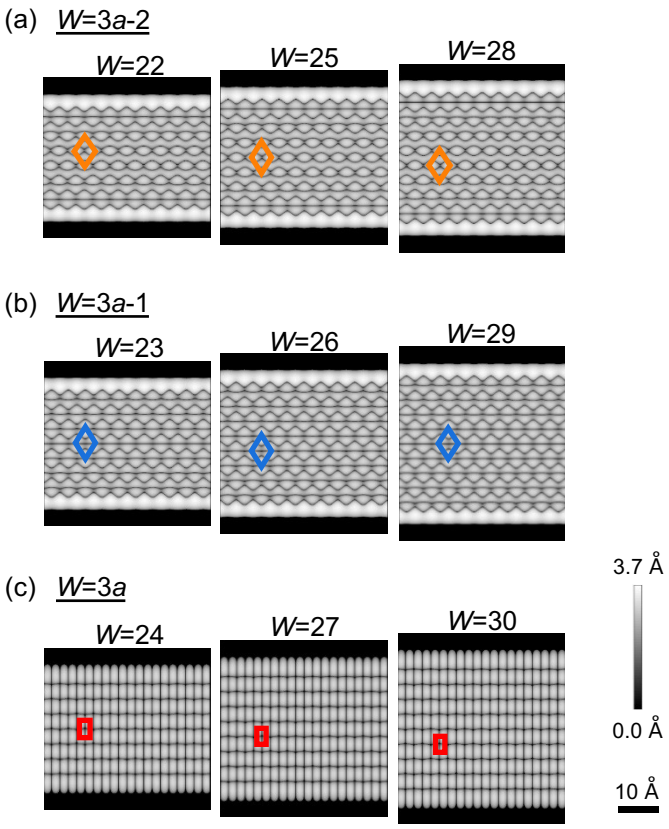

Figure 4.6 Simulated STM images with a unit structure superimposed in each image. (a) AGNRs with $W = 22$ (left), $W = 25$ (middle), and $W = 28$ (right). AGNRs with (b) $W = 23$, $W = 26$, and $W = 29$, and (c) $W = 24$, $W = 27$, and $W = 30$.

Clar's Theory

Before we discuss the details of the distribution and shape of the bright spots, as well as their relationship with the carbon position, the periodically changed STM in Figure 4.6 should be explained. We recall that in such a small V_s region near ε_F, the occupied states of graphene nanoribbons (and graphene itself) belong to the π electrons. Therefore, the STM signal essentially reflects the distribution of π electrons over the carbon network. On the chemical side, Clar's theory qualitatively describes the chemical properties of sp^2-bonded materials [12] very well, including graphene, and it can also be used to explain the electronic states in the crystal lattice. In this theory, six delocalized π electrons form a Clar sextet, representing the resonance of two complementary hexagonal Kekulé configurations with alternating single and double bonds. Here, start with the basics. Figure 4.7a depicts the resonance of electronic structures in benzene. For a given material, the representation with the maximum number of Clar sextets is called the *Clar formula*. If the maximum number of Clar sextets is n, then a Clar bond configuration has the resonance of 2^n Kekulé-type bond formulas [13]. By taking account of all possible Kekulé-type bond formulas, we can best predict various properties of sp^2-bonded materials, ranging from the local density of π states to bond lengths [14,15]. Thus, maximizing the number of Clar sextets unifies a maximum number of resonant Kekulé formulas in one single Clar representation.

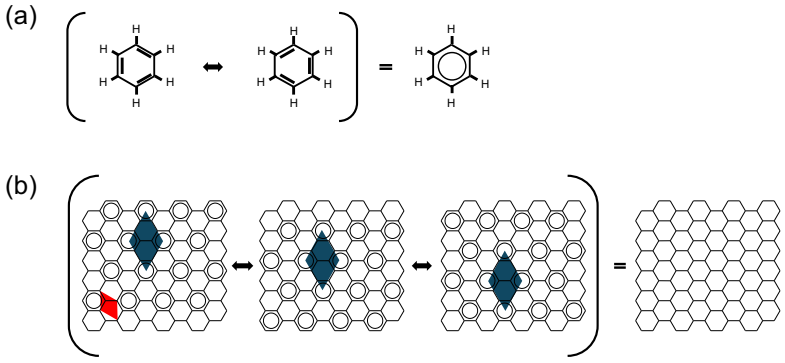

Figure 4.7 Resonance of electronic structures in (a) benzene and (b) an infinite graphene sheet, wherein the unit cells of graphene and the Clar sextets are indicated in red (a) and blue ($\sqrt{3}a$), respectively.

As shown in Figure 4.7b, an infinite 2D graphene sheet has three equivalent Clar formulas. In these formulas, all π electrons belong to a Clar sextet and the bonds sticking out of a Clar sextet are single bonds without any localized double bonds. As a result, the pattern of Clar sextets forms a $(\sqrt{3} \times \sqrt{3})R30°$ superstructure in each Clar formula. The superposition of these three equivalent

Clar formulas in the left panel leads to a uniform π-electron distribution over the hexagonal carbon lattice, as illustrated in the right panel of Figure 4.7b.

In the case of graphene nanoribbons, the uniform π-electron distribution of graphene can be disrupted due to edges. Even if we confine our focus on single-hydrogenated armchair edges, π electrons are not allowed to form only Clar sextets but instead form a mixture of Clar sextets and localized double bonds in some ribbons, depending on ribbon width (Figure 4.8).

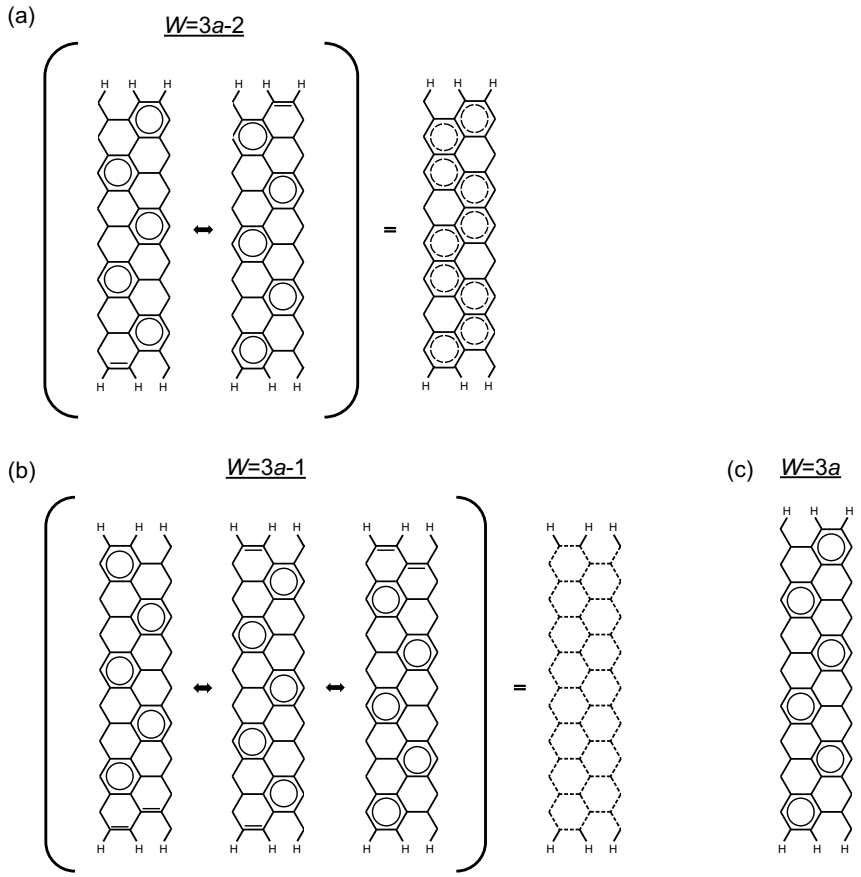

Figure 4.8 Clar formulas for three subclasses of AGNRs with width indices of (a) $W = 3a - 2$, (b) $W = 3a - 1$, and (c) $W = 3a$.

Based on the reference 16, our AGNR can be divided into three subclasses according to the number of different equivalent Clar formulas. The simplest case is AGNR with $W = 3a$, which has only one unique Clar representation with a maximal number of Clar sextets for its unit cell. The next case is AGNR with $W = 3a - 2$, in which there exist two equivalent Clar formulas. Finally, AGNR with $W = 3a - 1$, have multiple, or more than two, Clar representations

maximizing the number of Clar sextets. In the latter two cases, the electronic structure of each AGNR is determined by the coexistence of all possible Clar formulas. Figure 4.9 depicts the periodic change of the superposition of Clar formulas and explains why simulated STM images change periodically with every three increases of W in Figure 4.6. The rectangular lattice in nanoribbons with $W = 3a$ in Figure 4.6c represents the distribution of π electrons at an energy level close to ε_F in the Clar representation in Figure 4.9c.

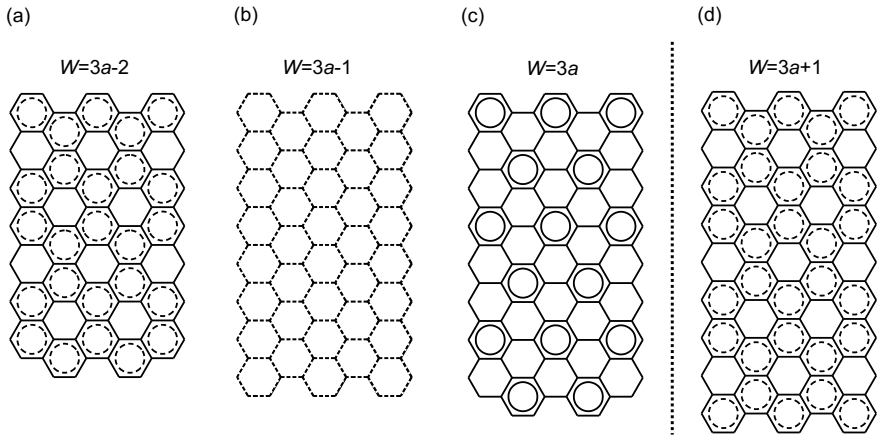

Figure 4.9 Superpositions of all possible Clar formulas for the AGNRs. (a) A ribbon with a width index of $W = 3a - 2$ has two equivalent Clar formulas. (b) A ribbon with a width index of $W = 3a - 1$ has more than two equivalent Clar formulas. The dotted lattice indicates the averaged result of all the possible formulas. (c) A ribbon with the width index of $W = 3a$, which shows one unique Clar formula. (d) A ribbon with a width index of $W = 3a + 1$, which has a Clar formula pattern similar to that in (a).

Figure 4.10a presents simulated STM images of AGNRs belonging to different subclasses. The V_s for these images was assumed to be −0.5 V. Another research group simulated STM images (Figure 4.10b, from Ref. 16) at the same V_s for AGNRs with the same ribbon widths as those in Figure 4.10a. By comparing these images, we can check the accuracy and validity of our simulations. It should be noted that the definition of a ribbon width in Ref. 16 is different from ours. Namely, it defined the width (w) as the number of hexagons across the ribbon width, which yields the relationship $W = w + 2$. If we take this into account, our images in Figure 4.10a are in good agreement with those reported in Ref. 16. Another point to mention is that a rectangular lattice is absent for the $W = 24$ AGNR in Figure 4.10a and 4.10b. This is in contrast to the case

of the AGNR with $W = 3a$ at a V_s of −0.05 V in Figure 4.6c, indicating that V_s is a critical parameter for visualization of the rectangular pattern.

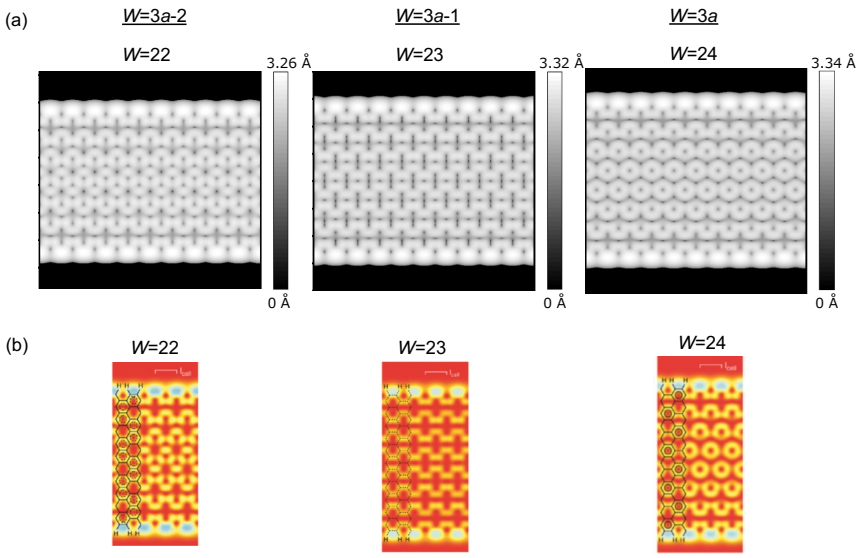

Figure 4.10 Comparison of (a) our simulated STM images and (b) the results in Ref. 16. AGNRs with ribbon widths $W = 22$ (left), $W = 23$ (middle), and $W = 24$ (right) in both (a) and (b). And the same V_s of −0.5 V is used for all images [16].

B. Comparison with Experimental Data

Dot Patterns of Rectangular Lattice

We now look more carefully into the dot patterns of the rectangular lattice. Figure 4.11a is modified from Figure 4.6c with a partial superimposition of Clar formula. The simulated corrugation in the area surrounded by the solid line is enlarged in Figure 4.11b. The atomic coordinate of the highest points reveal that the four vertices do not form a perfect rectangle but form a trapezoid lattice, as shown in Figure 4.11b. This means that not all four vertices are equivalent sites, i.e., this rectangularlike lattice in Figure 4.11b can be interpreted as the overlapping of two different $\sqrt{3} \times \sqrt{3}$ phases as shown by the orange and purple rhombuses in Figure 4.11a. However, the difference in length between the upper (2.05 Å) and lower (2.22 Å) bases in Figure 4.11b is very small. Such a subtle difference may be difficult to distinguish clearly in STM experiments. Therefore, the rectangular lattices in the hexagonal graphene network were

imaged.

The superimposed Clar representation in Figure 4.11c indicates that the two horizontal bonds in a Clar sextet and the bonds sticking out of the sextet both appear dark. In contrast, side areas in a Clar sextet including oblique bonds appear bright (red), reflecting the high local density of occupied π states. In each bright (red) area, the highest corrugation is not at the position of a carbon atom but is situated slightly inside a Clar sextet. As presented in Figure 4.11b, this explains the appearance of the rectangular lattice in STM experiments. As shown in Figure 4.10, a simulated STM image at a higher sample bias, or a negative bias with a larger absolute value than that in Figure 4.6, did not show this rectangular lattice. Consequently, electrons at high energy levels in the occupied states likely contribute to its imaging, some candidates of which are at the HOMO orbital and in the first HOMO band. These details will be discussed in Section 4.4. In addition, it should be noted that the high-corrugation area or the red area forming the vertex of a rectangular lattice exhibits an oval shape rather than a circular shape in Figure 4.11c. This feature also agrees well with Figure 3.24 in Chapter 3, in which each bright dot is elongated along the long-side direction of the rectangle.

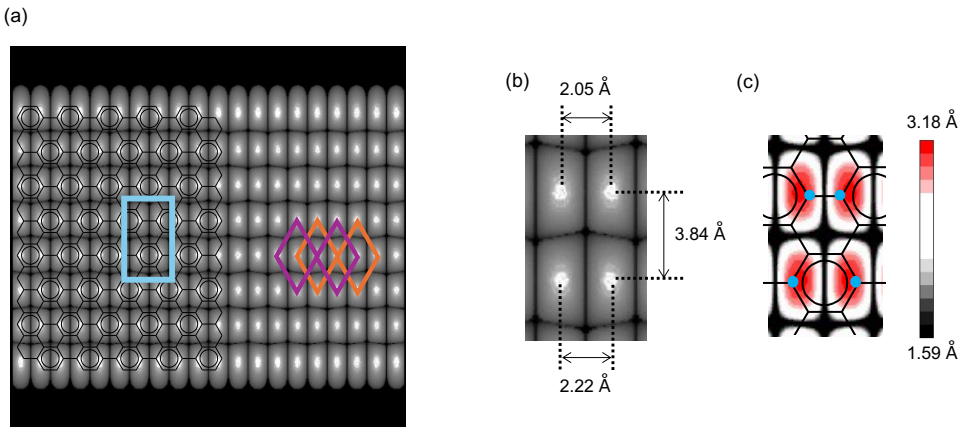

Figure 4.11 (a) Simulated STM image of an AGNR with width index $W = 24$ at a sample bias of −0.05 V. The Clar representation is partially superimposed. Orange and purple rhombuses indicate the overlapping of two different $\sqrt{3} \times \sqrt{3}$ phases. (b) Simulated image of the area indicated by the solid line-box in (a). The distances between the bright spots are indicated with arrows. In (a) and (b), a nonlinear gray scale is used to highlight the highest sites at each vertex of the quadrangle lattice. (c) The area in (b) is depicted using a linear colored scale with the corresponding Clar formula. Filled (blue) circles represent the positions of the nearest carbon atoms from the sites with high density of states. These carbon atoms form a trapezoid whereas the

four red ovals are the vertices of the rectangularlike lattice.

Wrinkle Structure in Graphene Nanosheet

We have shown that two armchair edges belonging to AGNR with $W = 3a$ create the unique rectangularlike pattern of electronic structures near ε_F, which resembles those observed experimentally in Figures 3.23 and 3.24. However, a further point to discuss is the reason why our STM images exhibited a rectangular lattice on the small graphene sheet that is not a simple nanoribbon with perfect armchair edges. Three areas in Figure 3.24 were extracted to investigate further, shown in Figure 4.12a.

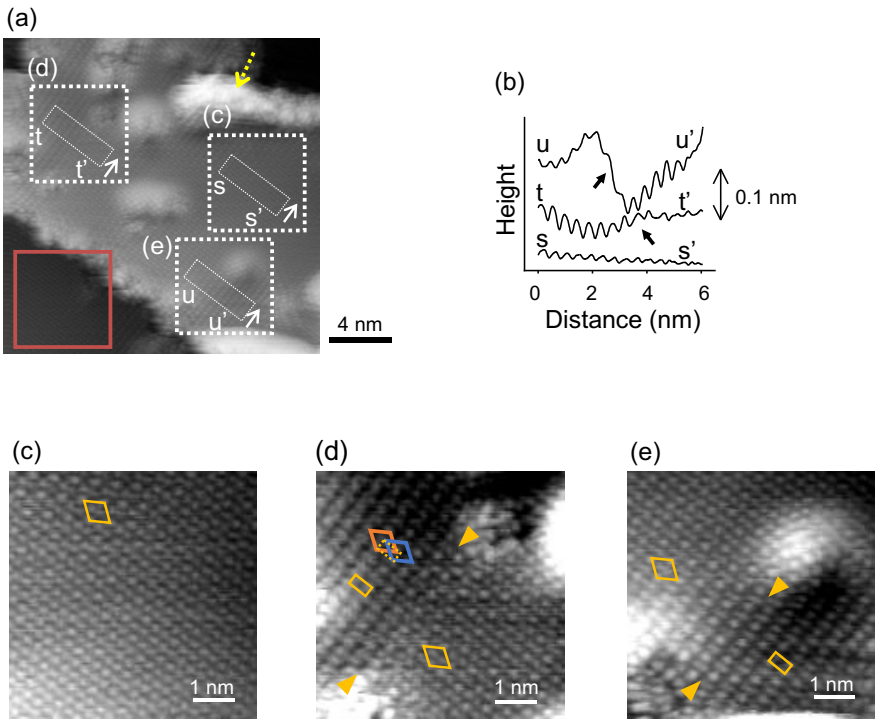

Figure 4.12 Analysis of wrinkling of the graphene sheet. (a) Image from Figure 3.24d in Chapter 3, in which the dotted arrow indicates the same position. Squares represent four selected areas. (b) Cross-sectional profiles along s–s', t–t', and u–u' lines in (a). Each profile is an average of the areas indicated by the dashed lines. The profiles are shifted vertically to avoid mixing. In the t–t' and u–u' lines, there exist height changes, as indicated by arrows. (c)–(e) Enlarged images of the three regions in (a) with enhanced contrast. (c) A relatively flat area with a $\sqrt{3} \times \sqrt{3}$ phase. (d), (e) Regions with a rectangular phase neighboring a $\sqrt{3} \times \sqrt{3}$ area. The approximate position of its

boundary in the middle of each image is indicated by filled triangles.

Figure 4.12b summarizes average cross-sectional profiles in the rectangular dashed areas shown in Figure 4.12a, projected in the direction of the arrows. The three areas in Figure 4.12a are enlarged in Figures 4.12c–4.12e. In Figure 4.12c, the flat area consists of a rhombus lattice, or a $\sqrt{3} \times \sqrt{3}$ phase, as indicated by the superimposed unit cell. In Figures 4.12d and 4.12e, an area with rectangular lattices is beside the $\sqrt{3} \times \sqrt{3}$ phase and the boundary is likely to be situated between the two triangular markers in each image. According to Figure 4.12b, height differences of ~0.02 nm and >0.1nm exist across the boundaries in Figures 4.12d and 4.12e, respectively. A likely explanation of this height difference is the wrinkling of the graphene sheet. We believe that the area with rectangular lattices is partitioned by two boundaries along the direction perpendicular to the long side of the rectangle. As explained above, one boundary is the wrinkling of the sheet in both Figures 4.12d and 4.12e. Regarding the other boundary of the area with the rectangular lattices in Figure 4.12d, there exists an outer edge of the sheet in the upper-left direction on the outside of Figure 4.12d, as indicated by the orange arrow in Figure 3.24a (in Chapter 3). And a ridgelike protrusion in the lower area outside of Figure 4.12e is marked by the green arrow in Figure 3.24a. The height of this protrusion, which may be an adsorbate, was approximately 0.7 nm. Unfortunately, the atomic-scale structures of these defects (the outer edge and the ridgelike structure) were unclear. However, they likely act as the other boundary of the areas with rectangular lattices.

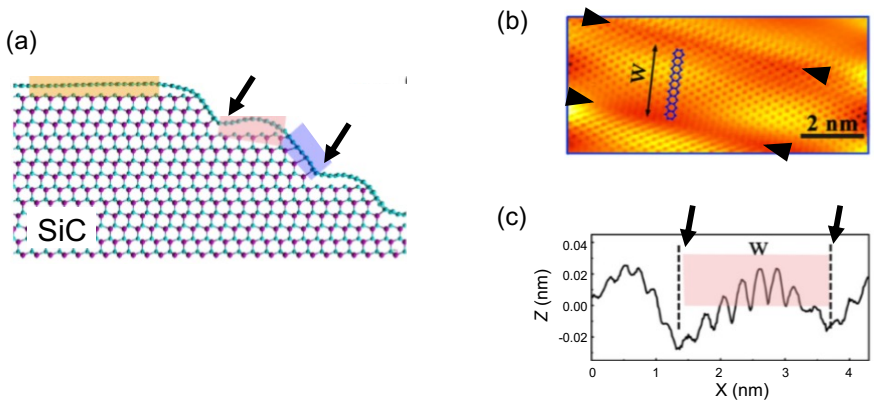

Figure 4.13 (a) Schematic of graphene monolayer on C-face terraces of SiC surface. (b) A STM image of an AGNR on a SiC surface. The atomic structure of graphene is overlaid onto the STM image to determine the ribbon width. (c) A profile line across the AGNR width [11)].

Since first recognized in the 1980s, the $(\sqrt{3} \times \sqrt{3})R30°$ phase has appeared not only near a step edge but also near a localized defect or adsorbed molecules on a graphite surface [17,18]. More recently, Wang et al. demonstrated AGNRs with atomically well-defined widths in a large graphene sheet on a C-faced SiC surface, as shown in Figure 4.13. Their AGNRs on nanoterraces were partitioned by pinning regions on the sidewall of the SiC substrate [11]. In the pinning regions, carbon atoms in graphene strongly bind to the exposed Si atoms. They suggest a "chemical cutting" enabled realization of AGNRs in one large graphene sheet. Considering these studies, it seems reasonable that wrinkling and adsorbates in our folded graphene play a similar role as an armchair edge to generate the $(\sqrt{3} \times \sqrt{3})R30°$ superstructure. When the separation of these defects is at the nanometer scale, two different $\sqrt{3} \times \sqrt{3}$ phases from them overlap to cause the π-electron distribution, as shown in Figure 4.11. This is an imaging mechanism of the rectangular lattices obtained using STM experiments. The overlap of two $\sqrt{3} \times \sqrt{3}$ phases is schematically depicted as orange and blue rhombuses in Figure 4.12d as well. Further investigation on the influence of local defects in graphene sheets on the formation of Clar formulas is required. However, the density of wrinkling can be considered higher on a folded or dispersed graphene sheet than on a natural HOPG surface. This may be one of the reasons why the rectangular phase was easily observed on our graphene sheets in the STM experiments (in Chapter 3).

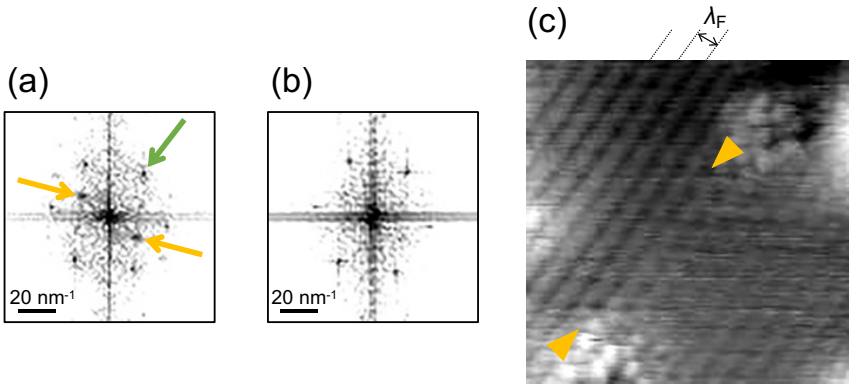

Figure 4.14 (a) Two-dimensional fast Fourier transform (2D-FFT) of Fig. 7(d). The green and yellow arrows represent the carbon lattice and k points of the first Brillouin zone, respectively. (b) 2D-FFT image of the area indicated by the square with a solid line in Fig. 7(a). (c) Inverse FFT of (a) masking points from the carbon lattice.

In previous paragraphs about Clar's theory, we discussed the origin of the rectangular lattice based on the resonance or valence-bond theory. Next, we examine it from a different aspect in the scattering of electron waves; we use the STM image in Figure 4.12d, and Figure 4.14a is its Fourier transform. The outer six points in Figure 4.14a correspond to the carbon lattice. An example of this is indicated by a green arrow. It also shows two intense points indicated by yellow arrows. They are two of the six possible k points of the first Brillouin zone, indicating the generation of intervalley backscattering [19] processes (i.e., coupling between states at two opposite K points (K and K')). We confirm that the two inner points were weak on the HOPG substrate, as shown in Figure 4.14b. This means that the incident K (K') and reflected K' (K) states cause interference of electron waves, thus resulting in a standing wave state [20] with $(\sqrt{3} \times \sqrt{3})R30°$ periodicities [21] in Figure 4.12d. Figure 4.14c shows the inverse fast Fourier transform (FFT) when the outer six points from the carbon lattice in Figure 4.14a are masked. It shows an interference pattern resulting from the two k points indicated by the yellow arrows in Figure 4.14a. This pattern has a periodicity of wavelength (λ_F) of $3a/2$ [21], where $a = 2.46$ Å. The FFT map in Figure 4.14a is similar to that on a graphene monolayer with irregular armchair edges on SiC [22], suggesting that a wrinkle indicated by the triangles in Figure 4.14c behaves like an armchair edge to cause intervalley backscattering and interference of electron waves.

We observed in Figure 4.14c that the upper-left area comprising the rectangularlike lattices has a clearer interference pattern or a stronger standing wave than that in the lower-right area with only the $\sqrt{3} \times \sqrt{3}$ phase. This is because the upper-left area in Figure 4.14c is partitioned by two boundaries, as mentioned in the previous paragraphs. One is the wrinkle in Figure 4.14c, and the other is a graphene edge indicated by the orange arrow in Figure 3.24a. Generated standing waves from the two boundaries, both having a periodicity of λ_F, coexist in the confined area. This leads to the overlapping of two different $\sqrt{3} \times \sqrt{3}$ phases, forming a rectangular lattice, as shown in Figures 4.11 and 4.12d.

C. Summary

So far, this Section has made a number of comparisons with the experimental part of Chapter 3, which also achieves a certain degree of reproducibility. Next, these findings and discussions were summarized.

Graphite surfaces have been widely used as samples for STM since its invention approximately 40 years ago. We conducted STM observations of graphene nanosheets on graphite and found a unique rectangular superstructure. Atomic-scale analysis of the images provided insight into the origin of this unique quadrangle lattice, which is an overlap of $\sqrt{3} \times \sqrt{3}$ superstructures along its

long diagonals. This was examined by first-principles calculations using a simple model or AGNRs. Based on Clar's theory, it is widely accepted that the electronic structures of AGNRs can be categorized into three subclasses. We found that, with a specific width ($W = 3a$) among the subclasses, the distribution of electrons with high energy in the occupied band exhibited a rectangularlike lattice in simulated STM images. The shape and distribution of bright dots forming the lattices were consistent with those observed experimentally. From these results, we proposed that (1) wrinkles and other local defects, such as an adsorbate in the graphene sheet, play a similar role as the armchair edge and induce electron wave scattering to form $(\sqrt{3} \times \sqrt{3})R30°$ superstructures; (2) when these local defects are in close proximity, the region between the defects shows almost the same electronic structures as AGNRs and a rectangular lattice was formed in our small graphene sheet.

Some Additional Calculations

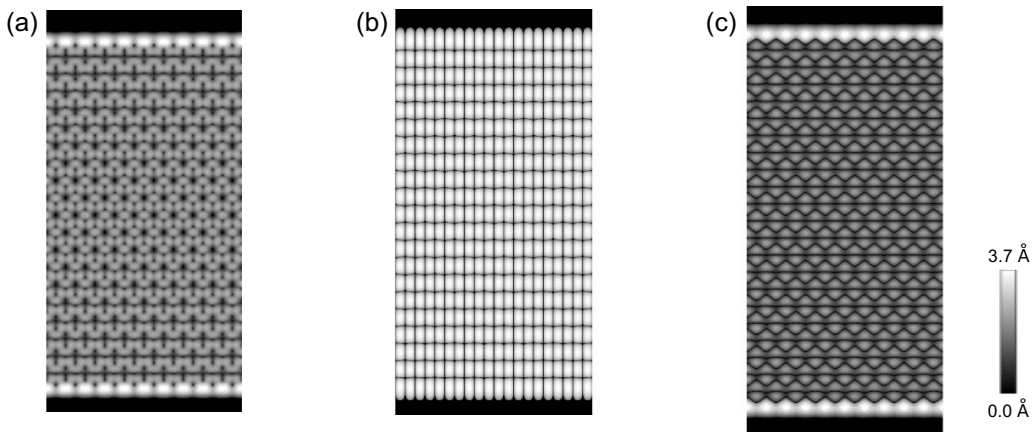

Figure 4.15 Simulated STM images of wider AGNRs with (a) $W = 61$, $W = 63$, and $W = 65$.

Although we calculated nine consecutive AGNRs in Figure 4.6, their width range is narrow. In other words, their widths are approximately between 1 nm and 3 nm, making them narrow ribbons. We aim to investigate whether the rectangular structure present in the $W = 3a$ nanoribbon can also appear in wider nanoribbons. This will also verify the extent to which the armchair edges can influence the electronic states within the AGNR. In Figure 4.15, we calculated wider nanoribbons (about 8 nm in width) belonging to three different subclasses. Their simulated STM images maintain the situation in Figure 4.6. So far, this calculation result remains consistent with the experiment, i.e., the superstructure can still be observed several nanometers away from the

armchair edges within the graphene [23]. We also calculated AGNRs wider than those in Figure 4.15, but the increase in the number of atoms in the calculation model increased the computational difficulty, so we did not make extensive attempts.

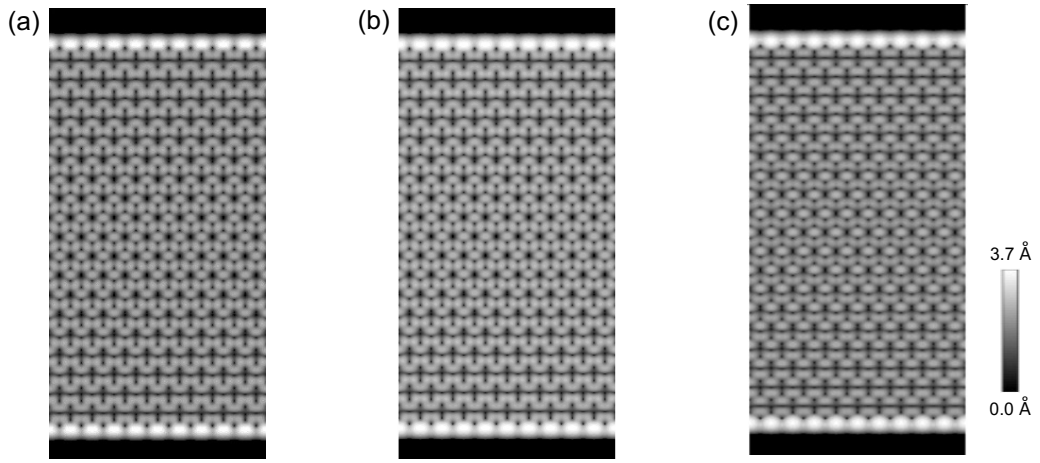

Figure 4.16 Simulated STM images of AGNRs with $W = 61$ using a k-point sampling of (a) 10 k points, (b) 45 k points, and (c) 100 k points along the armchair edge direction.

In Figure 4.16, we also varied the k-point sampling used in our calculations. Since the images in Figure 4.16 did not change their correspondence with ribbon width, we conclude that 30 k points are sufficient for simulating the STM images of AGNRs in this section. Besides the supplementary results in Figures 4.15 and 4.16, we also simulated the STM images of single-layer (and double-layer) zigzag-edged nanoribbons. However, such attempts did not yield effective or complete results and thus are not presented here. Another important suggestion is that comparing and referencing other well-known computational results is very helpful for our own explorations.

4.4 EFFECT OF SAMPLE BIAS ON SIMULATED STM IMAGE OF AGNR

The previous Section still has some issues that were not addressed or explored in depth. For example, in the calculations with small sample bias (Figure 4.6), a rectangular lattice can be

obtained in STM images, while in the calculations with large sample bias (Figure 4.10), it cannot. Clearly, this gap is worth filling, and it is quite easy to achieve in our calculations (by changing the sample bias). It is essential to pay attention to detailed comparisons and analyses.

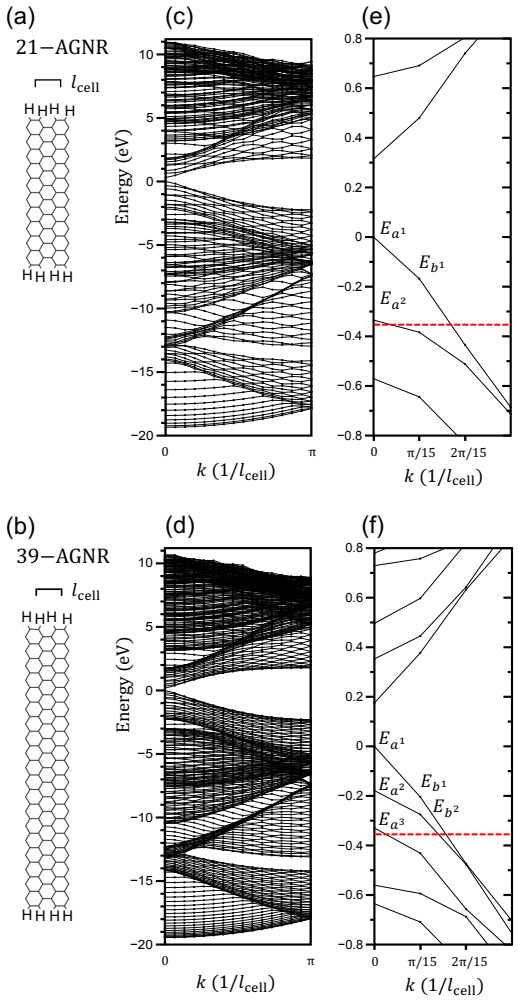

Figure 4.17 Ribbon configurations and band structures of 21-AGNR and 39-AGNR. Note that only the σ-bond network between carbon atoms is depicted in (a) and (b). The band structures of 21-AGNR and 39-AGNR are plotted in (c) and (d). The bands close to $\varepsilon_{\mathrm{HOMO}}$ are depicted in (e) and (f). Eigenvalues at $k = 0$ and its neighbor ($k = \frac{\pi}{15}/l_{\mathrm{cell}}$) are denoted by $E_{a^{\mathrm{n}}}$ and $E_{b^{\mathrm{n}}}$. Zero of energy is set to $\varepsilon_{\mathrm{HOMO}}$.

The type of AGNRs used in this Section remains unchanged from the previous section. For specific details, please refer to Figure 4.5. Figures 4.17a and 4.17b show schematic drawings of AGNRs with $W = 21$ and 39. Periodic boundary conditions were applied to a supercell setup

with a length l_{cell}, as indicated by the bar above each schematic drawing. According to the ribbon width, both belong to the $W = 3a$ family (a represents an integer). In other words, both have only one unique Clar representation with a maximal number of Clar sextets for their unit cell [16]. We refer to AGNRs with a width index W of 21 as 21-AGNR, and the same rule applies to AGNRs with other widths.

Figure 4.17 depicts the ribbon configurations and band structures of 21-AGNR (Figures 4.17a, 4.17c, and 4.17e) and 39-AGNR (Figures 4.17b, 4.17d, and 4.17f). In addition to 21-AGNR and 39-AGNR, we calculated the band structures of AGNRs belonging to other families. The trend of the energy gaps (E_{g}) is in accordance with results in Figure 4.5b. Magnified band structures near $\varepsilon_{\mathrm{HOMO}}$ for these two ribbons are depicted in Figures 4.17e and 4.17f. For 21-AGNR shown in Figure 4.17e, we notice an energy gap of 0.32 eV separating the valence and conduction bands. With the width index increasing to 39, Figure 4.17f shows E_{g} shrinking to 0.17 eV. The red dotted lines indicate the energy of −0.35 eV, corresponding to V_{s} of −0.35 V. Three and five eigenvalues lie within 0.35 eV beneath the $\varepsilon_{\mathrm{HOMO}}$ for 21-AGNR and 39-AGNR. Here, eigenvalues at $k = 0$ are represented as $E_{a^{\mathrm{n}}}$, where a higher n indicates an eigenvalue at a lower energy level below the HOMO. Similarly, those at its neighbor $k = \frac{\pi}{15}/l_{\mathrm{cell}}$ are defined as $E_{b^{\mathrm{n}}}$.

In the previous Section, we compared the experimental data of graphene nanosheets with simulated STM images at V_{s} (−0.05 V). In this Section, we systematically investigate the effect of V_{s} near the ε_{F} on simulated STM images. The V_{s} values are listed in Table 4.2. At each V_{s}, the number of eigenvalues ($E_{a^{\mathrm{n}}}$ and $E_{b^{\mathrm{n}}}$ in Figure 4.17) involved in simulating STM images for 39-AGNR is at least equal to or even larger than that for 21-AGNR. That is because 39-AGNR has more atoms than 21-AGNR, resulting in more discrete energy values. For all V_{s} in Table 4.2, we computed STM images to assess the impact of V_{s} on the images.

Table 4.2 Eigenvalues involved in computing STM images at different sample biases (V_{s}).

V_{s}	−0.05 V	−0.19 V	−0.24 V	−0.29 V	−0.35 V
21-AGNR	E_{a^1}	E_{a^1} E_{b^1}	E_{a^1} E_{b^1}	E_{a^1} E_{b^1}	E_{a^1} E_{b^1} E_{a^2}
39-AGNR	E_{a^1}	E_{a^1} E_{a^2}	E_{a^1} E_{a^2} E_{b^1}	E_{a^1} E_{a^2} E_{b^1} E_{b^2}	E_{a^1} E_{a^2} E_{b^1} E_{b^2} E_{a^3}

Figure 4.18 depicts the simulated STM images at V_s shown in Table 4.2. At the minimum V_s of −0.05 V, only one eigenvalue (E_{a^1}) was responsible for the electron distribution, as listed in Table 4.2. A rectangular-like pattern runs through the entire 21-AGNR and 39-AGNR widths, which is superimposed in Figures 4.18a and 4.18b. In Chapter 3, this particular lattice was observed in the STM experiments of graphene nanosheets at a low and negative V_s.

For 21-AGNR at V_s of −0.19 V, as shown in Figure 4.18c, the vertices of the rectangular lattice changed dramatically and transformed into a ring-like shape. This change is caused by the participation of E_{b^1} in the simulated image. For 39-AGNR at V_s of −0.19 V, as shown in Figure 4.18d, due to the added eigenvalue of E_{a^2}, which is not E_{b^1} as in the case of 21-AGNR, the STM image looks more like a hexagon near the center of the ribbon. Additionally, Figure 4.18d reveals that the pattern near the edges is different from the hexagonal one at the center whose trend is not obvious for 21-AGNR in Figure 4.18c. This probably originates from the difference in width between these ribbons.

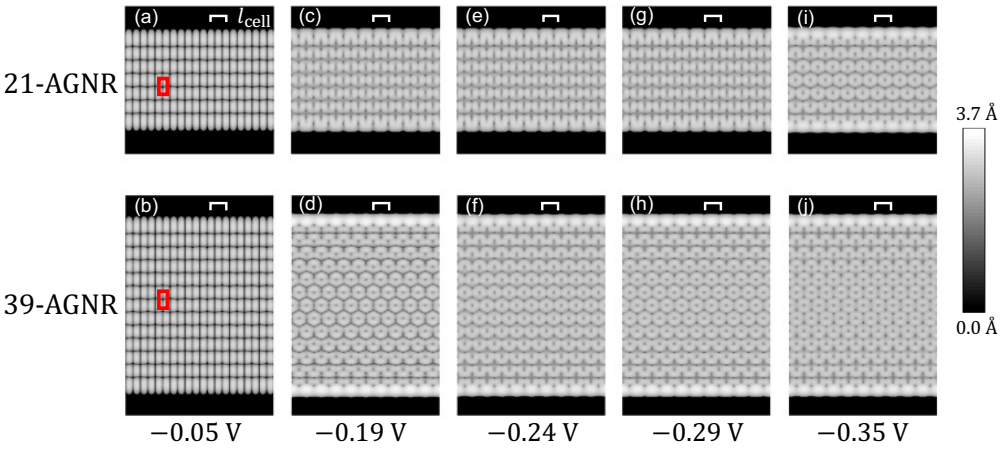

Figure 4.18 STM images were simulated for 21-AGNR and 39-AGNR at V_s listed in Table 4.2.

After V_s was increased up to −0.29 V for 21-AGNR, no new eigenvalues in Table 4.2 were added to compute STM images, resulting in no changes in Figures 4.18c, 4.18e, and 4.18g. For 39-AGNR, new eigenvalues E_{b^1} and E_{b^2} were included when V_s increased from −0.19 to −0.24 V and from −0.24 to −0.29 V. In Figure 4.18f, the corrugation of the hexagon in the ribbon center becomes slightly blurred compared with Figure 4.18d. The simulated STM image in Figure 4.18h is similar to the one in Figure 4.18f, indicating that E_{b^2} has little effect on the formation

of STM images. Figure 4.18i showing 21-AGNR at V_s of –0.35 V resembles Figure 4.18f showing 39-AGNR at V_s of –0.24 V, probably because the same eigenvalues (E_{a^1}, E_{b^1}, and E_{a^2}) contributed to the image formation for both ribbons even at different V_s values. In Figure 4.18j, the addition of E_{a^3} caused a slight change in the image. Namely, the ring-like shapes do not have a demarcation as clear as the ones at V_s of −0.29 V in Figure 4.18h.

A general trend in Figure 4.18 is that eigenvalues with high energies in the occupied states significantly influence computed STM images. The simulated STM images of AGNRs with $W = 3a$ exhibit a unique rectangular-like lattice with E_{a^1} Other eigenvalues with high energies, such as E_{a^2} and E_{b^1}, can affect the simulated STM images to some extent, which depends on how close they are to $\varepsilon_{\mathrm{HOMO}}$.

Although only the eigenvalues at $k = 0$ and 0.033 (or $k = \frac{\pi}{15}/l_{\mathrm{cell}}$) are counted in Figure 4.18, we have considered other k sites to check the simulated STM images in Figure 4.19. Again, as mentioned above, our conclusion is that only eigenvalues with high energies significantly influence our calculations, which remains unchanged even if k-points were increased from 30 up to 100 in Figure 4.19.

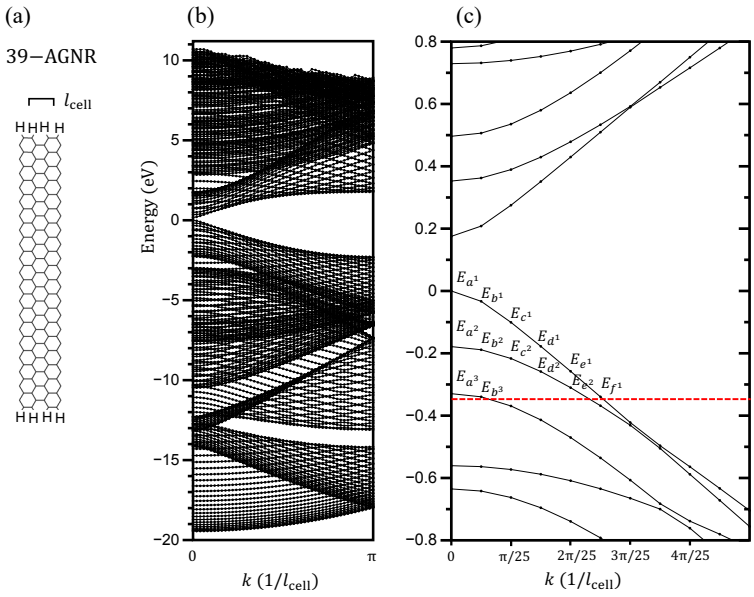

Figure 4.19 Ribbon configuration and its band structures of 39-AGNR. A k-point sampling of 100 k points is used; the red dotted line denotes the energy of −0.35 eV.

In Figure 4.19, we used a k-point sampling of 100 k-points, which is more than 30 k-points in Figure 4.18. The 39-AGNR configuration with single hydrogen termination is depicted in Figure 4.19a. After self-consistent field calculation, the overall band structure and its details at a specific k range are depicted in Figures 4.19b and 4.19c, respectively. Similar to the case of the calculation with a 30 k-point sampling in Figure 4.17, an energy gap of 0.17 eV was shown in the band structures for 39-AGNR in Figures 4.19b and 4.19c. Compared to Figure 4.17, Figure 4.19c shows a larger number of eigenvalues lying within 0.35 eV beneath the energy level of the highest occupied molecular orbital ($\varepsilon_{\mathrm{HOMO}}$). Notably, the eigenvalues in Figure 4.19, such as E_{b^1}, are different from those in Figure 4.17 (except for E_{a^n}, which is at $k = 0$).

Table 4.3 Eigenvalues involved in computing STM images of 39-AGNR at different V_s ranges in (a) and (b).

(a)

V_s	-0.030 V	-0.035 V	-0.105 V	-0.178 V	-0.180 V	-0.190 V
Eigenvalues	E_{a^1}	E_{a^1} E_{b^1}	E_{a^1} E_{b^1} E_{c^1}	E_{a^1} E_{b^1} E_{c^1} E_{d^1}	$E_{a^{1-2}}$ E_{b^1} E_{c^1} E_{d^1}	$E_{a^{1-2}}$ $E_{b^{1-2}}$ E_{c^1} E_{d^1}

(b)

V_s	-0.220 V	-0.258 V	-0.260 V	-0.315 V	-0.330 V	-0.340 V
Eigenvalues	$E_{a^{1-2}}$ $E_{b^{1-2}}$ $E_{c^{1-2}}$ E_{d^1}	$E_{a^{1-2}}$ $E_{b^{1-2}}$ $E_{c^{1-2}}$ E_{d^1} E_{e^1}	$E_{a^{1-2}}$ $E_{b^{1-2}}$ $E_{c^{1-2}}$ $E_{d^{1-2}}$ E_{e^1}	$E_{a^{1-2}}$ $E_{b^{1-2}}$ $E_{c^{1-2}}$ $E_{d^{1-2}}$ $E_{e^{1-2}}$	$E_{a^{1-3}}$ $E_{b^{1-2}}$ $E_{c^{1-2}}$ $E_{d^{1-2}}$ $E_{e^{1-2}}$	$E_{a^{1-3}}$ $E_{b^{1-3}}$ $E_{c^{1-2}}$ $E_{d^{1-2}}$ $E_{e^{1-2}}$ E_{f^1}

Table 4.3 lists a set of V_s, along with the eigenvalues involved between the $\varepsilon_{\mathrm{HOMO}}$ and each V_s. To save space, we use $E_{a^{1-2}}$ to denote E_{a^1} and E_{a^2}, and so on. We simulate STM images of 39-AGNR in Figure 4.20, using V_s listed in Table 4.4. At the minimum V_s of −0.030 V in Figure 4.20a, a rectangular pattern was visible. In Figure 4.20f, we used the same V_s as in Figure 4.18d, −0.190 V, which contributed to the same simulated STM image. Figures 4.20b–4.20e show the V_s between –0.030 V and –0.190 V, containing eigenvalues absent in Figure 4.18. As the V_s value increases in this range, the rectangular structure gradually disappears. When the V_s value exceeded –0.190 V in Figures 4.20g–4.20l, the features of the STM images gradually stabilized

and had a hexagonal structure.

In conclusion, the results in Figure 4.20 are consistent with the calculation in Figure 4.18. The simulated STM image of AGNRs with $W = 3a$ exhibits a unique rectangular lattice with E_{a^1}. Eigenvalues with high energies in the occupied states can significantly influence features in STM images.

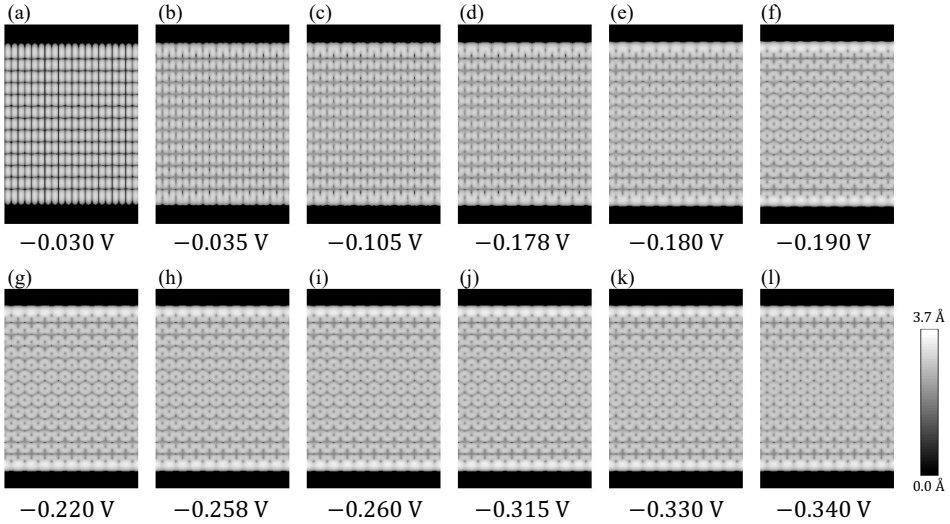

Figure 4.20 STM images were simulated for 39-AGNR at V_s listed in Table 4.4.

We show the simulated STM results of 37-, 38-, and 39-AGNRs belonging to all three families ($W = 3a - 2$, $3a - 1$, and $3a$) in Figure 4.21. For every AGNR in Figure 4.21, as the absolute value of V_s increases, the corrugations representing electron distributions always change. Furthermore, a comparison of AGNRs with different widths at the same V_s is shown in Figure 4.21. At a minimum V_s of −0.05 V, the AGNRs of the three families exhibit different electronic structures. Figures 4.21a and 4.21e show STM images at this low V_s for 37-AGNR and 38-AGNR, which exhibit two different $(\sqrt{3} \times \sqrt{3})R30°$ superstructures. For 39-AGNR shown in Figure 4.21i, the STM image shows an entirely different rectangular lattice; these differences between varied families become less pronounced with increasing V_s, which also indicates that the electrons at the top of the valence band are more capable of changing the electronic structure of AGNRs. Figures 4.21c, 4.21g, and 4.21k show minor variations in STM images for different AGNRs calculated at V_s of −0.5 V, which is inconsistent with previous reports [16,24]. This is probably because AGNRs widths in our study are wider, almost twice as

much as those in previous studies. Figures 4.21d, 4.21h, and 4.21l show results obtained at V_s of −1 V, where more eigenvalues are involved than those in other images in Figure 4.21. Here, Figures 4.21d, 4.21h, and 4.21l show hexagonal patterns, as examples are depicted in red ink. This shows that STM images at large V_s lose the periodic change of dot patterns depending on the category of ribbon width ($W = 3a - 2$, $3a - 1$, and $3a$). They reflect the structure of an in-plane graphene network instead. In addition, bright dot patterns are obtained at the edges among all three images. In summary, obtaining an image at a small negative V_s is effective to distinguish the three families ($W = 3a - 2$, $3a - 1$, and $3a$) of AGNRs in experiments.

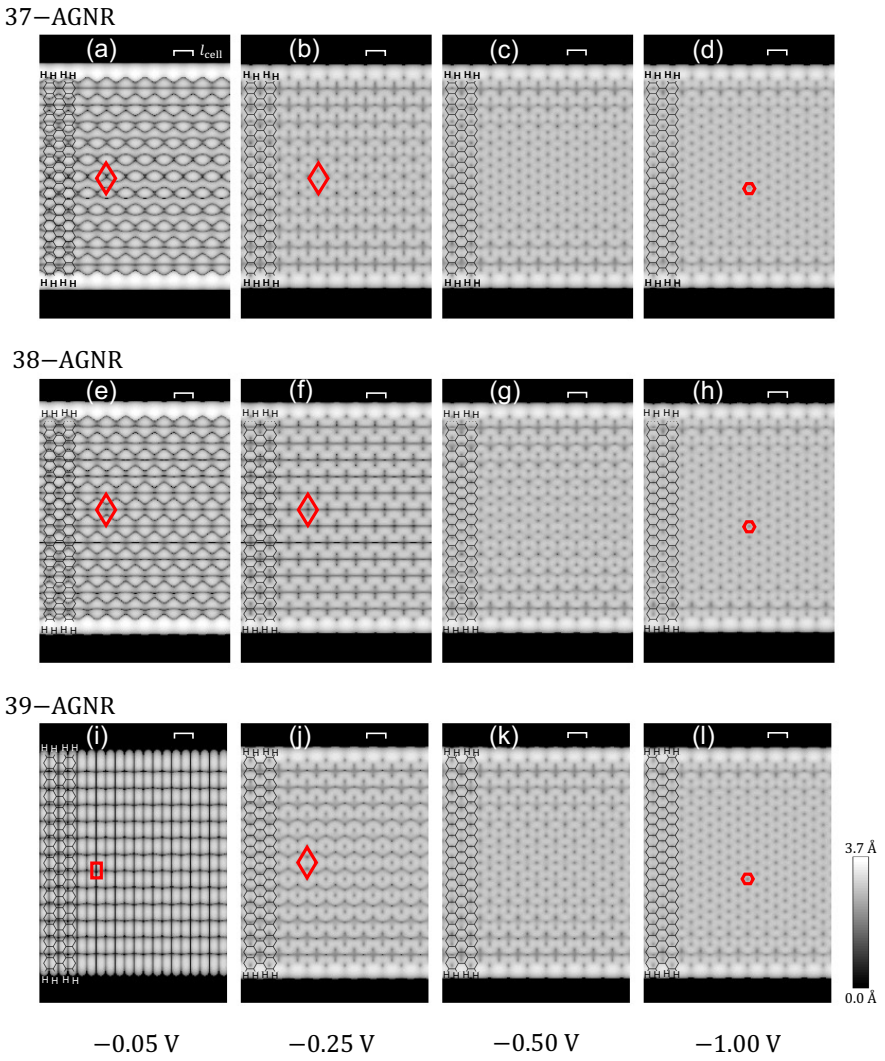

Figure 4.21 Simulated STM images of AGNRs with three different families as 37-AGNR (upper), 38-AGNR (middle), and 39-AGNR (lower). STM images in each column were

calculated using the Vs value below. The ribbon configurations are superimposed in each image.

4.5 EFFECT OF LINEAR WRINKLE DEFECT ON SIMULATED STM IMAGE OF AGNR

A graphene wrinkle was introduced into AGNRs in this Section, which is different from the previous calculations. Wrinkling is a typical defect structure generated in 2D materials on a supporting substrate [25,26]. In this paper, we abbreviate nanowrinkles on graphene, or graphene nanowrinkles, as GNWs. Recent experimental data on graphene sheets with GNWs show some new findings, such as its 1D electron confinement [27,28]. However, little is known about the structural morphology and electronic properties of GNWs due to two main reasons: one is that wrinkles are easily deformed due to external influences, and they will fold over after reaching a maximum of ~6 nm [29]. The other is that measurements are always performed on the substrate; thus, the intrinsic effect of the interaction with a substrate cannot be ignored.

A. Wrinkle Structure

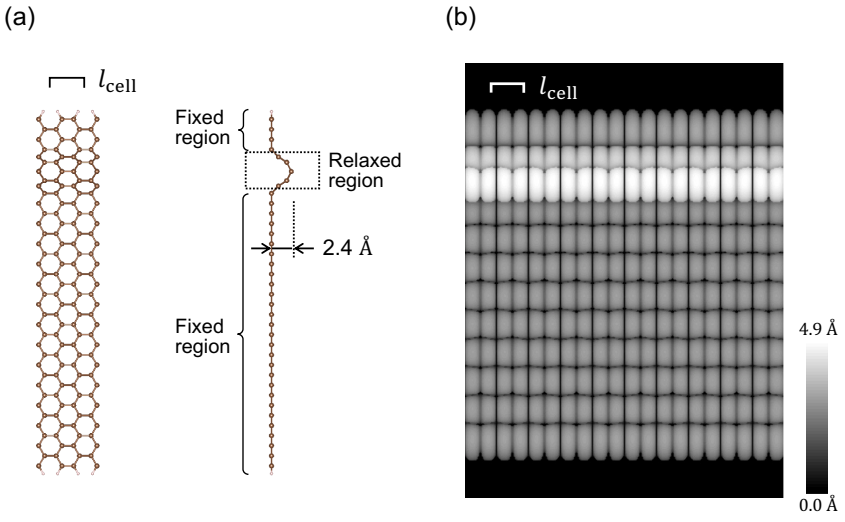

Figure 4.22 37-AGNR with a wrinkle. (a) The ball and stick models; the edges of the ribbon are terminated by hydrogen atoms (small balls). Braces and the dashed box indicate the fixed atoms

and the relaxed atoms, respectively. The wrinkle has a height of 2.4 Å. (b) Simulated image of this AGNR with a V_s of −0.05 V.

To eliminate the effects of a substrate, we investigated the electronic structure of a free-standing AGNR with a wrinkled defect. Using the model shown in Figure 4.22, we examine how a GNW in an AGNR affects STM images at low V_s. The relaxed model of 37-AGNR, with which we simulated the electron density maps in Figures 4.21a–4.21d, was used as the starting material. Note that the C atoms in this simple AGNR are all distributed in the same plane. In the following, x and y axes in-plane were taken parallel and perpendicular to the armchair edge. The z-axis was taken as the direction normal to the plane. To make the 37-AGNR bent in Figure 4.22a, we kept the flat portion in-plane fixed and separately optimized the structure of wrinkled part in Figure 4.22a. The wrinkled structure was allowed to relax down to a force threshold of 10^{-3} a.u. To reproduce the experiments in Figure 4.12, the model in Figure 4.22a has a GNW with a straight ridge with a limited height of 2.4 Å in the z-axis. We emphasize that the linear wrinkle in our model is parallel to the top and bottom edges. The typical height and width of the wrinkle in 37-AGNR are comparable to the measured [27] and calculated [30] values in other studies.

B. Changes in Electronic States near Fermi Level

As illustrated in Figures 4.21a, 4.21e, and 4.21i, only the STM images of AGNRs at low V_s exhibit the periodic change with respect to the three families ($W = 3a - 2$, $3a - 1$, and $3a$). Thus, we calculated the STM image at −0.05 V in Figure 4.22b. In contrast to the rhombus lattices on the simple 37-AGNR shown in Figure 4.21a, rectangular-like lattices similar to those in Figure 4.21i are visible on the AGNR with a wrinkle shown in Figure 4.22b.

In Figure 4.22, we demonstrated that GNW changes the STM image representing the distribution of electrons with high energies in the occupied band. This is probably because the wrinkled structure in Figure 4.22a disturbs the resonance [16] of the electron distributions determined by the ribbon width, which is $W = 3a - 2$ in this case. We also conducted similar calculations to those in Figure 4.22 with wrinkled graphene, where we varied the width, height, and position of the wrinkle. Unfortunately, as these structural parameters are extensive, we have not completed a systematic study on how each parameter of the wrinkle affects the electronic structure on a flat graphene region. It should be noted that what we observe in Figure 4.22 is that a wrinkle parallel to the armchair edges alters the electron distribution on a neighboring flat graphene region, even if the wrinkle's height is only a few angstroms.

In our experimental work [31], rectangular lattices were found on nanographene sheets. We

speculate that the wrinkled structure played the role of an edge, altering the electronic distribution of these nanographene sheets. If two line-defects, such as edges or wrinkles whose ridges are sufficiently high, were parallel and in close proximity, the electronic structure of AGNRs appeared in the region between these line defects, even on graphene sheets that are not perfect ribbons. In Figure 4.22, the rectangular lattices appear in 37-AGNR with a wrinkle, which directly proves the above-mentioned perspectives.

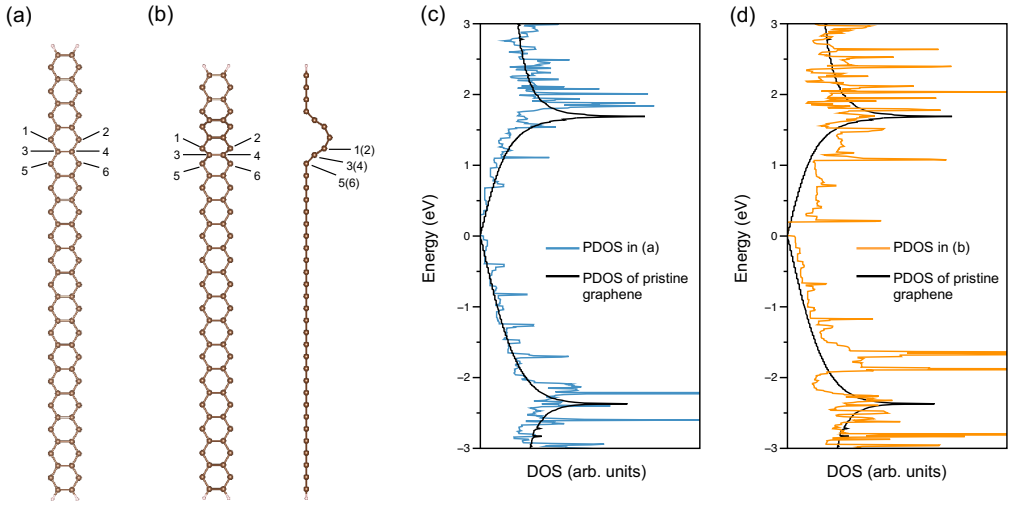

Figure 4.23 PDOS of the simple 37-AGNR and the one with a wrinkled structure. (a) Schematic of simple 37-AGNR. (b) Schematic of wrinkled 37-AGNR. The notation "1(2)" indicates two atoms labeled as 1 and 2 in the left panel, and the same rule applies to 3(4) and 5(6). (c) PDOS of the six-labeled carbon atoms in (a). (d) PDOS of the six labeled carbon atoms in (b). In (c) and (d), the PDOS of six carbon atoms in pristine graphene is also shown as black curves though its computational model is not provided.

Finally, the effect of introduced wrinkles on the density of states (DOS) is worth mentioning, and the calculated results are shown in Figure 4.23. Six C atoms in Figure 4.23a are in the same z plane, whereas the six C atoms in Figure 4.23b are in a wrinkle configuration. The partial density of states (PDOS) of these C atoms are displayed in Figure 4.23c and 4.23d. For the six C atoms in the simple 37-AGNR, the contribution of the PDOS in Figure 4.23c is similar to the PDOS in pristine graphene. In comparison to the PDOS of pristine graphene or the simple 37-AGNR, the PDOS of the wrinkled structure in Figure 4.23b exhibits a significant contribution near 0 eV as shown in Figure 4.23d. A noticeable increase in electron or state density was shown

in the energy ranges of (-2 eV, -1 eV) and (0 eV, 1 eV), along with a small increase in the range of (-1 eV, 0 eV). A high DOS in this energy range has also been proposed on the surface of nitrogen-doped graphene, which causes spontaneous adsorption of gas molecules and paves the way for subsequent chemical reactions [32,33]. Wang et al. demonstrated that morphology regulation could create wrinkles in graphene nanosheets as powerful adsorptive sites and remove organic pollutants [34]. The multi-curved, wrinkled surface of graphene-based materials provides good lithium adsorption sites, resulting in improved lithium storage capability as a working anode [35]. In these reports, wrinkled surface defects improve the chemical activity of graphene, which is thought to be due to the high DOS near 0 eV shown in Figure 4.23d.

4.6 SUMMARY

We performed first-principles calculations within the GGA approximation to obtain the band structures and STM images of AGNRs. The features in simulated STM images of AGNRs are found to be V_s sensitive, and this gives rise to three families of AGNRs based on the calculations of small V_s values. Specifically, at the top of the valence band, eigenvalues have a significant effect on STM images computed at the corresponding V_s. AGNRs with the width index $W = 3a$ exhibit a unique rectangular lattice when only the highest eigenvalue in the occupied states is calculated, which is the minimum V_s in this study. For the AGNRs of all three families, at this small V_s, triple periodicity according to the width is revealed. As the absolute V_s value increases, the STM images of all AGNRs change. When V_s reaches a sufficiently large value such as −1 V, the AGNRs of all three families exhibit the same hexagonal lattice, which is also consistent with previous studies. When a linear wrinkled defect is introduced into AGNRs, it plays a role similar to that of an edge, thereby changing the electronic structure or STM images in AGNRs. For instance, the above-mentioned rectangular lattice appears in 37-AGNR that does not belong to $W = 3a$. An increasing PDOS of the wrinkled structure was also displayed near the ε_F. Our computational method provides an approach for gaining insights into wrinkle defects in graphene. This enables a deeper understanding of the wrinkled structure and a more flexible use of this defect for graphene modification.

REFERENCES

1) W. Kohn, A. D. Becke, R. G. Parr, J. Phys. Chem. 100 (1996) 12974-12980.
2) P. Hohenberg, W. Kohn, Phys. Rev. 136 (1964) B864.
3) W. Kohn, L. J. Sham, Phys. Rev. 140 (1965) A1133-A1138.
4) J. P. Perdew, A. Zunger, Phys. Rev. B 23 (1981) 5048.
5) J. P. Perdew, K. Burke, M. Ernzerhof, Phys. Rev. Lett. 77 (1996) 3865.
6) https://mdcl.issp.u-tokyo.ac.jp/scc/.
7) Y. Morikawa, K. Iwata, K. Terakura, Appl. Surf. Sci. 169-170 (2001) 11-15.
8) Y. Morikawa, H. Ishii, K. Seki, Phys. Rev. B 69 (2004) 041403(R).
9) T. Wassmann, A. P. Seitsonen, A. M. Saitta, M. Lazzeri, F. Mauri, Phys. Rev. Lett. 101 (2008) 096402.
10) L. Yang, C.-H. Park, Y.-W. Son, M. L. Cohen, S. G. Louie, Phys. Rev. Lett. 99 (2007) 186801.
11) W.-X. Wang, M. Zhou, X. Li, S.-Y. Li, X. Wu, W. Duan, L. He, Phys. Rev. B 93 (2016) 241403(R).
12) E. Clar, The Aromatic Sextet, Wiley, London (1972).
13) M. Randić, Chem. Rev. 103 (2003) 3449.
14) T. M. Krygowski, M. K. Cyrański, Chem. Rev. 101 (2001) 1385.
15) I. Gutman, Ž. Tomović, K. Müllen, J. P. Rabe, Chem. Phys. Lett. 397 (2004) 412.
16) T. Wassmann, A. P. Seitsonen, A. M. Saitta, M. Lazzeri, F. Mauri, J. Am. Chem. Soc. 132 (2010) 3440.
17) J. P. Rabe, M. Sano, D. Batchelder, A. A. Kalatchev, J. Microsc. 152 (1988) 573.
18) H. A. Mizes, J. S. Foster, Science 244 (1989) 559.
19) P. Ruffieux, M. Melle-Franco, O. Gröning, M. Bielmann, F. Zerbetto, P. Gröning, Phys. Rev. B 71 (2005) 153403.
20) K. Sasaki, K. Wakabayashi, T. Enoki, New J. Phys. 12 (2010) 083023.
21) G. M. Shedd, P. E. Russell, Surf. Sci. 266 (1992) 259.
22) H. Yang, A. J. Mayne, M. Boucherit, G. Comtet, G. Dujardin, Y. Kuk, Nano Lett. 10 (2010) 943.
23) Y. Niimi, T. Matsui, H. Kambara, K. Tagami, M. Tsukada, H. Fukuyama, Phys. Rev. B 73 (2006) 085421.
24) H. Huang, D. Wei, J. Sun, S. L. Wong, Y. P. Feng, A. H. C. Neto, A. T. S. Wee, Sci. Rep. 2 (2012) 1.
25) M. C. Wang, J. Leem, P. Kang, J. Choi, P. Knapp, K. Yong, S. Nam, 2D Mater. 4 (2017) 022002.
26) J. A. Baimova, E. A. Korznikova, S. V. Dmitirev, B. Liu, K. Zhou, Curr. Nanosci. 12 (2016)

184.

27) H. Lim, J. Jung, R. S. Ruoff, Y. Kim, Nat. Commun. 6 (2015) 8601.

28) L. Liu, W. Xiao, D. Wang, K. Yang, L. Tao, H. J. Gao, Appl. Phys. Lett. 109 (2016) 143103.

29) W. Zhu, T. Low, V. Perebeinos, A. A. Bol, Y. Zhu, H. Yan, J. Tersoff, Nano Lett. 12 (2012) 3431.

30) Y. Guo, W. Guo, J. Phys. Chem. C 117 (2013) 692.

31) J. Li, S. Li, T. Higashi, K. Kawai, K. Inagaki, K. Yamamura, K. Arima, Phys. Rev. B 103 (2021) 245433.

32) X. Li, W. Hua, J. Guo, Y. Luo, J. Phys. Chem. C 119 (2015) 16660.

33) Y. Liu, B. Song, C. Huang, L. Yang, J. Mater. Chem. A 10 (2022) 13527.

34) J. Wang, B. Chen, B. Xing, Environ. Sci. Technol. 50 (2016) 3798.

35) M. Sahoo, S. Ramaprabhu, Electrochimi. Acta 186 (2015) 142.

CHAPTER

5

NANOCARBON-ASSISTED CHEMICAL ETCHING ON GERMANIUM SURFACES

This chapter discusses our latest research results using nanocarbon catalysts. In Section 5.1, we introduce the research objectives for using nanocarbon in semiconductor surface processing. Section 5.2 primarily describes two process flows for nanocarbon-assisted chemical etching on semiconductor surfaces, including some equipment and key steps. Section 5.3 summarizes previous work by our research group, as well as the challenges faced. In Section 5.4, we report our latest progress in adding strong oxidants to the etching solution. Finally, Section 5.5 provides a summary of this Chapter, including the background, and the above-mentioned research for semiconductor surface processing using nanocarbon catalysts.

5.1 INTRODUCTION

This chapter's background builds upon the content of Chapter 2. In Chapter 2, we discussed the history of the birth of metal-assisted chemical etching, its applications, and why we aim to replace metal catalysts with nanocarbon catalysts (the drawbacks of metal catalysts). Additionally, in Chapter 2, we discussed the role of Chapter 5 within this thesis, specifically its connection to STM experimental observations (Chapter 3) and first-principles calculations (Chapter 4).

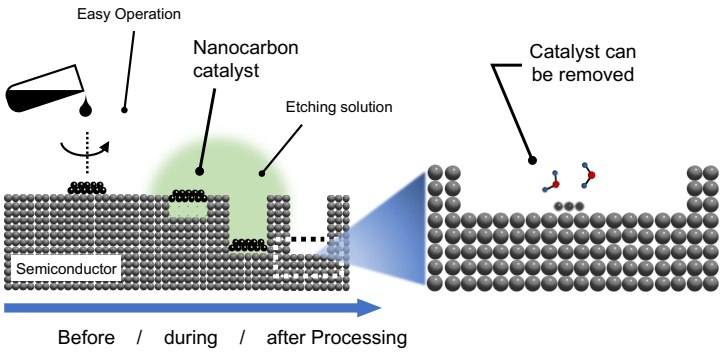

Figure 5.1 Nanocarbon catalysts were proposed as substitutes for metal catalysts in semiconductor surface microfabrication. For the disadvantages of metal catalysts, please refer to Figure 2.10 in Chapter 2.

This Section omits the aforementioned explanations and starts by introducing the research background of nanocarbon catalysts. The story begins with our group discovering the ability of a single-level nanocarbon sheets to etch the surface of semiconductors [1]. Specifically, by spin-coating dispersed monolayer graphene nanosheets on the Ge surface and immersing them in an oxygen-dissolved aqueous solution, we found that etch hollows formed on the Ge surface directly beneath the graphene sheets. After confirming the catalytic role of the graphene sheets, we proposed a novel semiconductor surface catalyst-assisted microfabrication technique, as shown in Figure 5.1. A key feature of this technique is the use of catalytically active nanocarbon materials to form micron-scale three-dimensional structures, such as trenches, on the semiconductor surface through a series of wet processes.

By developing a new technique that is simple to operate, cost-effective, and free of metal residues, we aim to achieve the processing effect shown in Figure 5.2. The goal is to etch micro- and submicron-sized three-dimensional structures with high aspect ratios on semiconductor surfaces as desired. The resulting semiconductor surfaces have potential applications in optoelectronics [2], energy conversion and storage [3], gas sensors [4], and so on, as detailed in Chapter 1 and Chapter 2.

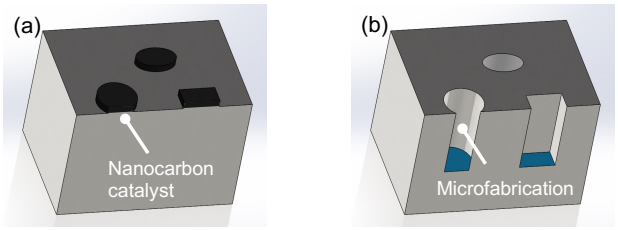

Figure 5.2 Schematic of semiconductor surface processing using nanocarbon catalysts.

To achieve this goal, there are two main steps. One is to prepare a solution containing highly catalytic nanocarbon materials and then select an appropriate process to load these materials onto the semiconductor surface according to a preset micro-pattern, as shown in Figure 5.2a. This step involves the chemical synthesis, characterization, and even calculation of nanocarbon materials. Designing and shaping micro-patterns of nanocarbon materials is also far more challenging than preparing metal catalysts. On the other hand, to etch the structures shown in Figure 5.2b, it is necessary to test the catalytic stability and durability of the nanocarbon catalysts, as well as to improve the etching process and optimize etching parameters.

As of now, we have developed various methods for preparing different nanocarbon catalysts

(Chapter 2) and preliminary tested their etching capabilities in oxygen-dissolved water [1,5]. In Chapters 3 and 4, we investigated the electronic states of the local structures of graphene and their correlation with catalytic activity [6,7]. In practical applications, we combined nanocarbon solutions with photolithography to etch trench structures on Ge surfaces [8]. However, several issues hinder the practical application of this technology. For instance, using nanocarbon materials to etch Ge surfaces in oxygen-dissolved water results in an etching rate of only about 6 nm/h. According to previous research on metal-assisted chemical etching [9-12], the use of strong oxidants appears to improve the etching rates of semiconductor surfaces such as Ge and Si. This chapter reports the experimental progress on adding H_2O_2 to the etching solution. By analyzing the etching mechanism in this solution, we also provide several suggestions for future work.

5.2 EXPERIMENTAL METHODS

Semiconductor manufacturing is often conducted in cleanrooms to minimize particles and chemical contaminants in the air, which are crucial for the production process. Figure 5.3 shows the fume hood equipped in Osaka University's Ultra Clean Facility (UCF), where the cleaning process of semiconductor surfaces is performed. Additionally, experiments involving the use of hazardous chemical reagents, such as wet etching, also need to be conducted inside such equipment with ventilation systems.

Figure 5.3 Fume hoods at Ultra Clean Facility.

In this study, there are two methods for processing semiconductor surfaces (e.g., Ge), as shown

in Figure 5.4. Both methods require cleaning the Ge surface and forming dispersed nanocarbon sheets, or films of a certain pattern, on the Ge surface via spin coating. Figure 5.4a depicts a simple, quick method that allows for the straightforward examination of the catalytic activity of individual graphene nanosheets. This method led to the initial discovery that nanocarbon materials could be used as catalysts to enhance the chemical etching of semiconductor surfaces. Graphene nanosheets are dispersed on the Ge surface using spin coating, followed by immersion in a solution for etching. After etching, some surface characterization techniques, usually atomic force microscopy (AFM), are used to detect the processing results.

Figure 5.4b builds on (a) by incorporating photolithography to create nanocarbon patterns before etching, and then the same etching experiment as in (a) was performed. The photolithography steps related to photoresist (from spin coat to lift-off) are implemented at the Advanced Research Infrastructure for Materials and Nanotechnology Open Facilities of Osaka University [13]. The details of the overall process in Figure 5.4b will be provided elsewhere. Some results obtained using the methods in Figures 5.4a and 5.4b will be discussed later.

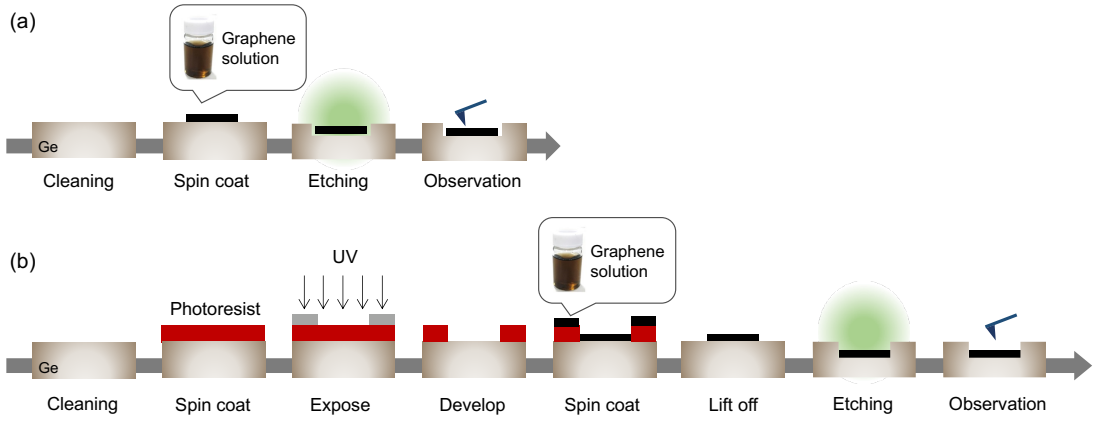

Figure 5.4 Two etching processes using nanocarbon catalysts in this study. (a) Spin-coating method to form dispersed nanocarbon sheets on the Ge substrate, which is then immersed in the etching solution. (b) Combination of photolithography on top of (a), aiming at controlling the pattern of the catalyst and thus enabling the processing of selected areas.

In the experiment shown in Figure 5.4a, some auxiliary experiments are needed to compare the coverage area of the same graphene sheet (on the Ge surface) before and after etching. Figure 5.5 shows that we used a nano-indentation device (ENT-2100Y, Nanotec) to leave multiple triangular

marks on the Ge surface, and we obtained AFM images of the same area before and after etching through these marks. The use of the nano-indentation device needs to be done before cleaning the Ge substrate. For detailed procedures and parameters, please refer to the reference 21. In the AFM observation experiment, it might be necessary to pre-confirm the approximate location of the triangular marks to narrow the search scope. One feasible method is to print a visible array of nano-indentations on the Ge surface. However, after locating the target area, it is necessary to avoid nano-indents in the AFM image, as the significant height differences caused by nano-indents can create difficulties in obtaining clear AFM images.

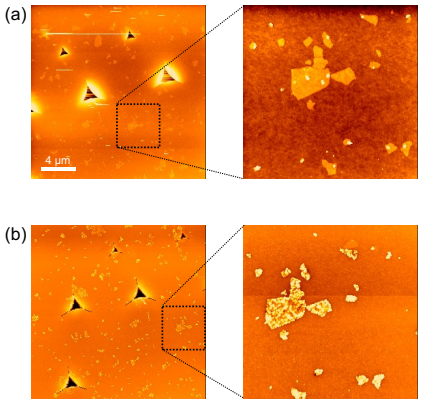

Figure 5.5 Nanoindentation was used to visualize the same surface area of Ge substrates (a) before and (b) after etching.

In the lithography process shown in Figure 5.4b, there are two critical steps, one of which is creating a pattern on the 4-inch Cr-coated glass mask (hereafter Cr mask). Figure 5.6a shows the light-emitting diode (LED) lithography system (PMT Corporation, PLS1010), which is used to engrave the pattern on the Cr mask. The pre-designed pattern can be drawn using a software program called Vectorworks. Before lithography, the positive photoresist (AZ5206E) was spin-coated on the Cr side of the unused Cr mask. During the lithography process, appropriate scanning speeds and other parameters need to be selected. After lithography, the mask needed to be developed, and then the exposed Cr needed to be etched.

Figure 5.6b shows the completed Cr mask. It is important to note that, up to this step, the mask must be kept away from direct exposure to sunlight. In Figure 5.6b, the clean wiper (white area) below shows where the Cr has been removed, leaving transparent glass. The reflective areas contain Cr that has not been removed. Figure 5.6 has four identical patterns, one of which is

magnified in Figure 5.6c. In the upper right corner of Figure 5.6c, there is a large triangle, visible to the naked eye, used for alignment. Figure 5.6c contains various shapes, with the smallest line width being 5 micrometers.

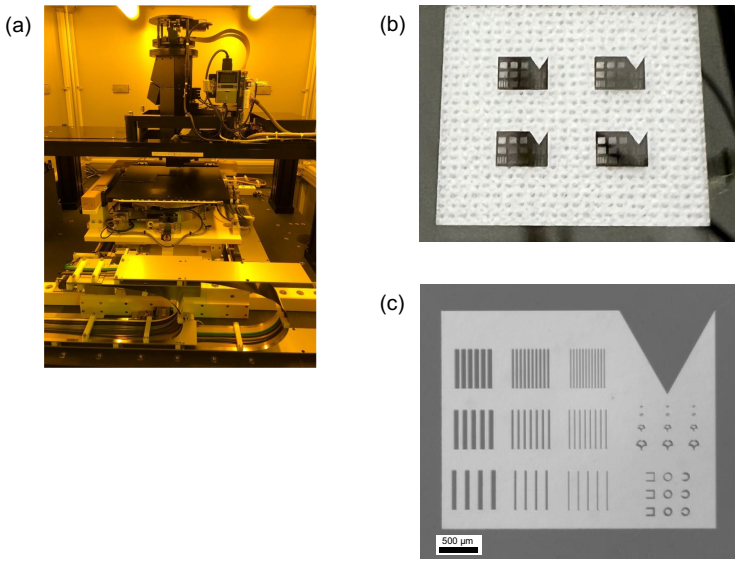

Figure 5.6 (a) Maskless LED lithography system. (b) Optical photograph, and (b) Optical microscope photograph of the obtained Cr mask.

In Figure 5.4b, another critical photolithography step involves creating a photoresist pattern on the Ge surface, as shown in Figure 5.7. In the process depicted in Figure 5.7a, a layer of photoresist is first spin-coated onto the Ge surface. Typically, before spin-coating the photoresist, a layer of hexamethyldisilazane (HMDS), an organosilicon compound, is spin-coated onto the Ge substrate to enhance the adhesion of the photoresist to the Ge surface. After spin-coating the photoresist, it needs to be baked. In the subsequent exposure step, a contact mask aligner (Mikasa, MA-10) shown in Figure 5.7b is used. The Cr mask fabricated in Figure 5.6b is placed above the Ge (between the Ge substrate and the light source). The Cr mask is brought into close contact with the Ge substrate under a certain degree of vacuum, and then ultraviolet light (g-line) is irradiated. Finally, the Ge substrate is developed in a developer solution, resulting in the pattern shown in Figure 5.7. Comparing Figures 5.6c and 5.7c, we can see that the photoresist pattern has been successfully obtained as planned. The green areas in Figure 5.7c represent the remaining photoresist, and the color indicates that the photoresist thickness is uniform. Since a positive photoresist was used, the exposed areas were removed. To achieve the results shown in Figure

5.7c, the development process typically needs to be kept within an appropriate time range.

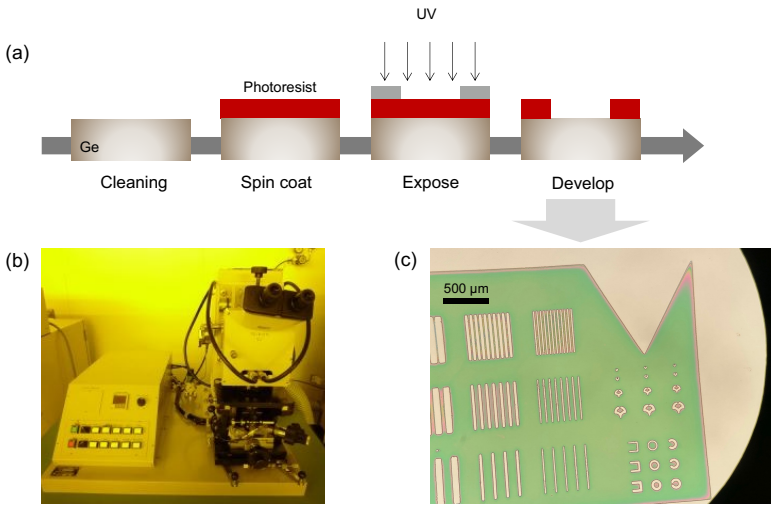

Figure 5.7 (a) The first half of the process shown in Figure 5.4b (up to the "develop" step). (b) Mask Aligner. (c) Photoresist patterns formed on a Ge substrate after development.

Completing the processing of the Ge surface according to the procedure in Figure 5.4b requires considerable effort, and even minor oversights can lead to experimental failure. In the initial stages, it is advisable to check the implementation of some key steps in Figure 5.4b, such as the microscopic observation shown in Figure 5.7c.

5.3 ETCHING BEHAVIOR IN OXYGEN-DISSOLVED WATER

In this section, we will introduce successful cases of etching the Ge surface using the two methods shown in Figure 5.4, as well as some issues that still need to be addressed. Both methods utilize the catalytic activity of nanocarbon materials to enhance the oxidation of Ge beneath them. The oxide of Ge dissolves in water, resulting in etched hollows.

A. Review of Our Past Research Results

First, Figure 5.8 shows the Ge surface etched following the procedure outlined in Figure 5.4a.

After spin-coating the graphene solution, the Ge surface exhibited dispersed single-layer graphene sheets (~1.0 μm thick; cross-sectional profile not shown). After etching, the AFM image of the same Ge surface showed etching hollows in the shape of graphene sheets [1)].

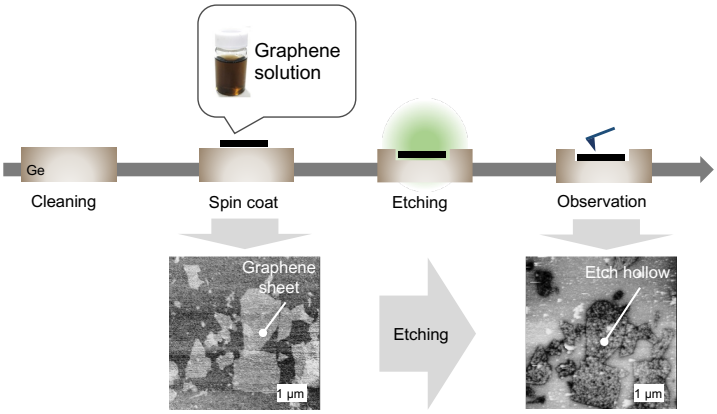

Figure 5.8 Single-level graphene sheets act as catalysts to form etch hollows on the Ge surface.

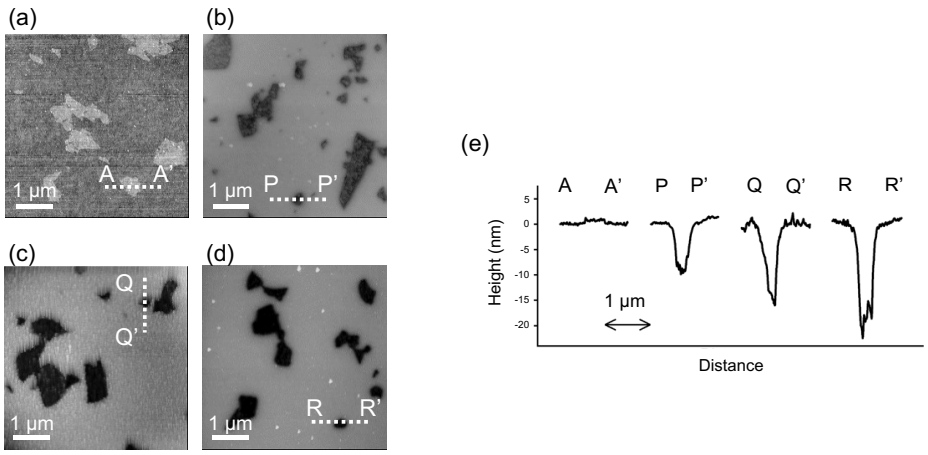

Figure 5.9 (a) AFM image of nanocarbon catalysts dispersed on a Ge surface before etching. (b–d) AFM images of Ge surfaces etched using three different types of nanocarbon catalysts. (e) Cross-sectional profiles along lines in (a–d).

In Figure 5.9, we used three different nanocarbon catalysts [8)] to etch the Ge surface under the same conditions (the etching process referenced in Figure 5.4a). The synthesis methods and XPS

characterization of these three different nanocarbon materials are detailed in Chapter 2. Figure 5.9 concludes that the depths of the hollows etched by different nanocarbon materials vary. This etching difference may arise from variations in the local structures of the nanocarbon materials, leading to differences in catalytic activity. This aspect is also the focus of our studies in Chapters 3 and 4.

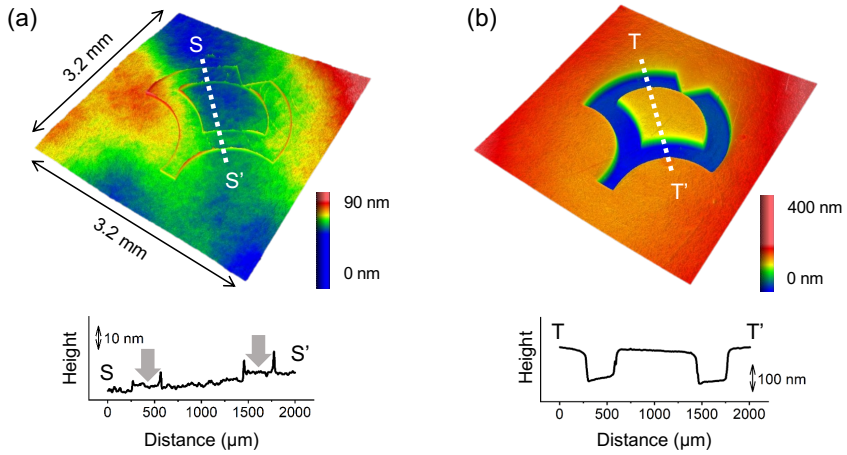

Figure 5.10 Application of photolithography in our nanocarbon-assisted chemical etching.

In Figures 5.8 and 5.9, the etching process shown in Figure 5.4a was used. Although this method is simple, the deposition of nanocarbon sheets on the Ge surface is random. Therefore, it can be used to quickly test whether the material has catalytic activity and evaluate the magnitude of its catalytic activity. To verify the feasibility of actual processing, it is still necessary to use the process shown in Figure 5.4b. Figure 5.10 shows that we successfully etched the desired trench structure [8] on the Ge surface (for a detailed description of this figure, see Figure 2.16).

B. Current Issues

Currently, we still face many challenges. For example, in Figure 5.10, the etching used the weakest etching-capable nanocarbon material (graphene oxide, which corresponds to Figure 5.9b). In the experiments shown in Figure 5.10, we tried to use nanocarbon materials that were better at etching (reduced graphene oxide, corresponding to Figures 5.9c and 5.9d), but their poor

dispersion in solution often prevented the formation of ideal films and predetermined patterns on Ge. The patterns in Figure 5.10 are millimeter-scale, far from achieving the desired microscale processing.

In Figure 5.11, we successfully produced micron-scale trench structures using the Cr mask shown in Figure 5.6c (corresponding to the bottom right part of the mask). However, two problems still need to be addressed. One is the low reproducibility of this result. Even on the same Ge substrate, the etching is uneven. The most likely scenario is that it is challenging to deposit nanocarbon film according to the design pattern in such small areas. This needs to be confirmed after the "lift off" step before etching. However, because the nanocarbon film is extremely thin and buried in the topography of the Ge surface, estimating its thickness (existence) is difficult.

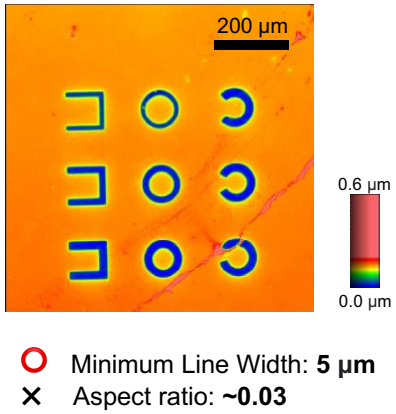

Figure 5.11 A case of selective area processing using nanocarbon catalysts. The minimum line width of the etch patterns reached 5 µm, but the aspect ratio was far from the desired target.

Another urgent problem to solve is that the trench structure in Figure 5.11 is only about 160 nanometers deep. Even considering the smallest line width of 5 micrometers, the aspect ratio is only around 0.03. To address this issue, one approach is to enhance the catalytic activity of the nanocarbon materials. Based on the results shown in Figure 5.9e, it is unlikely that high aspect ratio etching structures can be made with these three nanocarbon materials in the way they are used now, unless the nanocarbon materials or the etching process are greatly improved. Another approach is to make a slight change to the current method by replacing the oxygenated water we have been using with a solution containing strong oxidizers. The introduction to strong oxidants will be given in the next section.

5.4 IMPACT OF ADDING STRONG OXIDANTS TO ETCHING SOLUTION

To address the issue of low etching rates mentioned at the end of Section 5.3, we drew upon previous work. In Section 5.3A, we reviewed cases involving the use of strong oxidants in catalyst-enhanced chemical etching. Section 5.4B describes the progress of our own work, which involved adding hydrogen peroxide (H_2O_2) to the etching solution.

A. Use of Strong Oxidants in Past Wet Etching Studies

Figure 5.12 introduces the work of a research team [14-17] that, like us, is dedicated to applying nanocarbon catalysts to semiconductor surface microfabrication. In Figure 5.12a, they deposited nanocarbon films on the surface of Si and then performed etching in a gaseous environment [16]. Figures 5.12b and 5.12c show the etching results, which etched a hole about 1 μm deep in the shape of the nanocarbon film. Although their team used a Si substrate, the nanocarbon catalyst they used was similar to ours. We reasonably speculate that the H_2O_2 solution used in Figure 5.12 might enhance the etching performance of the nanocarbon material. Next, we will explain the role of strong oxidants, such as H_2O_2, in catalyst-assisted etching (etching mechanism).

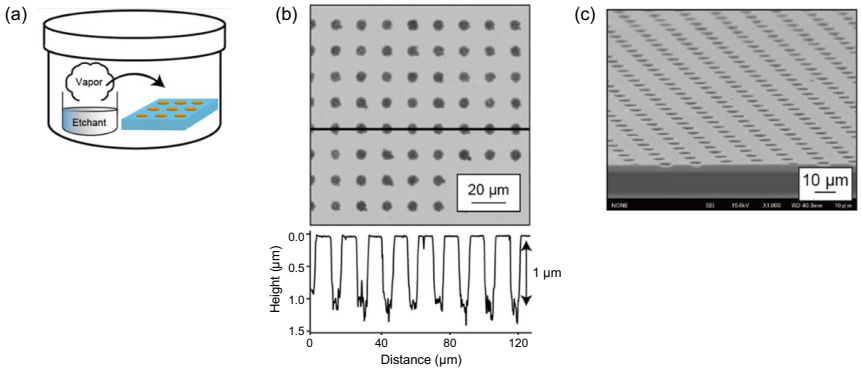

Figure 5.12 (a) Vapor-phase nanocarbon-assisted etching. (b) 3D laser microscopy topographic image, a cross-sectional profile along a line, and (c) scanning electron microscope image of silicon substrates loaded with nanocarbon sheets after the process in (a) at 22 °C for 16 h. The molar ratio of the etching solution was [HF]:[H_2O_2]=29:0.20 [16].

It is also worth mentioning that Figure 5.12a used vapor-phase etching, and their method of

depositing the nanocarbon film was similar to stamping (for details, please refer to reference 16). These two points are significantly different from the process shown in Figure 5.4. This may provide insights into solving some of the etching issues we faced in Section 5.3.

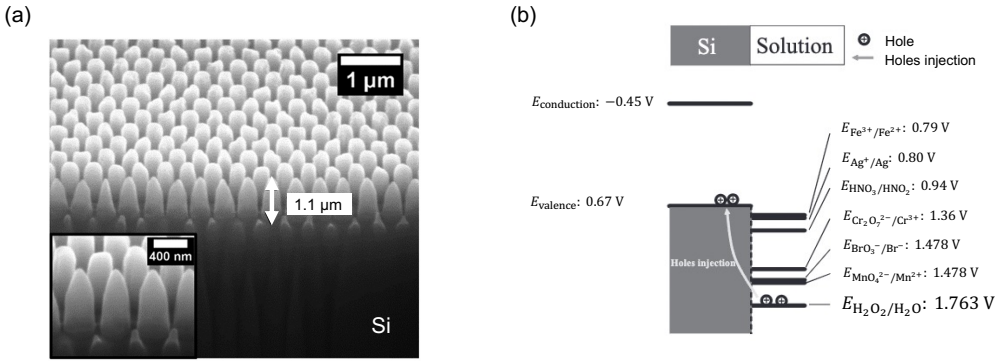

Figure 5.13 (a) Si nanostructures obtained in metal-assisted chemical etching using H_2O_2 [18]. (b) Scheme of the potential relationship between bands in a Si substrate and standard potentials of various oxidants [9].

In metal-assisted chemical etching (MaCE), it is also common to use strong oxidizers in the etching solution. In the experiment shown in Figure 5.13a, Si nanostructures were obtained using H_2O_2 [18]. In these studies, the etching is commonly explained through the generation, movement, and consumption of electrons and holes (as we mentioned in Figure 2.7b). Specifically, in the etching solution, the oxidant is reduced by catalysts such as metals, leading to the generation of holes. These holes then move to the semiconductor surface covered by the metal. Hole consumption refers to the promotion of local oxidation reactions at the semiconductor surface by the holes that have moved there. The resulting oxides dissolve in the solution, forming etch pits. In summary, the rates of hole generation and consumption determine the overall chemical reaction rate, while the movement and distribution of holes dictate the direction of etching.

In Figure 5.13b, the valence band of Si and the electrochemical potentials of various common oxidants used in chemical etching of Si (such as H_2O_2, HNO_3, $Fe(NO_3)_3$, $KMnO_4$, etc.) are summarized [9]. It can be observed that the standard potentials of these oxidants are more positive than that of the valence band of Si. Particularly, the standard potential of H_2O_2/H_2O at 1.763 V, significantly higher than the 1.23 V of O_2 dissolved in H_2O. H_2O_2 is likely to inject holes more readily into the valence band of Si, thereby promoting Si oxidation and dissolution. This also serves as the basis for adding strong oxidizers to our experiments.

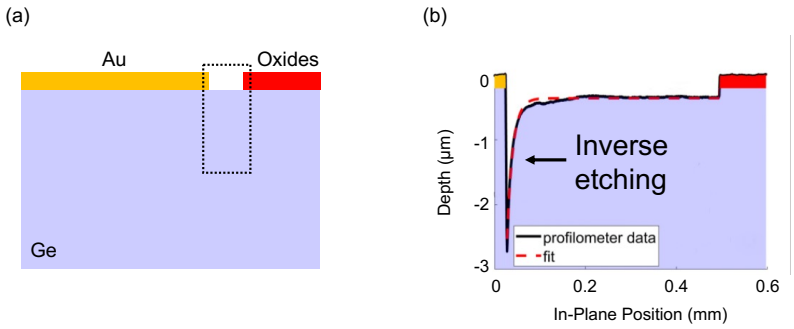

Figure 5.14 Inverse metal-assisted chemical etching was found in experiments using H_2O_2 [19]. (a) Schematic before etching. (b) Cross-sectional profile of the dotted box in (a) after etching.

In addition to the aforementioned strong oxidants increasing the rate of catalyst-assisted etching, some new etching phenomena have also been discovered. Namely, Lidsky [19] et al. observed inverse MaCE in Figure 5.14, where the area directly under Au is not etched, but the neighboring , exposed Ge experiences enhanced etching in H_2O_2 solution. This indicates that there are still significant gaps in our understanding of catalyst-assisted chemical etching and its mechanisms under different conditions. Undoubtedly, this also introduces many uncertainties in our experiments using H_2O_2.

B. Carbon-assisted Chemical Etching of Ge in H_2O_2

The purpose of this subsection is to unveil the morphology of Ge in our etching experiment using graphene-based catalysts when H_2O_2 is added to a solution. Since graphene oxide (GO) is easier to deposit as a single flake level on Ge than reduced GO (rGO), we use it as the starting material. X-ray photoelectron spectroscopy spectra have shown that GO flakes on Si [14,20], Ge [8], or InP [17] are reduced to a structure resembling rGO generated in a liquid by hydrothermal treatment or hydrazine when dipped in a solution containing an oxidant, like H_2O_2 or O_2. Considering this transformation, we term the etching phenomena of Ge in the following as nanocarbon (NC)-assisted chemical etching [21].

Experimental methods

The experimental procedure follows the steps outlined in Figure 5.4a. Details regarding the cleaning of the Ge substrate and the spin-coating of the nanocarbon solution can be found in the

reference 21. Two solutions, O_2-dissolved water (O_2 concentration: 7–9 ppm) or a mixture of ultrapure water and H_2O_2 (30%, Kishida Chemical), was used for etching. The H_2O_2 concentration was varied, ranging from 100 ppm to 200 ppm, and the solution temperature was controlled between 22 °C and 58 °C using a water bath (TR-3α, AS ONE).

Etch morphologies of Ge samples were characterized using atomic force microscopy (AFM, SPA-400, Hitachi High-Tech) in the tapping mode in air, employing a Si cantilever (spring const. 26 N/m; resonance freq. 300 kHz). To investigate how loaded NC flakes affect the etch morphologies of Ge below, we used the method illustrated in Figure 5.5.

Morphology of Ge Surface after Initial Etching

In Figures 5.15a and 5.15b, the arrangement of the etch hollows are identical to that of the GO flakes before etching. This shows that NC flakes help dissolve the Ge below in O_2-dissolved water, which fits with the anisotropic processing in MaCE on Si [9,10] and our research on rGO-assisted etching [1,8]. In Figures 5.15c and 5.15d, dotted arrows are markers to indicate the same position before and after etching in H_2O_2. The dotted polygons in Figures 5.15d and 5.15e show the approximate arrangement of some large GO flakes before etching in Figure 5.15c. Obviously, unlike Figure 5.15b, the etch hollows in Figure 5.15d underneath GO flakes do not exhibit a flat bottom. The observation area in Figure 5.15e was slightly adjusted to exclude the deep marker. In this image, pits of varying sizes are visible, all of which look to be situated within the polygons.

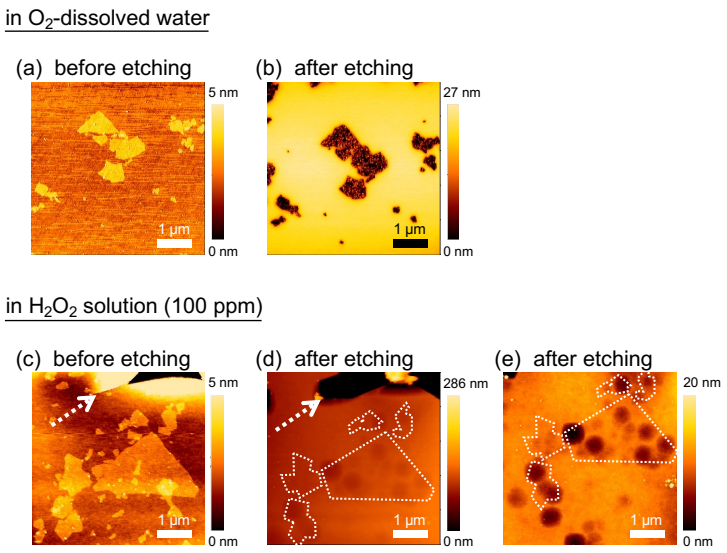

Figure 5.15 AFM topographic images of the same Ge surfaces before and after 8 h of etching at 22 °C in (a–b) O_2-dissolved water and (c–e) 100 ppm H_2O_2 solution.

To learn more about the result shown in Figure 5.15e, we looked at NC-loaded Ge samples at different etching times in Figures 5.16a–5.16d. Figure 5.16a and the profile along A-A' in Figure 5.16e reveal dispersed monolayer-thick (~1.0 nm) GO flakes. However, in Figures 5.16b–5.16d, GO flakes almost disappeared. Instead, Figure 5.16b resolves many small pits distributed inhomogeneously to form "pit groups" on the surface. According to the profile along B-B', the average width and depth of the four pits indicated by solid arrows are 90 nm and 2 nm, respectively. Though Figures 5.16a and 5.16b were taken at different areas, we suppose that these small pits are distributed in regions where GO flakes seem to have been present, as we found in Figure 5.15e. Figures 5.16c and 5.16d show that the number of pits decrease drastically but each pit grows after prolonged etching. The initial pits in Figure 5.16b appear to merge into a larger pit, with a typical width of 0.6 μm and depth of 12 nm, as shown in the profile along D-D' in Figure 5.16e. A noteworthy point is that the edges of each pit in Figures 5.16c and 5.16d, particularly in Figure 5.16c, appear to run perpendicular or parallel to each other to form square-like shapes in the entire scanned area.

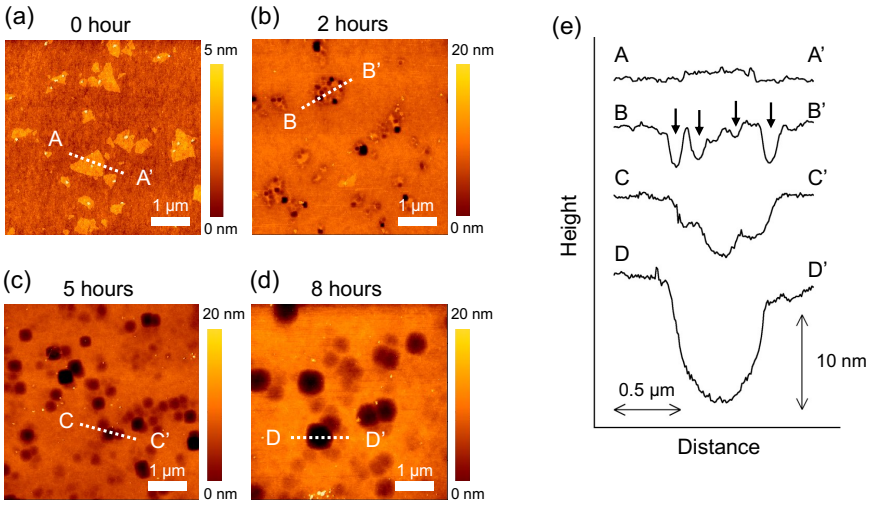

Figure 5.16 AFM images of NC-assisted etching on Ge substrates at 22 °C in 100 ppm H_2O_2. The etching times were (a) 0, (b) 2, (c) 5, and (d) 8 h, respectively. (e) Cross-sectional profiles along the dotted lines in (a–d).

Morphology of Ge Surface after Prolonged Etching

Figure 5.17 shows accelerated etching in O_2-dissolved water or in a more highly concentrated

H_2O_2 solution at elevated temperatures. As we found in Figure 5.15b, the lateral size of the etch hollows in Figures 5.17a–5.17d is also similar to that of initial GO flakes before etching, even at enhanced temperatures. In Figure 5.17e, numerous small pits are formed at 31°C. Etching at higher temperatures in Figures 5.17f and 5.17g created larger and deeper hollows, of which the trend is clearer than those in Figures 5.16c and 5.16d. A treatment at higher temperatures in both O_2-dissolved water and 200 ppm H_2O_2 created deeper hollows, reaching ~60 nm, as shown in the profiles along the R-R' and U-U' lines in Figures 5.17d and 5.17h, respectively. The profiles along lines S-S', T-T', and U-U' in Figure 5.17h show a difference in lateral sizes between the topmost and the bottommost of the etch hollows to be approximately 0.33, 0.65, and 1.03 μm, respectively. In contrast, those in Figure 5.17d are almost constant (~0.24 μm). In Figure 5.17g, the size of the hollows is apparently larger than that of the loaded flakes. Thus, we suppose that enhanced etching proceeded laterally around the catalyst in H_2O_2, which is different from etching in O_2-dissolved water.

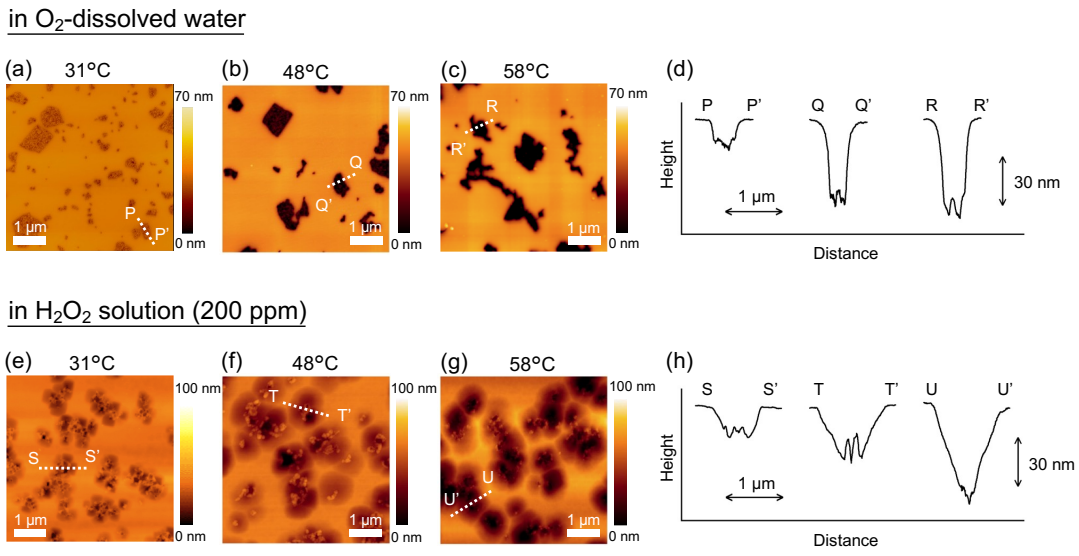

Figure 5.17 AFM images of NC-loaded Ge substrates etched for 3 h at different temperatures in (a–c) O_2-dissolved water and (e–g) 200 ppm H_2O_2 solution. The cross-sectional profiles along the lines in (a–c) and (e–g) are presented in (d) and (h), respectively.

Mechanism of Nanocarbon-assisted Chemical Etching

The possible mechanism [1,8] in Figures 5.18a and 5.18b is as follows: dissolved O_2 molecules initiate an oxygen reduction reaction (ORR), leading to the oxidation of NC-covered Ge and the

dissolution of the resultant oxide (GeO_2). ORR occurs on the NC surface:

$$O_2 + 4H+ \rightarrow 2H_2O + 4h^+ \quad (5.1)$$

The catalytic activity of outer edges and vacancies in NC flakes is believed to play a crucial role in Equation (5.1). The generated holes are consumed in the underlying Ge to form a GeO_2 layer. Another possibility is that dissociated O_2 atoms at vacancies [22] may induce direct oxidation of Ge. As the GeO_2 layer is dissolved, Equation (5.1) continues to form hollows with a flat bottom.

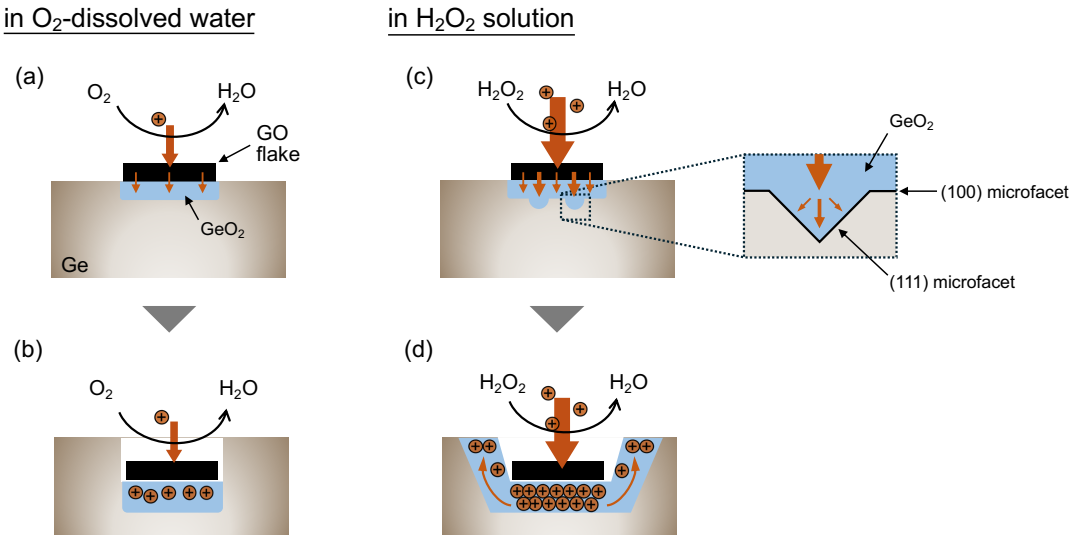

Figure 5.18 Mechanisms for NC-assisted etching on Ge substrates in (a–b) O2-dissolved water and in (c–d) H2O2 solution.

In Figures 5.18c and 5.18d, the H_2O_2 is reduced at the NC flake:

$$H_2O_2 + 2H^+ \rightarrow 2H_2O + 2h^+ \quad (5.2)$$

Equation (5.2) is widely accepted as a cathode reaction [9,10] in MaCE using H_2O_2, and nanocarbon is recognized as an effective catalyst for oxidant reduction reactions involving O_2 [23], H_2O_2 [24], and NO_3^- [25]. The etching in H_2O_2 formed inhomogeneous pitted morphologies such as in Figure 5.15e, differing from the etch morphology in O_2-dissolved water as shown in Figure 5.15b. One explanation is that the active sites on NC flakes promoting Equation (5.2) may be different from those for Equation (5.1). Therefore, an uneven distribution of holes is injected into the Ge surface in Figure 5.18c, which causes the pitted morphology. Another explanation is that Amirfakhri [26]

et al. showed that H_2O_2 decomposes into oxygen through the reaction:

$$2H_2O_2 \rightarrow O_2 + 2H_2O \quad (5.3)$$

The resultant O_2 molecules, together with the dissolved O_2 molecules in the H_2O_2, participated in Equation (5.1). The simultaneous occurrence of both Equations (5.1) and (5.2) under the NC flake in H_2O_2 may cause the pitted morphology. As mentioned in Figure 5.16, such pits first grow to have their edges form a square-like shapes. We reported the creation of inverted pyramid structures with Ge(111) microfacets. Because Ag or Pt particles in O_2-dissolved water sped up the etch rate of a Ge(100) facet more than Ge(111). Although the pits in Figure 5.16 are not exactly inverted pyramids [27]), anisotropic etching at the initial stage of NC-assisted etching in H_2O_2 is most likely responsible for their square-like edges.

V-shaped etch profiles were visualized in etching using H_2O_2, which also differ from the case in O_2-dissolved water. As mentioned in Figures 5.17g and 5.17h, the lateral etching may occur in regions without NC coverage, hereafter referred to as the "off-NC area." This is because H_2O_2, being a strong oxidant [9]), generates a larger number of holes compared to dissolved O_2 molecules. The holes diffuse from NC-covered Ge to off-NC areas or to the walls of the pit if hole consumption at the Ge/NC interface is slower than hole injection. Accordingly, off-NC areas or sidewalls of the pit may be etched, as depicted in Figure 5.18d. This effect becomes more pronounced with the increasing etching time in Figures 5.16b−5.16d and the rising temperatures in Figures 5.17e−5.17g. When the etch rate is sufficiently high, anisotropic etching no longer occurs, and pits with square-like edges merge and decrease in number, resulting in larger pits with curved edges. Similar lateral etching was observed in MaCE on Si [10]). Namely, when etching is performed in a low-concentration H_2O_2 solution, pores are formed with diameters matching the size of Ag particles. As the amount of H_2O_2 increases, holes may reach the pore walls, creating microporous Si. When microporous Si is dissolved, empty cone-shaped pores are left.

We use H_2O_2 in this study to achieve a higher etch rate. However, as shown in Figure 5.17, treatment with H_2O_2 does not create deeper hollows compared to dissolved O_2 (~ 60 nm at 58 °C for both solutions). One possible reason is that the etch rate is determined based on the etching depth observed in AFM images. The etching depth is measured between the assisted etching beneath nanocarbon and the natural etching occurring in the off-NC area. Thus, the use of a strong oxidant does not always lead to greater etching depths. For example, different solutions have been used to see changes in the etch morphology. The surface position of the NC-covered InP [17]) after etching is even higher than that of the off-NC area. This is because H_2SO_4-containing solutions or HCl-H_2O_2 solutions naturally etch at a fast rate. Secondly, as mentioned in Figure 5.18d, the etching depth did not significantly enhance due to incomplete consumption of the injected holes, resulting in lateral diffusion and lateral etching. Others have controlled the etching profile by

applying an electric bias from the back side of Si substrates [27], which may also help prevent lateral diffusion of holes in Ge.

Supporting Information: EDX Analysis

We also conducted Scanning Electron Microscopy (SEM) with Energy Dispersive X-ray analysis (EDX) in this experiment, of which results are shown in Figure 5.19. We used a Ge sample spin-coated with a graphene oxide (GO) solution but did not etch it. The concentration of GO in this solution was 1.0 g/L, which is 10 times higher than that (0.1 g/L) used in the Figure 5.15–5.17.

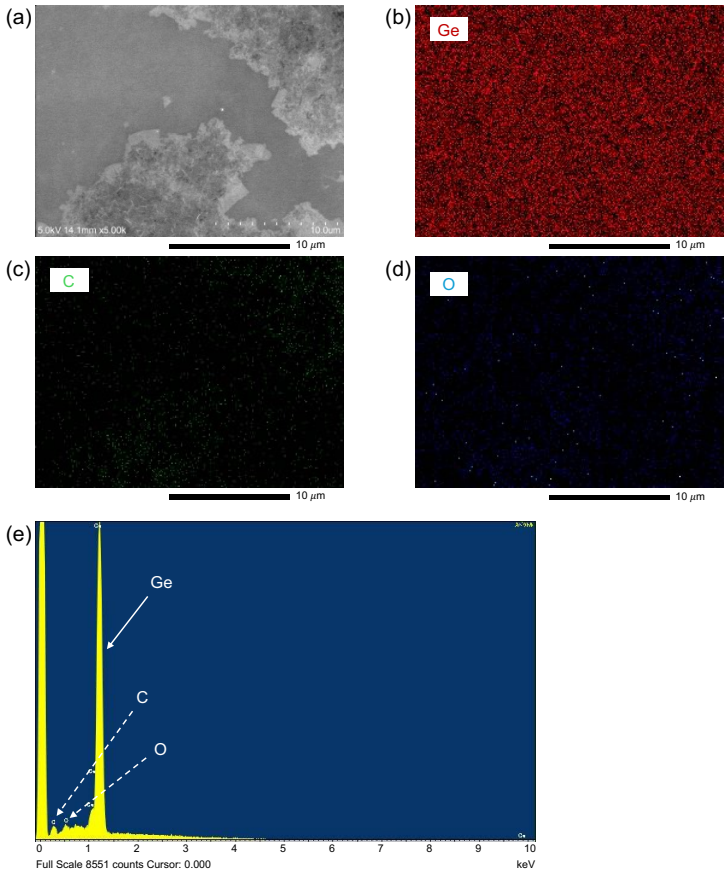

Figure 5.19 SEM image (a) and elemental maps (b–d) of the Ge surface spin-coated with 1.0 g/L GO solutions. (e) EDX spectrum of the SEM image (a), indicating the presence of Ge, C, and O.

In Figure 5.19, large GO flakes are visible on the Ge surface. Considering the AFM images presented in Figures 5.15a and 5.15c, we deduce that the large flakes in Figure 5.19a are not GO at a monolayer level but rather GO films consisting of several monolayers. Despite the presence

of these thick GO flakes, clear flake images are not discernible on both the carbon and oxygen images in Figures 5.19c and 5.19d, respectively. This limitation arises because EDX is not sufficiently surface-sensitive to detect GO flakes that are only one or a few monolayers thick. Therefore, we find it challenging to discuss the composition and structure of GO solely based on SEM-EDX analysis.

5.5 SUMMARY

Instead of metal catalysts, we suggest using nanocarbon materials as a new catalyst-assisted chemical etching method. This method was used to build three-dimensional structures on the surfaces of semiconductors. To meet the application needs of optical devices such as optical waveguides and photodetectors, this technology needs to demonstrate the ability to create high-aspect-ratio, micron-scale structure arrays on semiconductor surfaces.

This technology primarily employs wet processes, such as spin coating and photolithography, to deposit nanocarbon solutions on Ge surfaces. Although we previously discovered the catalytic activity of individual nanocarbon sheets and have demonstrated the feasibility of practical applications (selective area processing), a major current issue is that the etching speed is excessively slow.

To address this problem, we investigated past research on catalyst-assisted chemical etching using strong oxidants on semiconductor surfaces. In the latest experiments, we studied the impact of H_2O_2 on nanocarbon-assisted Ge chemical etching. The pits formed beneath the loaded nanocarbon gradually enlarge as the etching progresses. Although a single pit is not entirely an inverted pyramid structure, its square-like-shaped edges resemble the morphology of exposed Ge(111) microfacets after MaCE. Nanocarbon (NC) promotes the reduction of H_2O_2 molecules, so hole injection and etching also occur in the off-NC area. Small pits eventually merge to form larger hollows that seem to stretch beyond the original NC-covered area. The key to achieving uniform and deeper etch structures using NC catalysts in H_2O_2 lies in controlling hole diffusion.

REFERENCES

1) T. Hirano, K. Nakade, S. Li, K. Kawai, K. Arima, Carbon 127 (2018) 681.
2) H. Li, J. Liu, G. Wang, E. Wang, C. Xie, ACS Appl. Electron. Mater. 1 (2019) 1070.
3) A. I. Hochbaum, R. Chen, R. D. Delgado, W. Liang, E. C. Garnett, M. Najarian, A. Majumdar, P. D. Yang, Nature 451 (2008) 163.

4) M. Sainato, L. M. Strambini, S. Rella, E. Mazzotta, G. Barillaro, ACS Appl. Mater. Interfaces 7 (2015) 7136.
5) S. Li, K. Nakade, T. Hirano, K. Kawai, K. Arima, Mater. Sci. Semicond. Process. 87 (2018) 32.
6) J. Li, S. Li, T. Higashi, K. Kawai, K. Inagaki, K. Yamamura, K. Arima, Phys. Rev. B 103 (2021) 245433.
7) J. Li, K. Inagaki, K. Arima, Phys. Rev. Res. 6 (2024) 013252.
8) R. Mikurino, A. Ogasawara, T. Hirano, Y. Nakata, H. Yamashita, S. Li, K. Kawai, K. Yamamura, K. Arima, J. Phys. Chem. C 124 (2020) 6121.
9) Z. Huang, N. Geyer, P. Werner, J. de Boor, U. Gösele, Adv. Mater. 23 (2011) 285.
10) C. Chartier, S. Bastide, C. Lévy-Clément, Electrochim. Acta 53 (2008) 5509.
11) S.-H. Shin, Y. Liao, B. Son, Z.-J. Zhao, J.-H. Jeong, C. S. Tan, M. Kim, J. Mater. Chem. C 9 (2021) 9884.
12) G. Yoo, Y. Park, P. Sang, H. W. Baac, J. Heo, Opt. Mater. Express 6 (2016) 2567.
13) https://nanoplatform.osaka-u.ac.jp/index.html.
14) W. Kubota, R. Ishizuka, T. Utsunomiya, T. Ichii, H. Sugimura, Jpn. J. Appl. Phys. 58 (2019) 050924.
15) W. Kubota, T. Utsunomiya, T. Ichii, H. Sugimura, Langmuir 58 (2019) 050924.
16) W. Kubota, R. Yamaoka, T. Utsunomiya, T. Ichii, H. Sugimura, ACS Appl. Nano Mater. 5 (2022) 11707-11714.
17) W. Kubota, T. Utsunomiya, T. Ichii, H. Sugimura, Jpn. J. Appl. Phys. 62 (2023) SG1040.
18) J. D. Kim, M. Kim, C. Chan, N. Draeger, J. J. Coleman, X. Li, ACS Appl. Mater. Interfaces 11 (2019) 27371-27377.
19) D. Lidsky, J. M. Cain, T. Hutchins-Delgado, T. M. Lu, Nanotechnology 34 (2022) 065302.
20) Y. Tu, T. Utsunomiya, S. Kokufu, M. Soga, T. Ichii, H. Sugimura, Langmuir 33 (2017) 10765.
21) J. Li, S. Yamamoto, K. Inagaki, K. Arima, Electrochem. Commun. 163 (2024) 107735.
22) M. Topsakal, H. Sahin, S. Ciraci, Phys. Rev. B 85 (2012) 155445.
23) L. Tao, Q. Wang, S. Dou, Z. Ma, J. Huo, S. Wang, L. Dai, Chem. Commun. 52 (2016) 2764.
24) K. Lacina, O. Kubesa, P. Vanýsek, V. Horáčková, Z. Moravec, P. Skládal, Electrochim. Acta 223 (2017) 1.
25) K. Kamiya, K. Hashimoto, S. Nakanishi, ChemElectroChem 1 (2014) 858.
26) S. J. Amirfakhri, D. Binny, J.-L. Meunier, D. Berk, J. Power Sources 257 (2014) 356.
27) S. J. Rezvani, N. Pinto, L. Boarino, CrystEngComm 18 (2016) 7843.

CHAPTER

6

SUMMARY AND OUTLOOK

The first half of this chapter provides a summary of each of the first five chapters individually. The first two chapters primarily introduce the background, outlining the research direction, application scenarios, research topics, and research strategies of this thesis. Chapters three to five, respectively, describe the three research projects utilized in this thesis. The details of each project include its principles, necessity, experimental or computational methods, achieved results, and interconnections with other projects.

The latter part of this chapter focuses on the future work of the three research projects mentioned above. It sets objectives for them, provides research suggestions, and analyzes the feasibility of these suggestions.

6.1 SUMMARY

Nanocarbon-assisted chemical etching (NCaCE) utilizes the catalytic activity of graphene-based materials to promote the oxidation and removal of semiconductor surfaces in contact with them in a liquid environment. This is a novel wet process that does not use noble metal catalysts, allows for anisotropic processing, and ensures high-quality processed surfaces. Scanning tunneling microscopy was used to look at the atomic structure of the nanographene surface. Specifically, the electron density distribution near local defects was studied, which revealed a new type of superstructure. First-principles calculations revealed that this special electronic structure originates from linear defects within the nanographene, such as edges or wrinkles, and investigated the potential of these defects as active sites. Subsequently, in the actual NCaCE of Ge surfaces, a strong oxidizing agent was added to the etching solution. The Ge surface's new etching morphology was observed, and the mechanism was discussed, providing guidance for controlling the etching direction in future work.

Chapter 1 describes the historical development of semiconductor microfabrication, from microelectronics to optoelectronics. It discusses the development, applications, and technical challenges of optoelectronics. Furthermore, it mentions the purpose of this thesis, the research scope, and the research strategies used.

Chapter 2 introduces the principles, classifications, applications, and advantages and disadvantages of common semiconductor processing techniques. These techniques include thin

film deposition, lithography, and etching, which are related to our research. Then, we introduce metal-assisted chemical etching, a novel wet etching method. We describe its processing methods, etching mechanisms, and wide applications. We also briefly introduce our team's work on metal-assisted etching on Ge surfaces and discuss the challenges faced by this technique. Subsequently, we propose using non-metallic materials to replace noble metal catalysts. Next, we detail the catalytic properties and preparation methods of carbon-based materials represented by graphene and their application as catalysts in semiconductor surface processing in our research. Finally, we describe how to develop this technology, providing an overall description of the thesis structure and the contents of each research project.

In Chapter 3, to understand the atomic structure of the nanocarbon catalysts used in etching and the electron density distribution of some potential active sites, we observed the surfaces of finite-sized graphene sheets using scanning tunneling microscopy. During this observation, we discovered a novel electronic state and reproduced it on different types of graphene materials. After analyzing some atomic arrangements and sizes, we proposed that this special lattice pattern might originate from the overlap of other electronic states. To verify this theory, we also discussed how first-principles calculations would be used to analyze the experimental results.

- We attempt to distinguish between the atomic structures of reduced graphene oxide (rGO) and regular exfoliated graphene. In STM observations of nanographene sheets with similar side lengths ranging from tens to hundreds of nanometers, it was found that rGO sheets tend to exhibit curved edges, while exfoliated graphene sheets tend to show somewhat linear edges. Although at the atomic structure level, the edge structures of both are quite complex (non-linear), this difference might be attributed to the introduction of small amounts of oxygen-containing functional groups at the edges of rGO sheets during the synthesis process.

- Within the interiors of different types of graphene sheets, we observed the previously reported triangular structures and rhombic superstructures. The triangular structure is observed within the flat carbon network and originates from the AB stacking, resulting in the observation of three B-type carbon atoms in the hexagonal structure, with a lattice constant of approximately 0.246 nm. The rhombic superstructure arises from the disruption of atomic symmetry at the edges of finite-sized graphene, causing the electrons inside to reflect at the edges. Such superstructures typically appear within a few nanometers of the edge and revert to the triangular structure further away in the interior.

- In addition to the triangular structure and rhombic superstructure, we have repeatedly

observed a novel rectangular electronic structure on rGO nanosheets and exfoliated graphene nanosheets (with STM image sample biases of -0.05V or -0.01V). First, this novel electronic structure cannot be used as a distinguishing feature between rGO and regular graphene. Therefore, we focused on exploring the reasons for the appearance of the rectangular structure within the hexagonal structure of regular graphene sheets.

- Most notably, the rectangular structure appears in the edge region of the small graphene flakes. Naturally, we compared it with the rhombic structure originating from the armchair edge. By comparing the characteristics of both, we proposed the possibility that the rectangular structure is produced by the overlap of rhombic structures from different directions.

- We attempted to analyze the changes in the rectangular structure by varying the magnitude and polarity of the sample bias in the STM observation experiments. However, so far, no clear atomic images have been obtained in these experiments.

- To verify the rectangular structure observed in the experiment, we devised a plan using first-principles calculations. We briefly introduced the computational model, armchair-edge graphene nanoribbons, and some parameters (such as ribbon width, simulated sample bias), used to create the overlapping of two sets of rhombic superstructures.

In Chapter 4, to explain the origin of a novel electronic structure observed in STM experiments, we calculated the electronic structure of graphene nanoribbons. Under small sample voltages identical to those used in the experiments, we obtained the same rectangular structure as observed experimentally. Additionally, we explored the impact of varying the sample voltage in the calculations and the wrinkle structures in the model on the electronic structure of the graphene nanoribbons. Finally, we discussed the effects of these defect structures on the chemical activity of graphene.

- We first verified the accuracy of our computational models and methods. Through structural optimization calculations of the graphene model, we obtained the graphene lattice structure. By calculating the band structure of graphene nanoribbons, we reproduced the results previously reported in the literature.

- In the simulation of STM images for graphene nanoribbons, we found that besides the STM

image features exhibiting a triple periodicity change based on the width of the nanoribbons, a rectangular structure was discovered in the nanoribbons with a width of $W = 3a$. Using Clar's theory from organic chemistry, we explained the internal electron movement within the graphene nanoribbons and thereby accounted for the appearance of the rectangular structure.

- In comparing the rectangular structures obtained from the experiments, we found that the characteristics of the rectangular structures obtained by both methods are identical. Moreover, whether in the experiments or the calculations, the rectangular structure tends to resemble a trapezoidal structure. In the calculations, the upper and lower sides of the rectangular structure are 2.05 Å and 2.22 Å, respectively. Such a small difference is indistinguishable in the STM experiments.

- Reviewing the internal structure of the graphene sheets observed in Chapter 3, we found that there is a height difference of about 0.1 nm, or a wrinkle structure, near the regions where the rectangular structure appears. We propose that this is why the results observed in the graphene sheets appear in our calculations using graphene nanoribbons.

- In the calculations of the sample voltage dependence of the electronic states of graphene nanoribbons, we found that the rectangular structure appears only at low voltages, which include the electronic states at the top of the valence band. This result has also been verified through calculations with different k-point sampling, leading to the same conclusion. When the sample voltage is relatively high, the hexagonal structure of graphene appears. These two observations are consistent with our STM experiments and previous computational work.

- To better align with experiments and to study the wrinkle structures, we introduced this linear defect into the graphene nanoribbon model. We found that the wrinkle structure, like the edge structure, altered the electronic structure of the graphene nanoribbon. In some nanoribbons, where rectangular structures would not normally appear, the presence of wrinkle structures led to the observation of rectangular patterns. We also studied the density of states (DOS) of the carbon atoms in these wrinkle structures. We found an increase in the DOS near the Fermi level, which could enhance the adsorption and binding of other molecules to the wrinkle structures. This result might be related to the catalytic activity of nanocarbon catalysts and provides new insights into the modification of graphene.

In Chapter 5, to enhance the etching rate of nanocarbon-assisted chemical etching, we added a strong oxidant, hydrogen peroxide (H_2O_2), to the etching solution. We found that the etching rate of the Ge surface did not simply increase through this method. Additionally, we observed an etching morphology in the H_2O_2 etching process that differed from previous experiments involving oxygen-dissolved water. We analyzed its formation through hole diffusion and explained the etching mechanism in the H_2O_2 solution. Finally, we provided suggestions for achieving the desired etching morphology and rate in future work.

- Through in-situ AFM observations, we found that the etching-induced hollows, similar to those in oxygen-dissolved water etching, are catalyzed by graphene sheets and are located directly beneath them. However, these hollows do not mirror the shape of the graphene sheets; instead, they consist of multiple processed pits of various sizes.

- An investigation was conducted on the etching time dependence of etch pits in H_2O_2 solution. It was found that with the extension of etching time, the size and depth of etch pits gradually increased. It was also observed that some large etch pits were formed by the fusion of small etch pits. In addition, in experiments using this strong oxidizing agent, the presence of graphene flakes could not be distinguished on the etched Ge surface.

- In our investigation of the solution temperature dependence of etched pits, we found that temperature has a more pronounced effect on the formation and merging of etched pits compared to etching time. We found that the shape of these etched pits closely resembles the inverted pyramid structure observed in metal catalyst etching. Although the etching rate remains unchanged compared to etching in oxygen-containing water, the cross-sectional view of the etched pits exhibits a different “V” shape, indicating the occurrence of lateral etching.

- We explain the formation of uneven etching pits in H_2O_2 solution from the perspective of hole diffusion. Similarly, we illustrate that the formation of V-shaped etching pits originates from the excess holes transferring to the surrounding areas not covered by graphene flakes. Moreover, based on previous work, it is indicated that an electric field needs to be introduced into our etching setup to control the movement of holes.

6.2 OUTLOOK

For future research plans, recommendations are proposed for the three research projects in this thesis, despite the different order of appearance compared to the composition of the chapters in the thesis.

To apply nanocarbon-assisted chemical etching to practical production processes, two challenges need to be addressed: improving the etching rate and achieving microscale processing. We have provided prospects from four aspects: etching solution, process flow, nanocarbon catalysts, and semiconductor materials.

- Etching Solution: Although the experiment with adding H_2O_2 did not achieve an improvement in etching rate, we still gained insights into different etching morphologies and mechanisms. There are many aspects of our research that can be further explored, including the H_2O_2 solution used in this experiment, other oxidants mentioned in previous literature, and mixtures with acidic solutions. My suggestion is to experiment with new etching solutions and spin-coated graphene sheets, which is simple and fast. If promising results are found with certain solutions, it would be worthwhile to systematically investigate their effects on the etching of Ge surfaces.

- Process Flow: This project ultimately aims to create controllable micrometer-scale patterns on semiconductor surfaces. At such small dimensions, besides enhancing etching rates, stable, reproducible, and uniform processing outcomes are currently areas where we lack advancements.

  For the formation of graphene films, it is preferable in the current photolithography process to detect their formation status (integrity of the pattern, thickness of the film, etc.) before the etching step. It is important to note that many steps in the current process can affect it. If difficulties arise in detection due to the extremely thin thickness of graphene or other reasons, it may be necessary to explore new processes that can better form graphene films. Although spin-coating is very convenient and compatible with the use of graphene solutions, I have always been concerned about its instability (part of which may be due to suboptimal process parameters). Additionally, it cannot control the thickness of graphene films (for example, within the typical range of 20 nm to 100 nm for metal catalysts), which poses a significant obstacle to the investigation and application of this technology. In this regard, reference can be made to methods such as the “stamping” technique used in other literature (as introduced in this thesis).

We proposed an approach in this thesis that suggests using an electric field to guide hole diffusion to control etching shape and enhance etching rate. The validation of experimental equipment setup and methods should begin with metal-assisted chemical etching. Given the lack of prior experience in this field, a thorough investigation is necessary at the initial stage, and it is crucial to consider starting with simpler methods.

- Nanocarbon Catalyst: For the three graphene solutions currently being used, there are challenges such as insufficient etching rate and poor dispersion of some graphene. However, these issues may be improved by changing the etching solution or process. Additionally, during continuous etching, factors such as the etching capability of monolayer graphene, the stability of the catalysis in the solution, and even the stability of graphene itself need to be considered. While ensuring the formation of graphene film patterns before etching, it is worth exploring colloidal or solid forms of graphene catalysts, in addition to liquid-phase graphene catalysts.

- Semiconductor Material: Currently, etching does not involve materials other than Ge and Si. From an application perspective, some semiconductor material compounds are worth investigating. In such cases, previous research experience in process flow and catalysts remains relevant. However, the etching solution needs to be reselected according to different semiconductors.

For the STM experiments, we explain from two points: the fundamental properties of graphene and graphene catalysts.

- Electronic Structure of Graphene: Combined with theoretical calculations, we have gained some understanding of edge and wrinkle structures. However, these defects are relatively idealized (single or linear). In addition to considering other, more complex types of defects, we also need to consider more complex situations that exist in reality. For instance, we must take into account certain sp^3 hybridizations and the cumulative impact of numerous defects. To understand these local structures, in addition to the difficulty of experimental observation, a certain level of theoretical knowledge is also required.

- Catalytic Activity of Graphene: Regarding the reduced graphene oxide with higher catalytic activity, our understanding is just the tip of the iceberg. Its atomic structure and differences from other graphene materials at the atomic level are yet to be fully explored. The

accumulation of experimental data may be necessary for this aspect.

For theoretical calculations, we will illustrate from two points: the fundamental properties of graphene and the molecular dynamics analysis of catalytic reactions.

- Electronic Structure of Graphene: There are still some computational issues remaining in this thesis. For example, we have only preliminarily demonstrated the influence of linear wrinkle structures on the electronic states of graphene. Further systematic studies are needed. Additionally, similar to STM experiments, we need to explore other local defects, preferably in conjunction with experimental observations for analysis.

- Catalytic Activity of Graphene: If it were possible to simulate the chemical reactions during the etching process, it would undoubtedly make the connection between these three research projects even closer. Moreover, such calculations can provide a more intuitive and in-depth understanding of the catalytic activity of graphene materials. This part of the work requires a certain level of understanding and proficiency in theoretical calculations.

ACKNOWLEDGEMENTS

As my PhD journey is coming to an end, I have not yet had the time to thoroughly reflect on this research experience. However, it has already become an invaluable treasure in my life, far exceeding the expectations I had before coming to Japan for my studies. On the road ahead, I believe that I will continue to draw strength from all the people and experiences I have encountered during this time.

I sincerely thank all those who have contributed to the completion of this work. First and foremost, I would like to express my gratitude to my supervisor, Professor Kenta Arima. Words alone cannot fully convey my appreciation for his guidance and support. Since my master's studies, he has been guiding and assisting me in every aspect, from planning the research and preparing presentation to writing papers and attending to every detail. Over the years, he has always approached his work with dedication and treated everyone with equality, whether they are his students or others. There are many things I have learned from him that go beyond research. Additionally, I would like to thank Assistant Professor Kouji Inagaki. Without his extensive help with the calculations, I would not have been able to complete my current work. I am equally grateful to Professor Kazuya Yamamura and Assistant Professor Rongyan Sun for discussing my research during laboratory meetings, and for their advice and help outside of research. I would like to thank all the professors in the Department of Precision Engineering at Osaka University, including Professor Yoshitada Morikawa, Professor Kazuto Yamauchi, Professor Hirotsugu Ogi, Professor Yuji Kuwahara, Professor Heiji Watanabe, Professor Yasuhisa Sano, Associate Professor Hiroaki Kakiuchi, and so on, for their valuable comments and advice on my research.

Furthermore, I would like to thank Mr. Shaoxian Li and Mr. Seiya Yamamoto for their discussion, support, and assistance in my research and my daily life. I sincerely appreciate the support of the other members of Arima Lab and Yamamura Lab. I would like to extend my sincerest thanks to Ms. Mai Shindo, the secretary of Arima Lab, and Ms. Yukari Ogawa, the secretary of Yamamura Lab, for their patience and kind support in my daily life.

This work was supported by a Grant-in-Aid for JSPS Fellows (KAKENHI Grant No. JP23KJ1440 and No. JP21K18676). This work was also supported in part by Osaka University Fellowship Quantum Leader Resources (QLEAR), and a research grant from Mitutoyo Association for Science and Technology (Grant No. R2001).The computation in this work has been done using the facilities of the Supercomputer Center, the Institute for Solid State Physics (ISSP), the University of Tokyo.

Lastly, I want to express my heartfelt gratitude to my family for their endless support and

encouragement over the years. Especially during the COVID-19 pandemic, when many things became challenging, it was your unwavering support that allowed me to fully dedicate myself to my research. Thank you for always being there for me.